HEATED ATOMIC FORCE MICROSCOPE CANTILEVERS FOR POLYMER BASED ADDITIVE NANOMANUFACTURING

A Dissertation

by

MOHAMMADREZA SOLEYMANIHA

Submitted to the Office of Graduate and Professional Studies of
Texas A&M University
in partial fulfillment of the requirements for the degree of

DOCTOR OF PHILOSOPHY

Chair of Committee,	Jonathan Robert Felts
Committee Members,	Cynthia Hipwell
	Matt Pharr
	Xiaofeng Qian
Head of Department,	Andreas A. Polycarpou

August 2019

Major Subject: Mechanical Engineering

ABSTRACT

This dissertation demonstrates the design, simulation, fabrication and characterization processes of a novel heated atomic force microscope cantilever for polymer based additive nanomanufacturing. Fabrication and integration of heterogeneous nanostructures is an essential task for manufacturing next generation organic electronic devices. Current state-of-the-art in heated tip additive manufacturing has a limited write time and cannot accurately control polymer deposition rate. The new design presented here includes two embedded joule heaters connected by a microchannel, where thermo-capillary forces induced by the temperature gradient between heaters can deliver about 40 ng of polymer to the tip. The heated tip design presented here was informed by multi-physics finite element analysis to optimize the thermo-mechanical and thermo-fluidic performance of the device. Computational fluid dynamics simulations of molten polymer flowing in the microchannel shows the velocity of the leading edge depends significantly on the imposed temperature gradient. Thus, the cantilever tip can be inked, cleaned, and re-inked by controlling the temperature of the integrated heaters.

Following design optimization, this work details the step-by-step micro-fabrication processes for manufacturing the heated cantilevers. Electrical and thermal characterizations are performed to evaluate the temperature response and electrical resistance of the fabricated cantilevers, and is compared to the developed models. Preliminary results show a maximum temperature of 500 °C before thermal runaway occurs in the fabricated cantilevers, with temperature gradients as large as 2.0E6 °C/m.

Investigation of solid-liquid interactions at the nanoscale is crucially important to understand the mechanism of polymer spreading along the cantilever microchannel and tip. A new AFM-based measurement technique for dynamic measurement of polymer nanodroplet spreading at elevated temperatures is developed. The experimental setup is used to measure the spreading dynamics of polystyrene droplets with 2 μm diameters at 115-175 °C on flat surfaces. Custom image processing algorithms determine the droplet height, radius, volume, and contact angle of each AFM image over time to calculate the droplet spreading dynamics.

The new cantilever design and the AFM-based spreading measurement technique presented here, provide a framework to make better tools for wafer scale heterogeneous polymer nanostructure fabrication with high throughput, multiple feature registration, and high spatial resolution.

DEDICATION

To

My wonderful friend & wife, Somaye

My beloved gift of god, Ryan

My lovely mom, Mojgan

My dear father, Mahmood

My beautiful sisters;

Mahtab & Shabnam

ACKNOWLEDGEMENTS

First, I would like to thank my advisor, Dr. Jonathan Robert Felts, for accepting me as his first graduate student in his laboratory. He taught me a lot of things, not only scientific subjects, but also ethical and professional matters. Dr. Felts showed me the exciting side of research endeavors and made me a science fan. He took my hand in all of my research steps and showed me the way to success. I also would like to thank my doctoral committee members, Dr. Cynthia Hipwell, Dr. Matt Pharr and Dr. Qiaofeng Qian for their valuable participation in my Ph.D. projects. It was not possible to get to this point without their kind investment in my work.

Also, I would like to thank Dr. Sarbajit Banerjee and Dr. James Batteas for their invaluable help throughout my Ph.D. and their kind advice. Thanks to my coworkers, Shivaranjan Raghuraman, Achutha Tamraparni and Cody Chalker for their valuable, interesting and helpful helps and insights. I would like to thank all the staff members at the nanofabrication facility of Texas A&M University, Aggiefab for their support throughout my PhD career. I would also like to thank the Texas A&M High Performance Research Computing (HPRC) Facility for granting me an access to its supercomputing resources for performing computer simulations.

I would like to thank my lovely wife, Somaye and my shining diamond, Ryan. Without her friendship, love, passion, support, I had no chance of finishing such a long marathon. She has been sacrificing her life and time to support my research career. I will never forget the days she was spending with me at the nanofabrication facility of Texas

A&M University and giving me hope when I was hapless. I was blessed with the birth of my son on September 2018. With his cute smiles he simply motivated me to be best father for him.

Finally, I would like to thank my family in Iran. It has been 5 years that I have not been able to see them. Especially my mom who has prayed for my success since July 1986.

CONTRIBUTORS AND FUNDING SOURCES

This work was supervised by a dissertation committee consisting of Professor Jonathan Robert Felts [advisor], Professor Matt Pharr and Professor Cynthia Hipwell of the Department of Mechanical Engineering and Professor Xiaofeng Qian of the Department of Materials Science.

The electrical and thermal characterization measurements in Chapter 4 were conducted in part by Shivaranjan Raghuraman of Department of Mechanical Engineering and Cody Chalker of Department of Chemistry. All other work conducted for the dissertation was completed by the student independently

Graduate study was supported by Texas A&M Engineering Experiment Station fund.

TABLE OF CONTENTS

Page

LIST OF FIGURES

Page

LIST OF TABLES

Page

1. INTRODUCTION

Lithography is an important part of the fabrication process for micro-electro-mechanical systems (MEMS), Flash memory, and other semiconductor devices [1, 2]. Photolithography is a well-established method for patterning micro- and nanostructures on different types of surfaces. By exposing a surface coated by a thin layer of photoresist (polymer) with a specific wavelength of light through a photomask, different micro- and nanoscale features can be patterned on a variety of surfaces such as silicon, glass or other compound semiconductor wafers [3]. Although optical photolithography is a well-established patterning method in semiconductor manufacturing, patterning features smaller than the wavelength of light is extremely difficult, and sophisticated modifications are required to improve the patterning resolution.

One way to improve the resolution in photolithography is using light sources with shorter wavelength such as argon fluoride (ArF) or krypton fluoride (KrF) lasers at 193 nm and 248 nm [4] respectively and recently Extreme Ultraviolet (EUV) with the wavelength of 13.5 nm [5]. In a different approach in immersion lithography [6, 7], by replacing the air gap between the wafer and optical lenses with a liquid medium such as deionized water to increase the refractive index. Combining immersion lithography with double or triple patterning techniques, it has been feasible to pattern with sub-20 nm resolution. Although all these techniques have been able to continuously push device sizes ever smaller (aka Moore's Law), they are extremely expensive for all but the largest industrial applications. Another issue is compatibility of the techniques with organic

devices or 2D materials which limits application of these techniques in patterning emerging materials.

In addition to photolithography, polymers with tuned electrical, mechanical or optical properties can be used as the active organic materials in electronic devices such as organic thin film transistors (OTFTs), organic light-emitting diodes (OLEDs), flexible displays and solar cells to improve device flexibility, weight, and potential for massive scale up [8-10]. Despite the recent growing interest in organic material devices, it is challenging to pattern and integrate organic materials into electronic devices with high spatial resolution and high throughput, primarily due to incompatibility of polymers with most of current micro/nanomanufacturing techniques [11, 12]. At a fundamental level, it is still unknown how to integrate active polymers into micro/nano devices when virtually all of the current fabrication strategies involve photolithography steps that would destroy these materials. This challenge is further amplified when fabricating devices with multiple organic components.

1.1. Beam-based Lithography

Beam-based lithography toolsets such as Electron Beam Lithography (EBL) [13] or Focused Ion Beam (FIB) can be utilized to pattern features with sub 10nm resolution [14, 15]. In EBL, a focused beam of electrons exposes the photoresist coated surface and chemically modifies the resist layer to pattern the surface without using photomask [16]. Although by using EBL patterning with below 100 nm is feasible, patterning at below 30 nm is difficult due to proximity effects [17]. FIB works based on exposing a focused high energy ion beam to either etch or deposit different materials on a substrate [18]. New ion-

based fabrication tools have demonstrated superior results such as He ions [19]. FIB has the privilege of using heavy ions which gives the beam more momentum to perform patterning with even higher resolution as compared to EBL. However, the operational cost, maintenance, throughput and compatibility with new nanomaterials such 2D materials, have inhibited these tools to take over the optical lithography position in semiconductor manufacturing industry [20, 21]. One of the biggest obstacles in beam based lithography for 2D material-based electronics is electron beam-induced damages during patterning process which can either damage or change the electrical properties of the 2D materials [22, 23].

1.2. Nanoimprint Lithography

Non-optical lithography techniques such as nanoimprint lithography (NIL) [24, 25] and Tip-based nanofabrication (TBN) [26] have demonstrated feature sizes below 10 nm. NIL is a cost-effective, high resolution, high throughput maskless method in which a mold with nanoscale patterns is pressed on a thermoplastic (thermal NIL) or photo (UV) curable resist (UV-NIL) coated surface and deforms the soft thin resist by mechanical force to transfer the inverse shape of the mold to the resist [27]. In thermal NIL, the resist is heated up above its glass transition temperature during pressing the mold whereas in the UV-NIL the resist is cured with UV light before removing the mold. One of the main advantages of the NIL over other conventional optical lithography techniques is simplicity of the method to pattern sub-10 nm features and material compatibility specifically for biomedical applications [28, 29]. However, resist adhesion to the mold and defects on the mold after each process are the main critical issues which require NIL more optimizations

[30]. Moreover, for printing more than one material, there will be limitation in terms of molecular weight of glass transition temperature otherwise will result in instability in imprinted structures [27].

1.3. Scanning Probe Lithography (SPL)

Another low cost, high resolution alternative to the conventional lithography methods is TBN, in which a sharp nanoscale tip fabricates nanostructures on a variety of surfaces [26, 31]. Scanning tunneling microscope (STM) [32] and Atomic Force Microscope (AFM) [33] are two important tools which are dominantly used as scanning probe lithography (SPL) tools [34].

STM, a versatile type of scanning probe microscope (SPM) tool, invented in 1986 which works based on quantum tunneling for surface imaging at the atomic scale [32]. It utilizes an extremely sharp metal tip with single atom at the end and is connected to a piezoelectric tube on its other end. The tip is brought to the vicinity of the surface and the by applying a bias voltage to the tip, electrons will travel from the tip to the conducting surface and vice versa. The applied voltage is controlled to keep the distance between the tip and the surface constant throughout the scanning process. Therefore, the voltage change will be used to re-produce the surface topography as the tip travels across the surface with lateral resolution of 0.1-0.2 nm [35] and is reported to have as high as 1 atom resolution for nanomanipulation applications [36]. Figure 1.1 shows a schematic view of STM. STM has shown potentials to be used as a lithography tool with high resolution [37, 38]. However, one of the main drawbacks of the STM technique is difficulty of making and preparing atomically sharp STM tips with defined physical and chemical properties

[39]. Moreover, STM requires extremely clean surface and only can be performed on conductive surfaces which limits its application to be considered as a tool for patterning features.

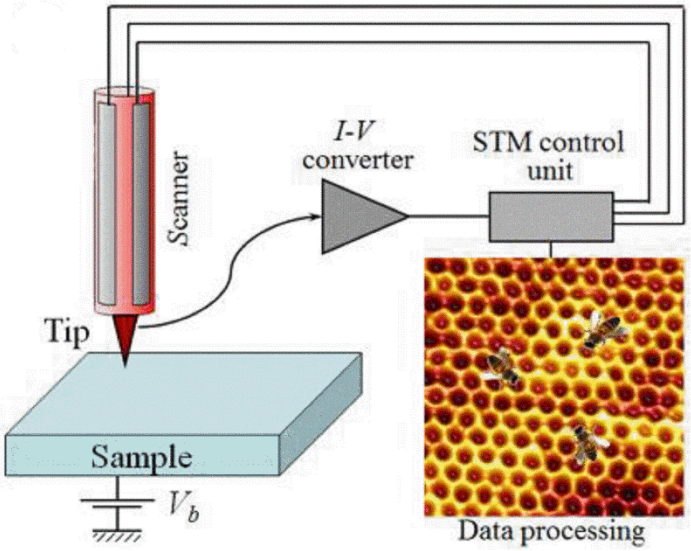

Figure 1.1 View of STM equipment (reprinted from Chaika [40]).

1.4. Atomic Force Microscopy (AFM)

AFM, invented in 1986 by Binning [33], utilizes a cantilever with a sharp nanoscale tip which has about 10 nm diameter. The cantilever is connected to a piezoactuator which oscillates the cantilever at its resonance frequency. Figure 1.2 shows the schematic view of a typical AFM instrument. Depends on the distance between the tip and the surface, either repulsive or attractive forces cause the cantilever to bend outward or inward, respectively. The bending in the cantilever is measured with a laser and a photodiode. The laser is irradiated by bending the cantilever and the change is detected and converted to electrical signal by a photodiode. The resulting signal is then used to re-

construct the surface morphology and roughness. There is a closed loop feedback control system which provides constant force on the cantilever by using the inputs from the photodiode. AFM probes are made out of silicon, silicon oxide and can be coated with diamond [41] or platinum [42] or polymer to modify the properties of the cantilever or the tip [43].

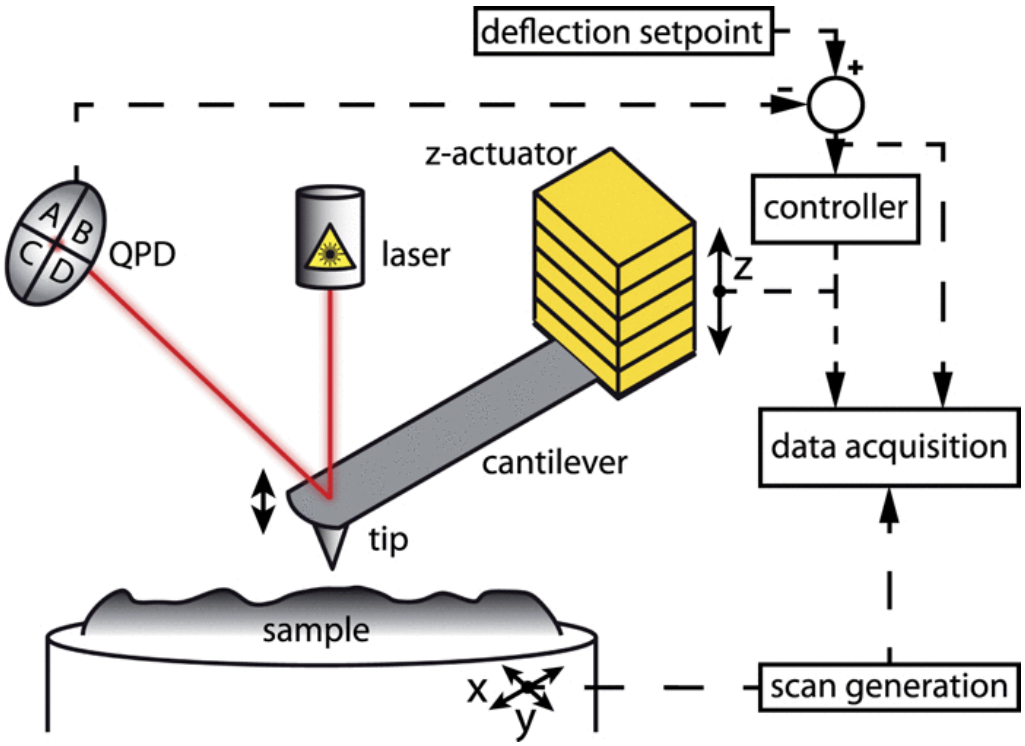

Figure 1.2 Schematic of the atomic force microscope tool (reprinted from Steininger *et al*. [44]).

One of the main advantages of the AFM-based fabrication techniques is in-situ imaging of the nanostructures after each fabrication process which eliminates the need to remove the sample for analyzing the chemical and topographical properties of the

fabricated features. AFM has been used to pattern a wide range of materials including semiconductors [45-48], biomaterials [49-51], metals, polymers [52, 53] and 2D materials [34, 54-56] either by adding or removing these materials to the substrate. The fabrication processes are categorized based on the dominant type of interaction between the AFM tip and the surface which can be mechanical, thermal, chemical, or diffusive. Figure 1.3 shows different classes of probe based techniques of lithography based on the dominant interaction type between tip and surface [34]. A diffusive AFM-based nanolithography technique to directly deposit materials from AFM nanoscale tip to a substrate is called dip-pen nanolithography (DPN) [57, 58]. In DPN, organic, biomolecules [59, 60] or liquid inks [61] are transferred from the nanoscale AFM tip to a variety of surfaces. Nevertheless, difficulty in controlling the ink transport and limited material types which can be deposited by DPN, has limited the application of this technique for wider applications in nanopatterning.

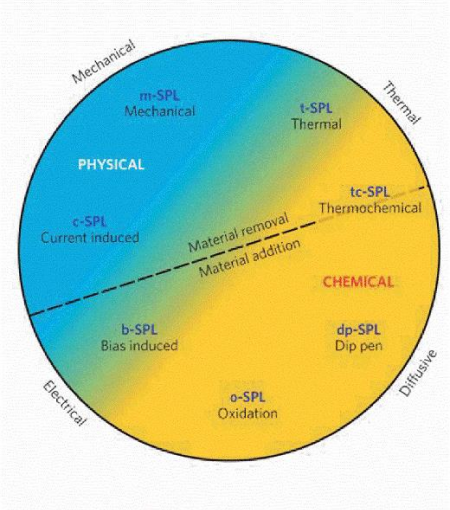

Figure 1.3 Different SPL techniques classified based on the dominant tip-surface interaction (reprinted from Garcia *et al*. [34]).

1.5. Thermal Scanning Probe Lithography (t-SPL)

Thermal SPL (t-SPL) was introduced for the first time in 1992 for data storage application in which infrared laser was used to heat up the AFM cantilever tip in contact with PMMA coated surface [62]. The resulting high temperature in the tip could locally indent the polymer film in the tip-surface contact area and created nanoscale pits on the surface. Later, laser heating was substituted by integrated heaters in which the AFM cantilevers are heated by electrical current flow through the cantilever legs and tip which are highly and lightly doped, respectively [63-65]. By contacting the heated AFM tip with the surface, a nanoscale hot spot with temperature of over 1000 C, depending on the dopants type, can be created at the contact point between the tip and the surface [66]. Figure 1.4(a) shows a schematic illustration of t-SPL. Heated AFM cantilevers have thermal time constant of 5 to more than 100 micro seconds which allows for rapid stimulus. [34, 66] In a specific variation of t-SPL, which is called thermochemical scanning probe lithography (tc-SPL), the resulting heat is used to chemically modify a material with resolution down to sub 10 nm. [53, 67, 68] The heat in this technique is used to trigger chemical reactions at the contact point between the heated tip and the surface to locally modulate chemical, electrical or optical properties of the substrate [69]. tc-SPL has demonstrated various applications in biology [70], applied physics [71, 72] and for fabrication of heterogeneous nanostructures [73, 74]. Figure 1.4(b) shows optical image of one common type of t-SPL cantilever.

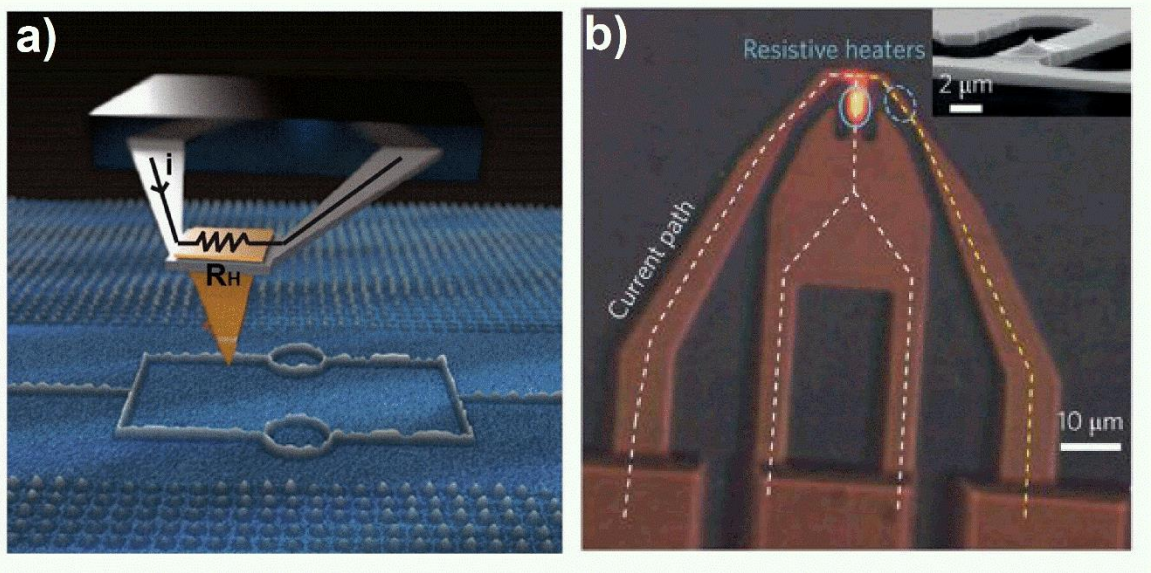

Figure 1.4 (a) Schematic view of t-SPL for patterning at the nanoscale (reprinted from Albisetti *et al.* [75]). (b) Optical image of a typical t-SPL cantilever with two joule heaters. Inset: SEM image of the tip of cantilever (reprinted from Garcia *et al.* [34]).

1.6. Thermal Dip-pen Nanolithography (t-DPN)

The resistive heating technique in heated AFM cantilevers can be used to locally transfer or deposit materials from the heated AFM tip to the surface [76]. In thermal dip-pen nanolithography (t-DPN), a heated AFM tip is coated with polymer or suspended nanoparticles in a polymer, placed in contact with a surface and heated above the glass transition temperature to pattern nanostructures. Figure 1.5(a-b) shows the schematic of t-DPN patterning technique in two different modes of writing nanostructures and reading the fabricated features, respectively.

Printing polymers, metals, semiconductor nanoparticles have been performed with t-DPN with resolutions close to single molecule [77]. The mass transfer between the tip and the substrate is a balance between thermocapillary stress due to temperature gradient

along the tip-substrate and viscous forces such that in a hotter tip, polymer can be transferred with a larger flow rate [78]. Figure 1.5(c) shows SEM image of a t-DPN cantilever which has been commonly used for a wide range of nanopatterning of polymers. In order to ink AFM tips in various SPM based patterning techniques and dispense the ink to a substrate, different techniques have been developed in the past. In Dip pen Nanolithography (DPN) which is similar to t-DPN but is performed at room temperature, the AFM tip is simply dipped into the ink reservoir and is coated [57]. In nanoscale dispensing (NADIS) a cantilever is specifically designed with a milled cavity, which acts as the reservoirs on top of a hollow tip outlet and the ink is placed directly on the cantilever reservoir. [79] Another technique for inking a probe is feeding the tip with a microfluidic channel which delivers the ink from a reservoir to a tip [80, 81]. t-DPN has a similar mechanism for feeding the tip in which, the tip is dipped into a molten polymer reservoir manually for each patterning process which is a time consuming procedure.

The current t-DPN cantilevers can deposit and pattern nanostructures as large as several μm^2 with sub 100 nm spatial resolution. However, lack of ability to control the polymer flow rate and insufficient polymer supply on the cantilever, make it practically impossible to pattern areas larger than several μm^2.

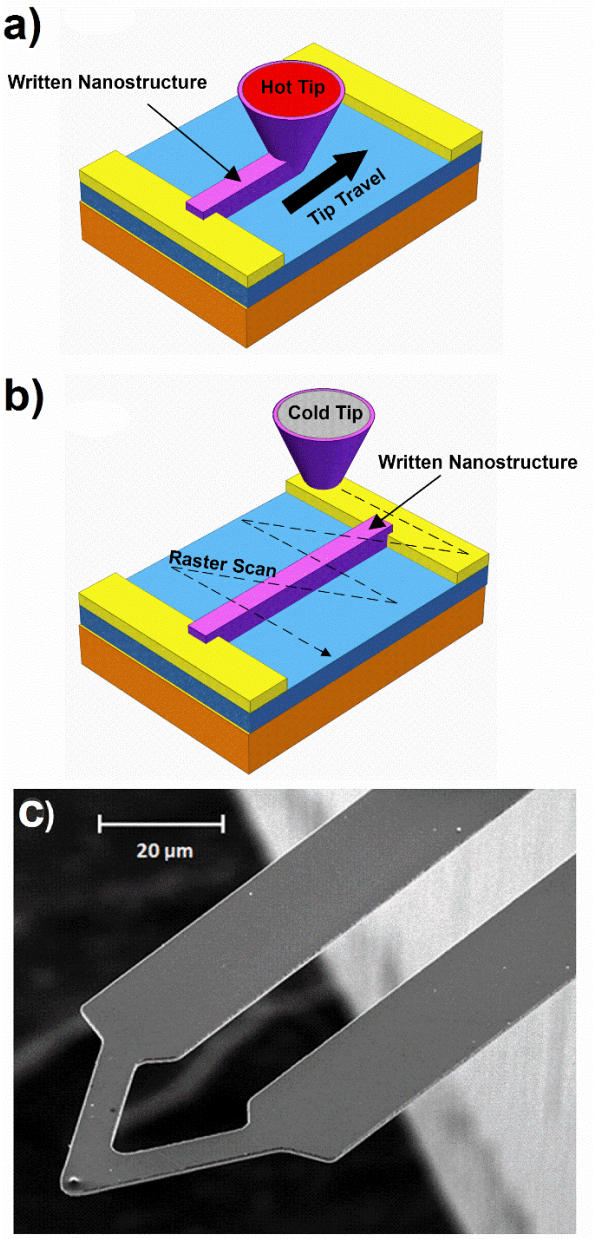

Figure 1.5 (a-b) Schematic illustration of t-DPN patterning technique in writing mode and imaging mode, respectively. (c) SEM image of a t-DPN cantilever (reprinted from Felts [82]).

1.7. Dissertation Overview

This dissertation presents the full process of design, simulation, fabrication and characterization of a new generation of heated AFM cantilever with double heaters for nanolithography applications such as patterning for organic or 2D-based nanoelectronic devices. In order to overcome the contributed issues with the older t-DPN cantilever designs, a new design which potentially has higher throughput and features controllability over polymer flow is presented in this report. The new cantilever design has a reservoir heater that can deposit about 40 ng of solid polymer and is connected to the tip via a microchannel. The temperature of the heaters can be controlled individually which provides controllability on temperature gradient along the microchannel.

Since the molten polymer is spreading and wets the microchannel, it is crucial to understand the spreading behavior of polymer at high temperature at the nanoscale. Almost all of the experimental techniques to study the spreading are only suitable for meso or larger scales. Different techniques such as optical goniometry and ellipsometry are widely used to study macroscale droplets spreading [83-85]. However, because of limited resolution of the optical measurement tools due to the light diffraction effect, it is not possible to study nanoscale droplets spreading. In the case of the ellipsometer, despite having high vertical resolution, the spot size is on the order of 10 μm, making it impractical for studying nanoscale heterogeneity in the fluid or the substrate. Measuring the complex spreading behavior of heterogeneous systems requires spatial resolutions below 100 nm in three dimensions with detection sensitivity capable of identifying the variable compositions of both the fluid and the substrate. Here we developed a technique for

measuring thermoplastic polymer spreading dynamics with nanometer scale spatial resolution at elevated temperatures using AFM. The AFM-based measurement technique provides a way to measure spreading dynamics of small volumes of heterogeneously complex fluids not possible through other means.

The gained knowledge of polymer wetting behavior can be applied directly to the new t-DPN where molten polymer spreads along the channel and the ability to understand and control the polymer flow at high temperature and temperature gradient will lead to a better heated cantilever design and more precise nanopatterning results. The design presented here provides a platform for wafer scale polymer nanostructure fabrication with mass flow control required for nano-manufacturing complex polymer-based devices.

Chapter 2 presents the design process used to study and control the mechanical, thermal and fluid dynamics behavior of the proposed heated AFM cantilevers. Chapter 3 demonstrates experimental studies of wetting of polymer droplets at the nanoscale using a novel AFM-based technique. The results of this study can be insightful to understand the wetting behavior of the molten polymers on the new heated AFM cantilevers. Chapter 4 presents the nanofabrication process and characterization of the heated AFM cantilevers. The new design of heated AFM cantilever provides a new platform in SPL and provides a new tool in t-DPN for fabricating heterostructures at the nanoscale with high throughput.

1.8. References

1. Campbell, S.A., *Fabrication Engineering at the Micro-and Nanoscale (the Oxford Series in Electrical and Computer Engineering).* 2012.
2. Madou, M.J., *Fundamentals of Microfabrication: The Science of Miniaturization*. 2002: CRC press.
3. Mack, C., *Fundamental Principles of Optical Lithography: The Science of Microfabrication*. 2008: John Wiley & Sons.
4. Ito, T. and S. Okazaki, *Pushing the Limits of Lithography*. Nature, 2000. **406**(6799): p. 1027.
5. Gwyn, C.W., et al., *Extreme Ultraviolet Lithography.* Journal of Vacuum Science & Technology B: Microelectronics and Nanometer Structures Processing, Measurement, and Phenomena, 1998. **16**(6): p. 3142-3149.
6. Mulkens, J., et al., *Benefits and Limitations of Immersion Lithography.* Journal of Micro/Nanolithography, MEMS, and MOEMS, 2004. **3**(1): p. 104-115.
7. Switkes, M. and M. Rothschild, *Immersion Lithography at 157 Nm.* Journal of Vacuum Science & Technology B: Microelectronics and Nanometer Structures Processing, Measurement, and Phenomena, 2001. **19**(6): p. 2353-2356.
8. Koch, N., *Organic Electronic Devices and Their Functional Interfaces.* ChemPhysChem, 2007. **8**(10): p. 1438-1455.
9. Berggren, M., D. Nilsson, and N.D. Robinson, *Organic Materials for Printed Electronics.* Nature materials, 2007. **6**(1): p. 3.

10. Günes, S., H. Neugebauer, and N.S. Sariciftci, *Conjugated Polymer-Based Organic Solar Cells.* Chemical Reviews, 2007. **107**(4): p. 1324-1338.

11. Sheats, J.R., *Manufacturing and Commercialization Issues in Organic Electronics.* Journal of Materials Research, 2004. **19**(7): p. 1974-1989.

12. Kelley, T.W., et al., *Recent Progress in Organic Electronics: Materials, Devices, and Processes.* Chemistry of Materials, 2004. **16**(23): p. 4413-4422.

13. Vieu, C., et al., *Electron Beam Lithography: Resolution Limits and Applications.* Applied Surface Science, 2000. **164**(1-4): p. 111-117.

14. Seliger, R., et al., *High-Resolution, Ion-Beam Processes for Microstructure Fabrication.* Journal of Vacuum Science and Technology, 1979. **16**(6): p. 1610-1612.

15. Tseng, A.A., *Recent Developments in Nanofabrication Using Focused Ion Beams.* Small, 2005. **1**(10): p. 924-939.

16. McCord, M.A. and M.J. Rooks, *Electron Beam Lithography.* Handbook of microlithography, micromachining, and microfabrication, 1997. **1**: p. 139-249.

17. Chang, T., *Proximity Effect in Electron-Beam Lithography.* Journal of Vacuum Science and Technology, 1975. **12**(6): p. 1271-1275.

18. Komuro, M., et al., *Maskless Etching of a Nanometer Structure by Focused Ion Beams.* Journal of Vacuum Science & Technology B: Microelectronics Processing and Phenomena, 1983. **1**(4): p. 985-989.

19. Hlawacek, G., et al., *Helium Ion Microscopy.* Journal of Vacuum Science & Technology B, Nanotechnology and Microelectronics: Materials, Processing, Measurement, and Phenomena, 2014. **32**(2): p. 020801.

20. Chen, S., et al., *Monolayer Mos2 Nanoribbon Transistors Fabricated by Scanning Probe Lithography.* Nano Letters, 2019.

21. Zheng, X., et al., *Patterning Metal Contacts on Monolayer Mos 2 with Vanishing Schottky Barriers Using Thermal Nanolithography*. Nature Electronics, 2019. **2**(1): p. 17.

22. Lehnert, T., et al., *Electron Radiation Damage Mechanisms in 2d Mose2.* Applied Physics Letters, 2017. **110**(3): p. 033106.

23. Meyer, J.C., et al., *Accurate Measurement of Electron Beam Induced Displacement Cross Sections for Single-Layer Graphene.* Physical Review Letters, 2012. **108**(19): p. 196102.

24. Chou, S.Y., P.R. Krauss, and P.J. Renstrom, *Nanoimprint Lithography*. Journal of Vacuum Science & Technology B: Microelectronics and Nanometer Structures Processing, Measurement, and Phenomena, 1996. **14**(6): p. 4129-4133.

25. Austin, M.D., et al., *Fabrication of 5 Nm Linewidth and 14 Nm Pitch Features by Nanoimprint Lithography.* Applied Physics Letters, 2004. **84**(26): p. 5299-5301.

26. Tseng, A.A., *Tip-Based Nanofabrication: Fundamentals and Applications*. 2011: Springer.

27. Guo, L.J., *Nanoimprint Lithography: Methods and Material Requirements.* Advanced Materials, 2007. **19**(4): p. 495-513.

28. Glangchai, L.C., et al., *Nanoimprint Lithography Based Fabrication of Shape-Specific, Enzymatically-Triggered Smart Nanoparticles.* Journal of Controlled Release, 2008. **125**(3): p. 263-272.

29. Traub, M.C., W. Longsine, and V.N. Truskett, *Advances in Nanoimprint Lithography.* Annual review of chemical and biomolecular engineering, 2016. **7**: p. 583-604.

30. Kim, K.-S., et al., *Tribology Issues in Nanoimprint Lithography.* Journal of mechanical science and technology, 2010. **24**(1): p. 5-12.

31. Hu, H., H. Kim, and S. Somnath, *Tip-Based Nanofabrication for Scalable Manufacturing.* Micromachines, 2017. **8**(3): p. 90.

32. Binnig, G., et al., *Surface Studies by Scanning Tunneling Microscopy.* Physical Review Letters, 1982. **49**(1): p. 57.

33. Binnig, G., C.F. Quate, and C. Gerber, *Atomic Force Microscope.* Physical Review Letters, 1986. **56**(9): p. 930.

34. Garcia, R., A.W. Knoll, and E. Riedo, *Advanced Scanning Probe Lithography.* Nature Nanotechnology, 2014. **9**(8): p. 577.

35. Bai, C., *Scanning Tunneling Microscopy and Its Application*. Vol. 32. 2000: Springer Science & Business Media.

36. Eigler, D.M. and E.K. Schweizer, *Positioning Single Atoms with a Scanning Tunnelling Microscope.* Nature, 1990. **344**(6266): p. 524.

37. Mamin, H., et al., *Gold Deposition from a Scanning Tunneling Microscope Tip.* Journal of Vacuum Science & Technology B: Microelectronics and Nanometer Structures Processing, Measurement, and Phenomena, 1991. **9**(2): p. 1398-1402.

38. Ringger, M., et al., *Nanometer Lithography with the Scanning Tunneling Microscope.* Applied Physics Letters, 1985. **46**(9): p. 832-834.

39. Hamers, R., *9.2. 1.5 Limitations and Continued Development of Stm*, in *Interaction of Radiation with Surfaces and Electron Tunneling*. 1996, Springer. p. 371-372.

40. Chaika, A.N., *High Resolution Stm Imaging*, in *Surface Science Tools for Nanomaterials Characterization*. 2015, Springer. p. 561-619.

41. Holt, K.B., et al., *Scanning Electrochemical Microscopy and Conductive Probe Atomic Force Microscopy Studies of Hydrogen-Terminated Boron-Doped Diamond Electrodes with Different Doping Levels.* The Journal of Physical Chemistry B, 2004. **108**(39): p. 15117-15127.

42. Bhushan, B. and K.J. Kwak, *Platinum-Coated Probes Sliding at up to 100 Mm S−1 against Coated Silicon Wafers for Afm Probe-Based Recording Technology*. Nanotechnology, 2007. **18**(34): p. 345504.

43. Hong, S.S., J.J. Cha, and Y. Cui, *One Nanometer Resolution Electrical Probe Via Atomic Metal Filament Formation.* Nano Letters, 2010. **11**(1): p. 231-235.

44. Steininger, J., et al., *High Bandwidth Deflection Readout for Atomic Force Microscopes.* Review of Scientific Instruments, 2015. **86**(10): p. 103701.

45. Held, R., et al., *In-Plane Gates and Nanostructures Fabricated by Direct Oxidation of Semiconductor Heterostructures with an Atomic Force Microscope.* Applied Physics Letters, 1998. **73**(2): p. 262-264.

46. Minne, S., et al., *Fabrication of 0.1 Mm Metal Oxide Semiconductor Field-Effect Transistors with the Atomic Force Microscope.* Applied Physics Letters, 1995. **66**(6): p. 703-705.

47. Campbell, P., E. Snow, and P. McMarr, *Fabrication of Nanometer-Scale Side-Gated Silicon Field Effect Transistors with an Atomic Force Microscope.* Applied Physics Letters, 1995. **66**(11): p. 1388-1390.

48. Ryu, Y.K. and R. Garcia, *Advanced Oxidation Scanning Probe Lithography.* Nanotechnology, 2017. **28**(14): p. 142003.

49. Fotiadis, D., et al., *Imaging and Manipulation of Biological Structures with the Afm.* Micron, 2002. **33**(4): p. 385-397.

50. Muller, D.J., *Afm: A Nanotool in Membrane Biology.* Biochemistry, 2008. **47**(31): p. 7986-7998.

51. Dufrêne, Y.F., et al., *Imaging Modes of Atomic Force Microscopy for Application in Molecular and Cell Biology.* Nature Nanotechnology, 2017. **12**(4): p. 295.

52. Felts, J.R., et al., *Nanometer-Scale Flow of Molten Polyethylene from a Heated Atomic Force Microscope Tip.* Nanotechnology, 2012. **23**(21): p. 215301.

53. Pires, D., et al., *Nanoscale Three-Dimensional Patterning of Molecular Resists by Scanning Probes.* Science, 2010. **328**(5979): p. 732-735.

54. Dago, A.I., Y.K. Ryu, and R. Garcia, *Sub-20 Nm Patterning of Thin Layer Wse2 by Scanning Probe Lithography.* Applied Physics Letters, 2016. **109**(16): p. 163103.

55. Liu, X., et al., *Scanning Probe Nanopatterning and Layer-by-Layer Thinning of Black Phosphorus.* Advanced Materials, 2017. **29**(1): p. 1604121.

56. Stanford, M.G., P.D. Rack, and D. Jariwala, *Emerging Nanofabrication and Quantum Confinement Techniques for 2d Materials Beyond Graphene.* npj 2D Materials and Applications, 2018. **2**(1): p. 20.

57. Ginger, D.S., H. Zhang, and C.A. Mirkin, *The Evolution of Dip-Pen Nanolithography.* Angewandte Chemie International Edition, 2004. **43**(1): p. 30-45.

58. Piner, R.D., et al., *" Dip-Pen" Nanolithography.* Science, 1999. **283**(5402): p. 661-663.

59. Demers, L., et al., *Direct Patterning of Modified Oligonucleotides on Metals and Insulators by Dip-Pen Nanolithography.* Science, 2002. **296**(5574): p. 1836-1838.

60. Sistiabudi, R. and A. Ivanisevic, *Dip-Pen Nanolithography of Bioactive Peptides on Collagen-Terminated Retinal Membrane.* Advanced Materials, 2008. **20**(19): p. 3678-3681.

61. Nakashima, H., et al., *Liquid Deposition Patterning of Conducting Polymer Ink onto Hard and Soft Flexible Substrates Via Dip-Pen Nanolithography.* Langmuir, 2011. **28**(1): p. 804-811.

62. Mamin, H. and D. Rugar, *Thermomechanical Writing with an Atomic Force Microscope Tip.* Applied Physics Letters, 1992. **61**(8): p. 1003-1005.

63. Lee, J., et al., *Electrical, Thermal, and Mechanical Characterization of Silicon Microcantilever Heaters.* Journal of Microelectromechanical Systems, 2006. **15**(6): p. 1644-1655.

64. Chui, B., et al., *Low-Stiffness Silicon Cantilevers for Thermal Writing and Piezoresistive Readback with the Atomic Force Microscope.* Applied Physics Letters, 1996. **69**(18): p. 2767-2769.

65. Mamin, H.J., et al., *High-Density Data Storage Based on the Atomic Force Microscope.* Proceedings of the IEEE, 1999. **87**(6): p. 1014-1027.

66. King, W.P., et al., *Heated Atomic Force Microscope Cantilevers and Their Applications.* Annual Review of Heat Transfer, 2013. **16**.

67. Szoszkiewicz, R., et al., *High-Speed, Sub-15 Nm Feature Size Thermochemical Nanolithography.* Nano Letters, 2007. **7**(4): p. 1064-1069.

68. Ryu Cho, Y.K., et al., *Sub-10 Nanometer Feature Size in Silicon Using Thermal Scanning Probe Lithography.* ACS Nano, 2017. **11**(12): p. 11890-11897.

69. Carroll, K.M., et al., *Fabricating Nanoscale Chemical Gradients with Thermochemical Nanolithography.* Langmuir, 2013. **29**(27): p. 8675-8682.

70. Martínez, R.V., et al., *Large-Scale Nanopatterning of Single Proteins Used as Carriers of Magnetic Nanoparticles.* Advanced Materials, 2010. **22**(5): p. 588-591.

71. Shaw, J.E., P.N. Stavrinou, and T.D. Anthopoulos, *On-Demand Patterning of Nanostructured Pentacene Transistors by Scanning Thermal Lithography.* Advanced Materials, 2013. **25**(4): p. 552-558.

72. Wang, D., et al., *Local Wettability Modification by Thermochemical Nanolithography with Write-Read-Overwrite Capability.* Applied Physics Letters, 2007. **91**(24): p. 243104.

73. Wei, Z., et al., *Nanoscale Tunable Reduction of Graphene Oxide for Graphene Electronics.* Science, 2010. **328**(5984): p. 1373-1376.

74. Kim, S., et al., *Direct Fabrication of Arbitrary-Shaped Ferroelectric Nanostructures on Plastic, Glass, and Silicon Substrates.* Advanced Materials, 2011. **23**(33): p. 3786-3790.

75. Albisetti, E., et al. *Thermal Scanning Probe Lithography: From Spintronics to Biomedical Applications*. in *Emerging Patterning Technologies 2018*. 2018. International Society for Optics and Photonics.

76. Sheehan, P., et al., *Nanoscale Deposition of Solid Inks Via Thermal Dip Pen Nanolithography.* Applied Physics Letters, 2004. **85**(9): p. 1589-1591.

77. Nelson, B.A., et al., *Direct Deposition of Continuous Metal Nanostructures by Thermal Dip-Pen Nanolithography.* Applied Physics Letters, 2006. **88**(3): p. 033104.

78. Chung, S., et al., *Temperature-Dependence of Ink Transport During Thermal Dip-Pen Nanolithography.* Applied Physics Letters, 2011. **99**(19): p. 193101.

79. Meister, A., et al., *Nanoscale Dispensing of Liquids through Cantilevered Probes.* Microelectronic Engineering, 2003. **67**: p. 644-650.

80. Kim, K.-H., et al., *A Novel Afm Chip for Fountain Pen Nanolithography-Design and Microfabrication.* MRS Online Proceedings Library Archive, 2003. **782**.

81. Leichle, T., et al., *A Microcantilever-Based Picoliter Droplet Dispenser with Integrated Force Sensors and Electroassisted Deposition Means.* Journal of Microelectromechanical Systems, 2008. **17**(5): p. 1239-1253.

82. Felts, J., *Tip-Based Nanomanufacturing and Metrology of Heterogeneous Nanostructures*. 2014, University of Illinois at Urbana-Champaign.

83. Yuan, Y. and T.R. Lee, *Contact Angle and Wetting Properties*, in *Surface Science Techniques*. 2013, Springer. p. 3-34.

84. Bonn, D., et al., *Wetting and Spreading.* Reviews of Modern Physics, 2009. **81**(2): p. 739.

85. Kalantarian, A., R. David, and A. Neumann, *Methodology for High Accuracy Contact Angle Measurement.* Langmuir, 2009. **25**(24): p. 14146-14154.

2. HEATED AFM CANTILEVERS: DESIGN AND SIMULATION[1]

2.1. Introduction

Polymers are ubiquitous in microfabrication processes, often serving as a sacrificial layer for photolithographic pattern transfer to inorganic crystalline films such as silicon [1-3]. More recently, polymers have been developed with electrical [4] and optical [5] properties which can serve as the active material in organic analogues to current inorganic devices, with the benefit of reduced weight, enhanced flexibility, and potential for massive scale up [6, 7]. Research into polymer-based photovoltaics, logic circuits, microfluidics and light emitting diodes has led to the development of a number of devices, such as solar energy harvesters and electronic displays [8-18]. Despite the progress in polymer material and device development, advances in manufacturing processes to pattern polymers with nanometer scale spatial resolution have been limited, primarily because polymers are largely incompatible with most current micro/nanomanufacturing techniques. Alternative manufacturing schemes are thus required to reliably pattern polymer nanostructures with high spatial resolution and high throughput.

Different methods for fabricating polymer nanostructures have been developed over the last few decades, with varying levels of spatial resolution, material compatibility, feature registration, and throughput. Nanoimprint Lithography is a hot embossing

[1] Reprinted from Soleymaniha, M. and J.R. Felts, Design of a heated micro-cantilever optimized for thermo-capillary driven printing of molten polymer nanostructures. International Journal of Heat and Mass Transfer, 2016. 101: p. 166-174. With permission from Elsevier

technique to pattern polymer thin films with better than 10 nm resolution and extremely high throughput, but the technique is largely limited to a single polymeric material [19, 20]. Block copolymer self-assembly creates heterogeneous polymer nanostructures with high density and near 10 nm resolution, but controlling domain alignment and location requires additional nanopatterning techniques [21, 22]. Layer-by-layer (LBL) assembly and molecular layer deposition (MLD) have previously demonstrated sub-nm control of polymer film deposition, but offers little lateral control over placement of structures within the deposited film [23, 24]. Electrohydrodynamic (EHD) jetting has demonstrated printing polymer structures with high density and material control, with resolutions approaching sub-50 nm [25, 26]. Capillary rise of molten polymers within nanoporous anodic aluminum oxide (AAO) templates generates polymer nanorods and nanotubes with sub 30 nm, but does not provide a method to controllably position them [27, 28]. Although many advancements have been made to pattern polymers, current techniques do not offer a clear method for patterning polymer with sub 100 nm feature size and spatial resolution, broad material compatibility, and lithographic registration to previously patterned features.

Thermal Dip-pen Nanolithography (tDPN) is an atomic force microscope (AFM) based technique capable of creating nano-architectures from molten polymer [29]. In tDPN, a nanometer sharp heated AFM tip is coated with polymer, placed in contact with a surface, and heated above the polymer glass transition temperature to print polymer onto the surface [30]. Previous work has demonstrated printing metals, polymers, and polymer-nanoparticle composites with resolutions approaching single molecules [31-33]. The polymer mass flow rate depends on the balance between thermo-capillary stress—induced

by the temperature gradient between the heater and the cool substrate—and viscous resistance to flow, such that hotter temperatures result in larger mass flow rates [34]. The current micro-cantilevers used in tDPN can pattern hundreds of polymer structures with sub-100 nm spatial resolution, but cannot store large concentrations of polymer, and cannot precisely control mass flow from the tip, making it difficult to pattern areas larger than several μm^2.

Here we present the design of a heated microcantilever device capable of writing millions of polymer nanostructures with ~40 fg/s mass flow rate control [29] , which will enable polymer nanostructure patterning over areas many orders of magnitude larger than currently possible. Figure 2.1(a) shows the schematic of the micro-cantilever design, which contains two embedded Joule heaters (tip and reservoir heaters) connected *via* a microchannel. The Joule heaters are formed through selective doping, where the highly doped legs efficiently pass electric current and the low doped heater regions generate heat. The reservoir heater stores ~40 ng of solid polymer, and allows polymer to imbibe the microchannel *via* capillary action upon heating above the glass transition temperature. Additionally, the temperature gradient between the reservoir and tip heaters creates a thermocapillary stress (τ_{TC}) on the polymer free surface, causing the fluid to flow from hot to cold (figure 2.1(b)). The imbibing polymer fills a separate reservoir surrounding the tip (figure 2.1(c)), and heating the tip when in contact with a substrate then transports the molten polymer from the tip to the surface. Figure 2.1(d-f) illustrates the effect of the imposed temperature gradient on the polymer mass flow. When both heaters maintain the same temperature, no gradient exists and polymer flows predominantly by capillary action

(Figure 2.1(d)). Raising the reservoir temperature above the tip temperature creates a thermocapillary stress that enhances capillary flow towards the tip (Figure 2.1(e)), whereas raising the tip temperature above the reservoir temperature slows or reverses the advancement of the polymer front (Fig 2.1(f)). A gradient also exists between the hot tip heater and an unheated substrate upon tip contact, driving polymer flow from the tip reservoir to the substrate [29].

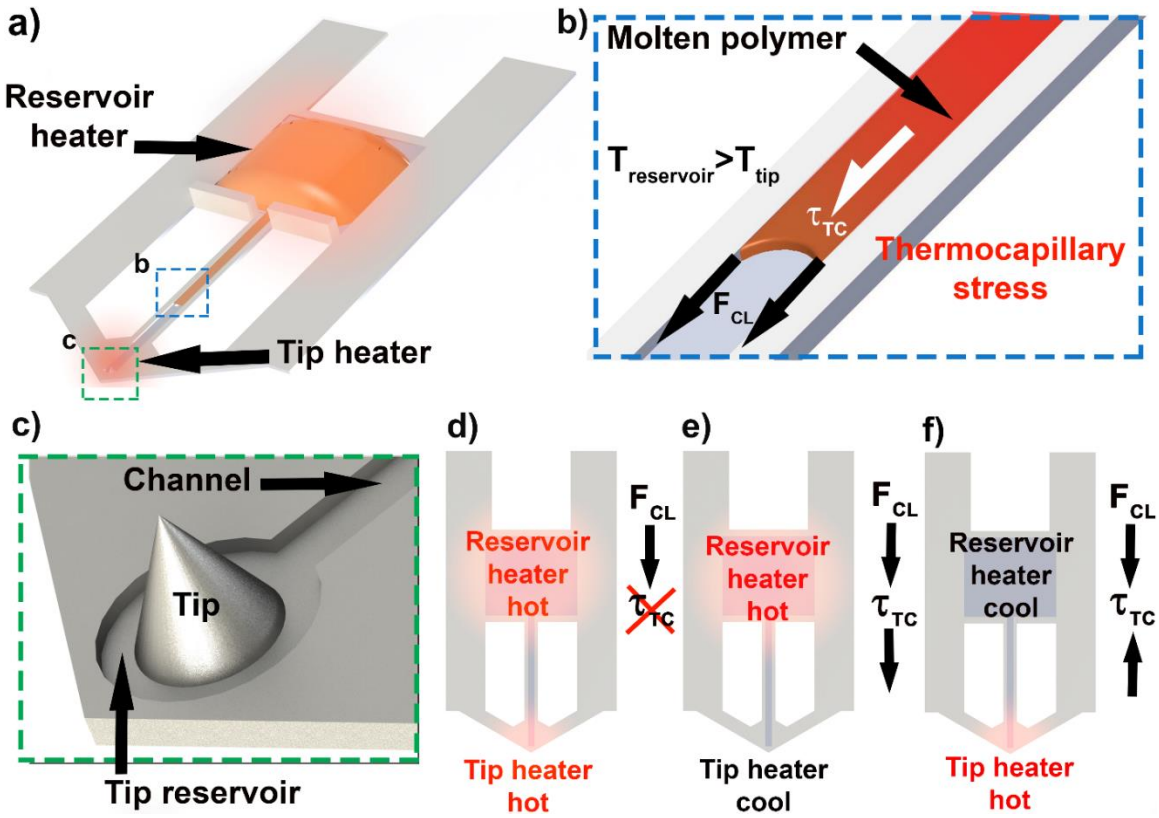

Figure 2.1 (a) Schematic of the cantilever design with embedded tip and reservoir heater. (b) Schematic of the channel with flowing molten polymer. (c) Schematic of the cantilever tip, channel and tip reservoir. (d) Schematic of the cantilever with both heaters are hot. (e) Reservoir heater is on, and the tip heater is off. (f) The tip heater is on, and the reservoir heater is off.

To ensure polymer from the reservoir does not interact directly with the substrate, the cantilever is operated with a 15˚ tilt (gravity driven flow is negligible with bond numbers typically ~1×10^{-5}). Separating polymer storage from the writing tip allows for more controllable polymer replenishment at the reservoir, such as *via* electrohydrodynamic printing, without significantly affecting the write process at the tip [35]. The design presented here provides a platform for wafer scale polymer nanostructure fabrication with the potential to manufacture heterogeneous polymer nanostructures with high throughput, multiple feature registration, and high spatial resolution.

2.2. Methods

Polymer flow along the microchannel redistributes mass on the cantilever, which shifts the frequencies of the cantilever resonant modes. Measuring these frequency shifts thus provides a measure of polymer distribution within the channel over time, provided the shifts are detectable. We calculate the effect of polymer distribution along the cantilever using a 3D modal analysis in ANSYS. The model simulated the first 4 cantilever modal resonances in the absence of damping effects. The cantilever was modeled as a fixed-free beam with cantilever motion restricted to vertical and longitudinal motion (torsion effects were excluded). The element size of the model was chosen such that the further size reduction had a negligible effect on the result. Figure 2.2 shows how the polymer mass redistributed along the cantilever body during the simulations, where the total polymer mass remained constant.

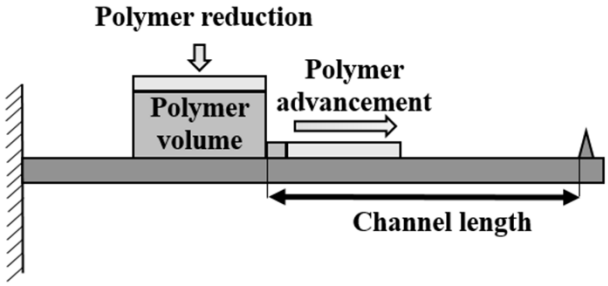

Figure 2.2 Schematic of the cantilever showing the concept of constant polymer mass on the cantilever during imbibing along the channel.

The modal response of the cantilever was calculated for different degrees of polymer imbibition within the microchannel, and changes in the resonant frequencies of the cantilever modes were correlated to polymer advancement through the microchannel. The contact mode between polymer and the cantilever surface was set as bonded with normal stiffness of 0.01 to avoid separation of polymer from the surface during the simulation. The resonant frequencies were simulated across a range of channel lengths and width for a cantilever with constant thickness of 1.5 µm and channel depth of 0.75 µm to determine the relationship between device geometry and mechanical dynamics.

The thermal gradient between the two heaters determines the extent of polymer mass flow control *via* thermo-capillarity. A steady state thermal-electric analysis was performed on the cantilever in ANSYS Multiphysics to determine the temperature response of the integrated Joule heaters. For thermal simulation, the cantilever geometry was fixed with a channel length of 100 µm, channel width of 5 µm, and a channel depth of 0.75 µm. The legs were high doped silicon, with a phosphorous doping level of 1×10^{20} cm^{-3}, the heater regions were low-doped silicon with a phosphorous doping level of 1×

10^{17} cm^{-3}, and the microchannel between the heaters was intrinsic silicon with an impurity doping level of 1×10^{14} cm^{-3}. Temperature dependent properties of silicon for all the regions and for air were taken into account, where both the local doping level and temperature determined the thermal conductivity and resistivity of each region of the cantilever [36]. Previous studies showed that heat transfers from silicon micro-heaters to the surroundings primarily *via* conduction through air, so the cantilever was enclosed in a 500 μm^3 air box with constant surface temperature boundary conditions [36, 37]. The base of the cantilever legs were held constant at room temperature to simulate the heat sinking behavior of the large silicon chip. A 10 kΩ resistor was placed in series with both the tip and reservoir heaters to limit instabilities in the current, as is common practice during actual device operation [38]. The temperature profile was then solved for while varying the input voltage to the legs of both the reservoir and tip heater.

The temperature gradient along the channel determines the magnitude of the thermocapillary stress on free surface of the imbibing molten polymer. Fluid dynamics of molten polymer flow in a microchannel was simulated in STAR-CCM+, where the flow was modeled as a three-dimensional multiphase (Eulerian) laminar flow using the volume of fluid (VOF) method with segregated flow and implicit unsteady solvers. The channel inlet was modeled as a stagnation inlet, the outlet and surface above the fluid free surface were treated as pressure outlets, and the channel wall boundaries were treated as no-slip boundaries with a constant fluid contact angle. A layer of air separated the fluid free surface and the top boundary to ensure that boundary effects did not alter the progression of the free fluid surface. Half the channel width was simulated with a symmetry boundary

condition. Experimental measurements show the contact angle between a molten polyethylene droplet and silicon dioxide surface is ~44˚, so the solid-fluid interface boundary condition was set by defining a constant contact angle of 45˚ [29]. The temperature gradient along the heaters was set to be either ±1000,000 ˚C /m, ±10,000,000 ˚C /m or zero and the temperature varied linearly along the channel, consistent with the thermal simulations. The surface tension linearly varied between 0.022-0.028 N/m over the temperature range of 160-260 ˚C, based on reported values for polyethylene (and is representative of many common polymers) [39-41]. In theory, Young's equation links the surface-liquid contact angle and the fluid surface tension such that the surface contact angle here would range between 25˚ - 45˚ assuming no change in the solid-gas and solid-liquid surface tensions. In practice, the solid surface has a variety of contaminants that also have temperature dependent surface tensions, making the actual contact angle variation much smaller. For this reason, contact angle was kept constant to remain conservative. The fluid dynamic viscosity of 0.001 Pa-s was chosen to improve convergence of the VOF method and set constant. While the viscosity of molten polymers are typically higher than the value chosen here, short time simulations at higher viscosities showed that the speed of the polymer front scales linearly with viscosity, consistent with scaling law analyses that show velocity is inversely proportional to viscosity for both capillary and thermocapillary driven flow. Thus, while the simulation does not provide accurate absolute fluid velocities, it captures how the thermocapillary force modifies the capillary flow in relative terms.

2.3. Results and Discussion

2.3.1. Mechanical Dynamics Analysis

Altering the distribution of mass along a cantilever [42-46] or the cantilever geometry alters the mode frequencies of the cantilever [42, 47, 48]. The resonance frequency of the micro-cantilever described here shifts as polymer flows into the microchannel due to the inherent redistribution of mass occurring. Therefore, the cantilever dynamics measurements could serve as a facile measure of the leading edge of polymer flow in the channel. This would be performed by first correlating cantilever resonant frequencies with optical measures of polymer imbibition, and then using the developed calibration to monitor subsequent mass flow without the aid of visual data [46]. Because oscillating the cantilever while writing in contact with a substrate would negatively impact polymer transfer, mass measurements would be taken periodically between writing events, sufficiently capturing changes over time provided total mass transfer is small between measurement events. A modal analysis of the cantilever vibration during operation shows the resonant frequencies of the first four cantilever modes are sensitive to the location of the advancing polymer meniscus within the channel. Frequency shifts were considered for wide (15 μm), intermediate (10 μm) and narrow (5 μm) channel widths to determine the effect of mass flow rate on frequency shift. For all the cases, the channel length and thickness were set to 100 μm and 0.75 μm respectively. Figure 2.3(a) shows the effect of the polymer imbibition length on the first resonance frequency. Here, damping effects were assumed to be small and ignored to better elucidate trends. It is worth noting that microcantilevers vibrating in viscous fluids exhibit spurious

vibrations, and such effects may be present in the current system due to large amounts of viscous polymer (although such spurious vibrations were not observed in previous studies of polymer-laden cantilever vibrations) [49, 50].

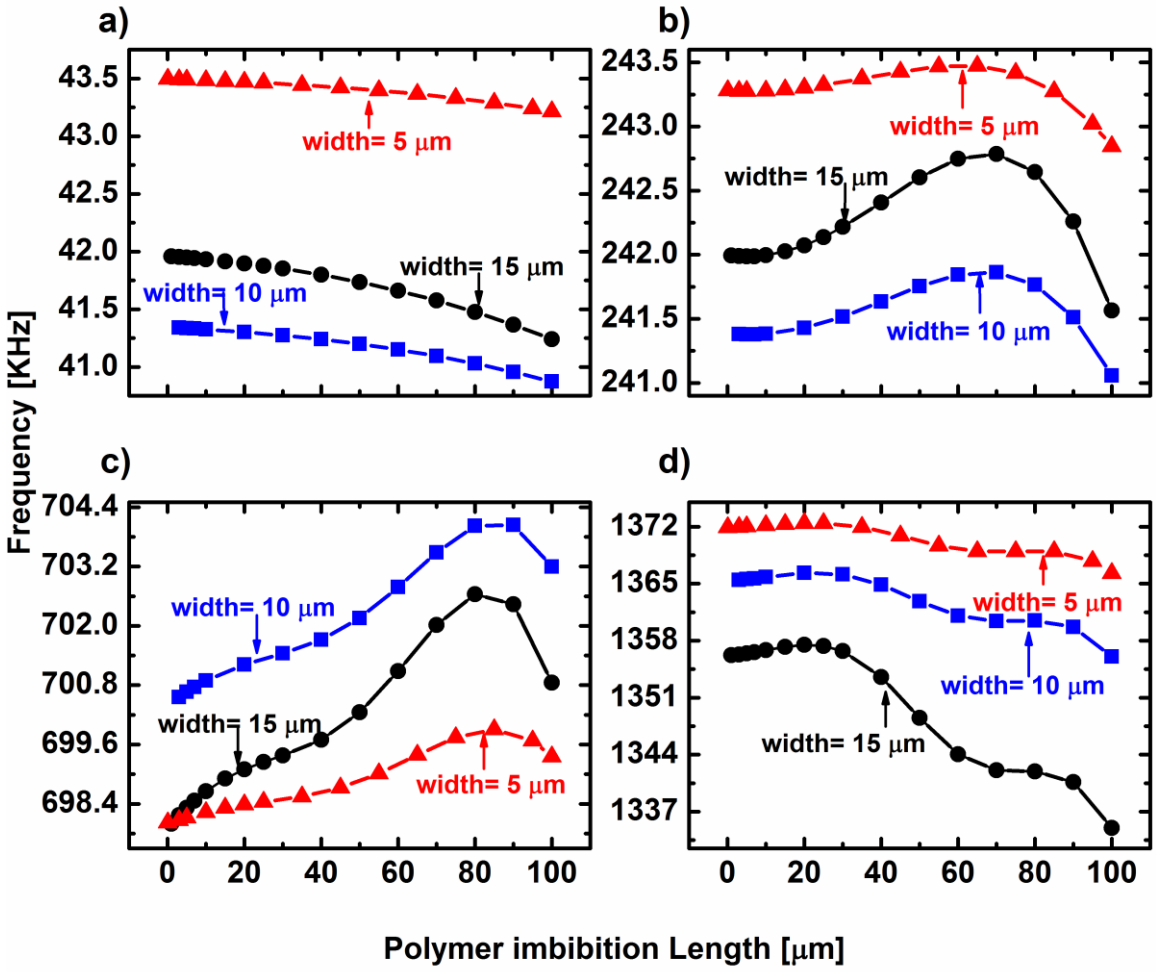

Figure 2.3 Results of dynamic simulation to show the effect of imbibition polymer length on the 1st (a), 2nd (b), 3rd (c), and 4th (d) resonance frequency of the cantilever with different channel widths**.**

The simulation results show a monotonic decrease of the first resonance frequency with increasing length of polymer within the channel for all the cases, with wider channels

showing larger shifts due to the larger overall changes in mass. Figure 2.3(b) shows the second mode frequency shift. Contrary to the first mode, the second mode experiences frequency shifts to lower or higher values depending on the location of the meniscus. For instance, the cantilever with the intermediate channel width shows the resonant frequency increasing up to an imbibition length of 70 μm, followed by a decrease in resonant frequency beyond 70 μm. The 3rd and 4th mode frequencies shown in figure 2.3(c-d) also exhibit non-monotonic behavior. The wide channel shows the maximum frequency shift between the initial and final location of the polymer meniscus position.

The total frequency shift between an unfilled and completely filled channel for the first four modes was simulated across a range of channel lengths and widths to understand how cantilever geometry alters the overall sensitivity to mass flow. Figure 2.4 displays the percent shift in mode frequency between a fully filled and completely empty channel with respect to the initial frequency of the cantilever as a function of the channel geometry. Figure 2.4(a) shows that the first mode frequency changes monotonically to larger shifts for longer, wider channels. Figure 2.4(b) shows the normalized second mode frequency shift, where the shift is no longer monotonic, with the maximum shift occurring for channel length between 180-200 μm and width between 8-18 μm. Figure 2.4(c) shows that the maximum frequency shifts for the 3rd mode occur for either short (length less than 50 μm) and wide channels (wider than 14 μm) or the maximum channel length and width. Figure 2.4(d) shows the maximum shift for the fourth mode occurs for channels with length between 100-120 μm and widths larger than 15 μm. Thus, although the first mode

does not provide much sensitivity for shorter, narrower channels, the increased sensitivity of higher modes may provide a method for measuring mass flow in smaller channels.

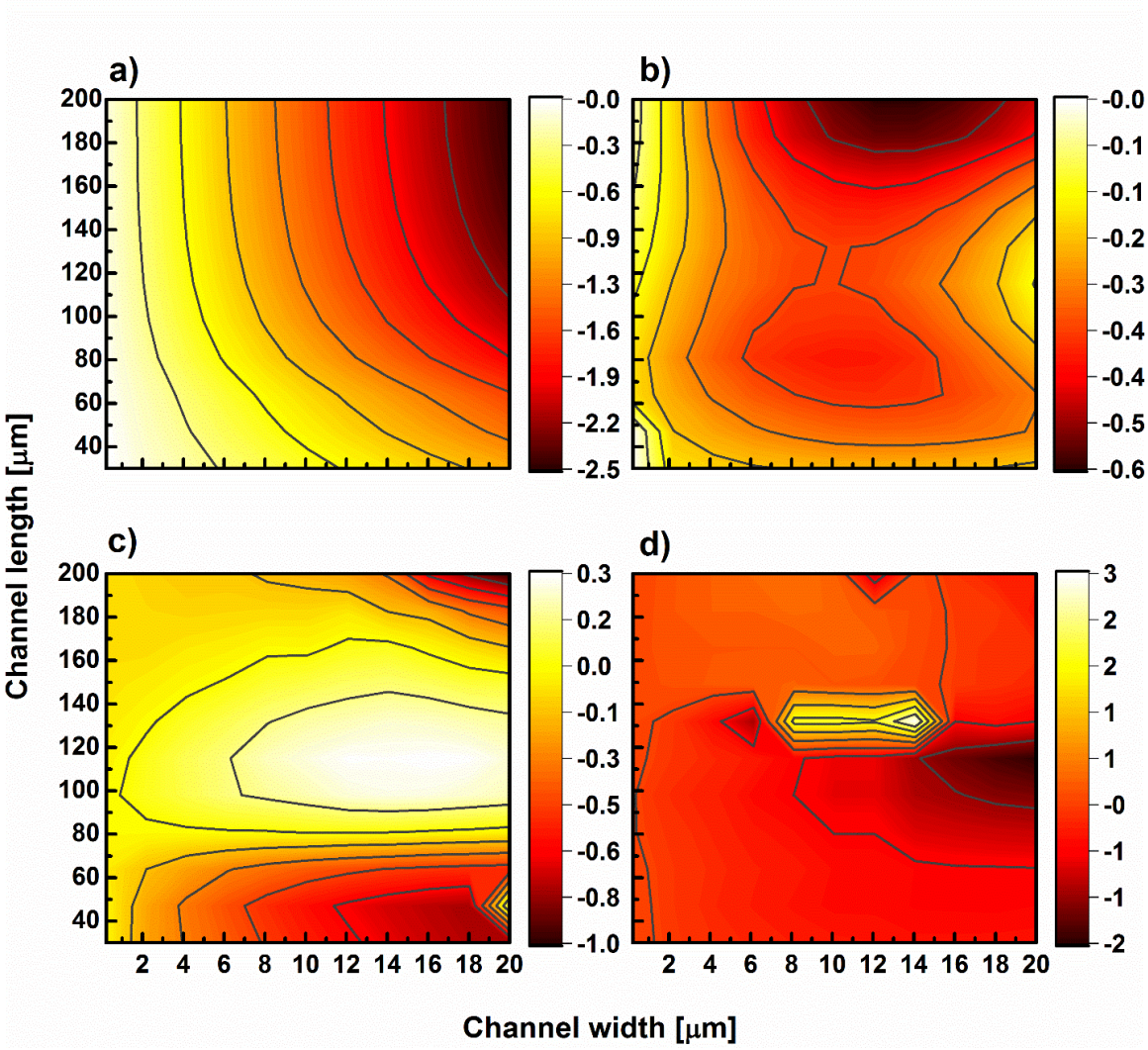

Figure 2.4 Percent frequency shift between an empty channel and a channel filled with molten polymer as a function of channel length and channel width for the 1st (a), 2nd (b), 3rd (c), and 4th (d) modes.

The ability to detect a shift in frequency depends on the quality factor of the vibration. Figure 2.5 shows sensitivity (calculated as the ratio between the frequency shift to the width of the mode frequency response assuming a constant quality factor) for the first four modes, assuming a quality factor ~50, which is commonly observed for commercial AFM cantilevers [51]. Peak shifts can be conservatively observed for sensitivities greater ~0.1. Figure 2.5(a) shows the sensitivity of the first mode shape as a function of channel length and width, where sensitivity is larger than 0.1 for all channel lengths and channel widths exceeding 4 μm. Figure 2.5(b) shows sensitivity for the second mode, where sensitivity values exceed the first mode particularly for channels less than 4 μm wide. Figure 2.5(c) shows the sensitivity of the 3rd mode, indicating it is particularly sensitive to very short channels. Figure 2.5(d) shows the sensitivity of the fourth mode which tends to be more sensitive for shorter channels. These results demonstrate that, depending on the size of the channel, different vibrational cantilever modes can be exploited to enhance sensitivity of mass flow measurements through the channel.

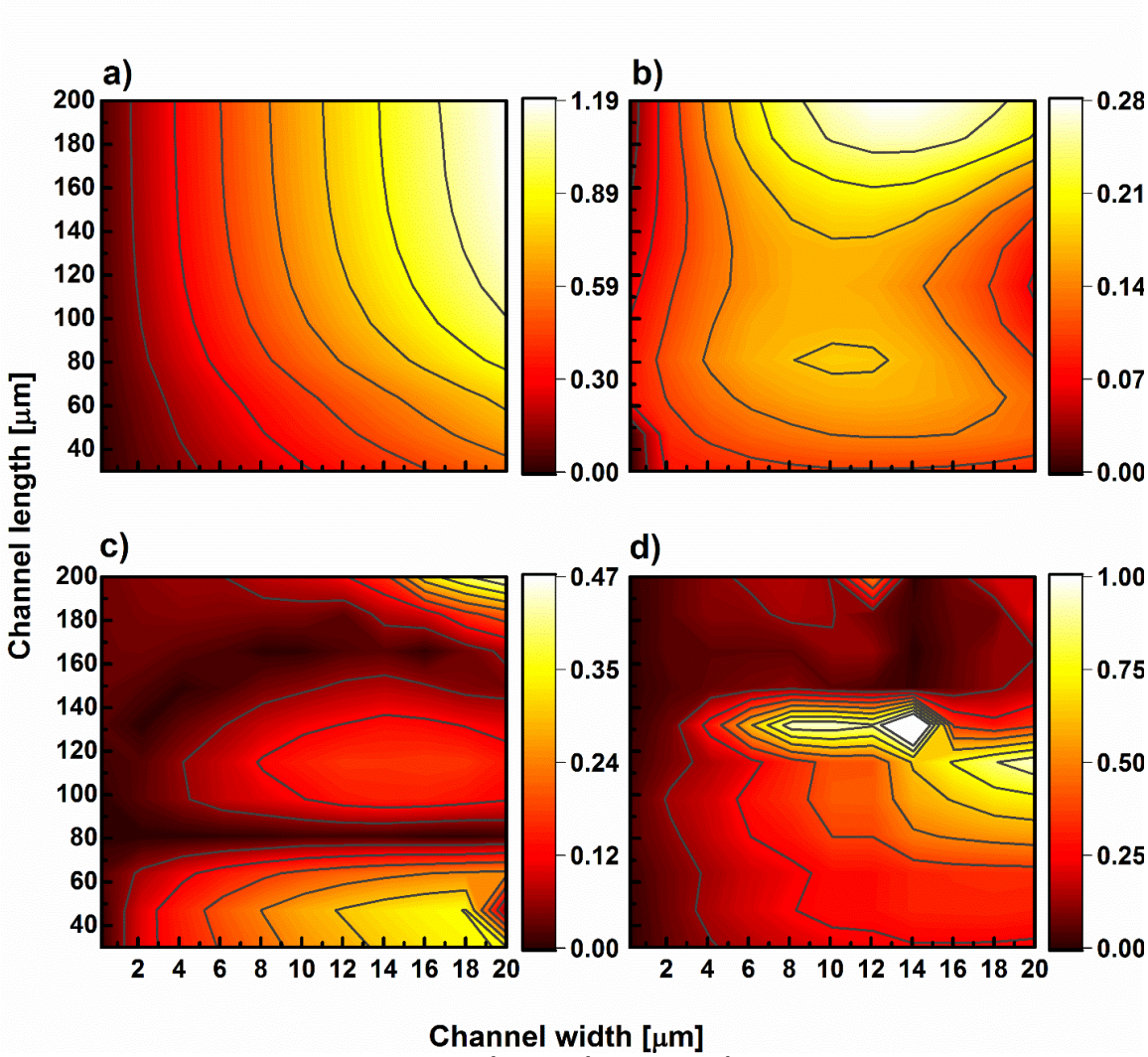

Figure 2.5 Sensitivity of the 1st (a), 2nd (b), 3rd (c), and 4th (d) mode shapes as a function of channel width and length, as defined by the magnitude of the frequency shift between and empty and filled microchannel relative to the width of a typical cantilever resonance peak in the frequency domain.

2.3.2. Thermal Analysis

Figure 2.6 shows a top view of the calculated temperature profile of the cantilever subject to both tip and reservoir heating (figure 2.6(a)), only reservoir heating (figure 2.6(b)), and only tip heating (figure 2.6(c)). The temperature distribution of the side

profiles of figure 2.6(a-c) are shown in figure 2.6(d-f) including the temperature distribution within the air surrounding the cantilever. The results show that a significant amount of heat diffuses both along the cantilever legs and through the surrounding air, where the thermal resistance of the air is large enough relative to the legs to cause a temperature rise in the unheated heater for both only tip heating and only reservoir heating. The thermal crosstalk between heaters fundamentally limits the ultimate temperature gradient achievable between the heaters. Figure 2.6(g) shows the maximum temperature of the tip and the reservoir for the case of only tip heating and only reservoir heating as a function of applied heater voltage for a heater separation of 100 μm. For the case of tip heating, there is a corresponding relative rise in temperature within the reservoir heater with respect to the tip of roughly 24% due to heat conduction from the tip to the reservoir. Conversely, reservoir heating results in a tip heater temperature relative rise of 31% with respect to the reservoir. Figure 2.6(h) shows the temperature profile along the channel between heaters for only tip heating, only reservoir heating, and both tip and reservoir heating. The results indicate that this design achieves temperature gradients of roughly ± 2,000,000 ˚C/m when the tip is held at 300 ˚C or the reservoir is held at 400 ˚C. Many polymers have glass transition temperatures below 200 ˚C and begin to degrade appreciably above 200 ˚C in the ambient environment, so typical operation of each heater at 200 ˚C results in temperature gradients of roughly ±1,000,000 ˚C/m.

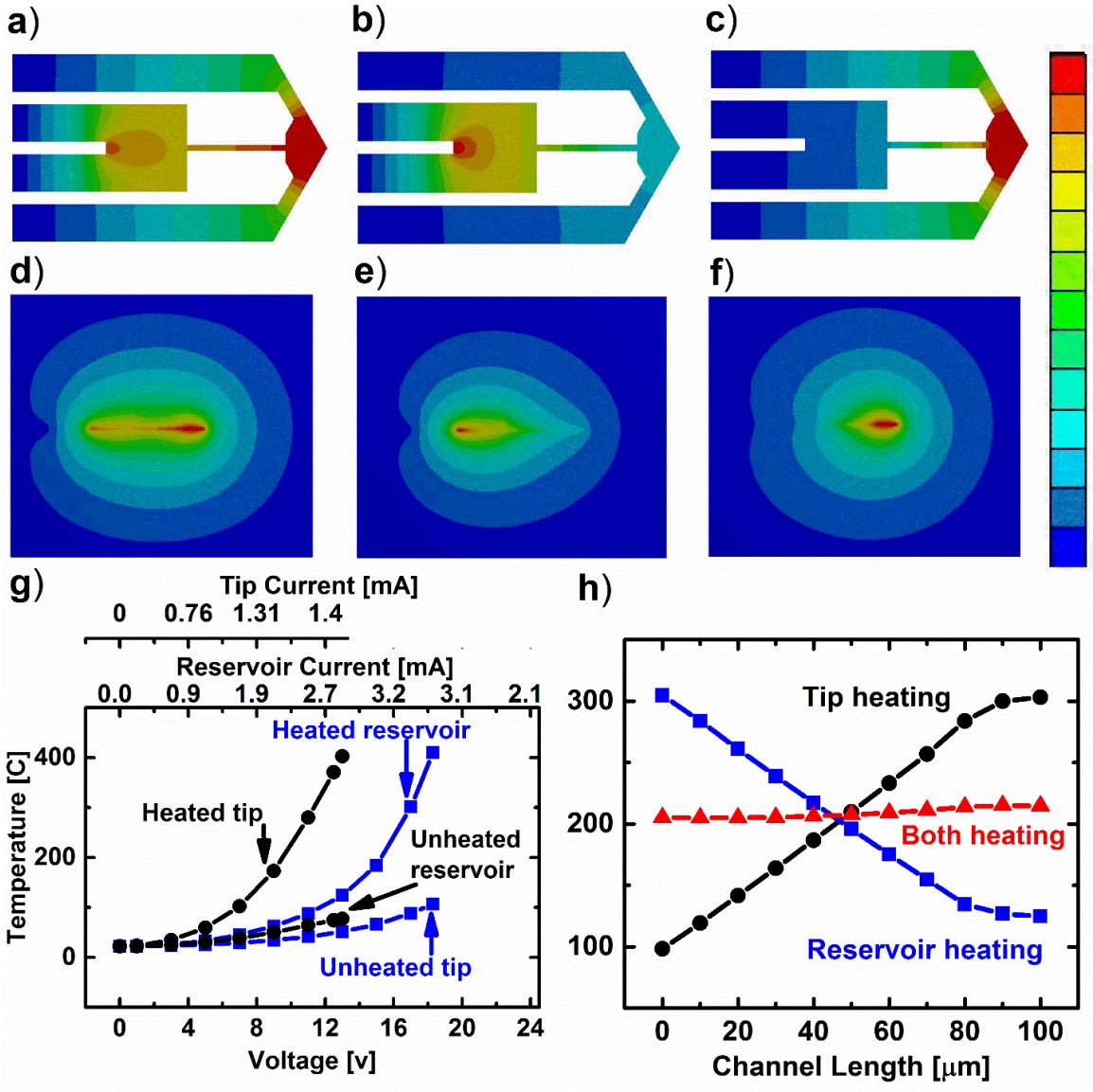

Figure 2.6 Thermal analysis of the cantilever. Top view of the cantilever temperature profile for simultaneous tip and reservoir heating (a), reservoir heating only (b), and tip heating only (c). (d-f) Side-view of the temperature profiles from (a-c) including the surround air environment. (g) The resulting maximum temperature of the tip and reservoir in series with 10 kΩ current-limiting resistor as a function of voltage applied to either the tip heater (black) or the reservoir heater (blue). (h) Temperature gradient along the channel during tip heating (black), reservoir heating (blue), and simultaneous tip and reservoir heating (red).

Interestingly, the temperature profile along the channel is linear, indicating that the surrounding air is sufficiently insulating to sustain nearly 1D thermal conduction along the channel, as opposed to the exponential temperature profiles expected with significant heat flow to the environment. Therefore, the temperature gradient along the channel, and thus the surface stresses experienced by the free surface of the fluid within the channel, is constant along the entire length. Finally, simultaneous heating of both heaters can set up a constant temperature profile along the channel, which effectively allows molten polymer transport solely due to surface tension forces on the advancing contact line.

Figure 2.7(a) shows the temperature difference along the channel of length 100 μm for different voltage values applied to the tip and reservoir heaters. By tuning the applied voltage input to each heater, the temperature difference between them can be modified between -200 — 200 ˚C. The white lines indicate isolines for the temperature difference between the heaters. The results show that a temperature difference between -100 –100 ˚C can be maintained over the entire range of operating voltages of the system. Figure 2.7(b) shows the maximum temperature of the reservoir heater as a function of voltage inputs to the heaters. For low reservoir voltages, the voltage applied at the tip heater significantly tunes the heater temperature. For high reservoir voltages, the temperature of the heater is largely controlled by the reservoir and only marginally modulated by the tip voltage. Conversely, figure 2.7(c) shows the reservoir temperature as a function of applied voltage to both heaters, where high applied tip voltages largely dictate the reservoir heater temperature.

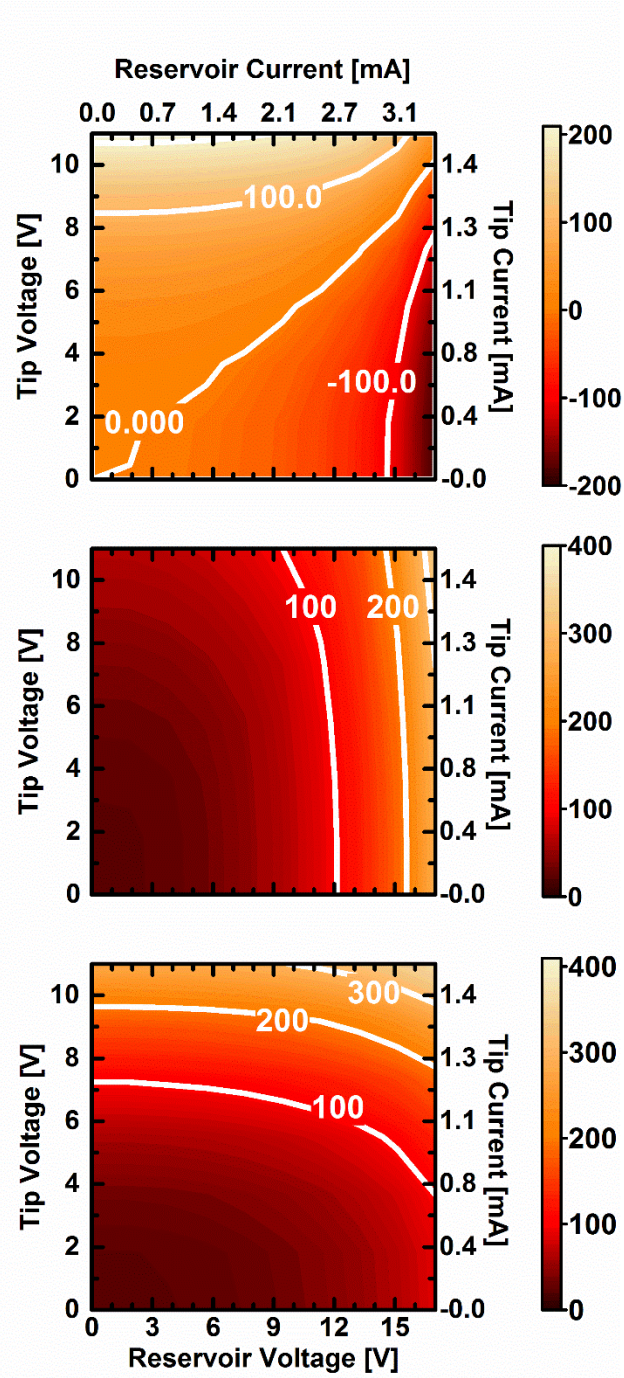

Figure 2.7 (a) Temperature difference along the channel for different applied heater voltages. The white lines indicate isolines for temperature difference values. (b) Reservoir temperature as a function of applied heater voltages. (c) Tip temperature as a function of applied heater voltages. For each heater a 10 kΩ current-limiting resistor in series is considered in all the cases.

2.3.3. Fluid Dynamics Analysis

Capillary motion in micro/nanochannels is a well-known phenomenon resulting from contact line forces at the advancing fluid front which are determined by the surface energy of the fluid, channel, and atmosphere [52, 53] . The classical Lucas-Washburn equation describes the dynamics of the fluid front within the capillary [54], which has been theoretically and experimentally validated down to the micrometer and nanometer scale [55-57]. For a circular capillary neglecting gravity and wall slip, the dynamics of the imbibing fluid front is described by:

$$\frac{dl}{dt} = \frac{\gamma r \cos\theta}{4\eta l} \qquad \text{(eqn 2.1)}$$

where η is the dynamic viscosity of the liquid, γ is the surface tension of the liquid, r is the channel radius, *l* is the fluid imbibition length and θ is the fluid contact angle. For a fluid advancing through an open channel subject to a temperature gradient, the temperature gradient along the fluid free surface induces a thermocapillary stress on the fluid surface [58, 59] that causes fluid to flow from hot to cold [58, 60]. The velocity of the fluid front is proportional to the thermocapillary stress as described below [58]:

$$\frac{dl}{dt} \propto \frac{h_0 \tau}{\eta} \qquad \text{(eqn 2.2)}$$

Where h_0 is the fluid centerline height, τ is the thermal stress and η is the fluid viscosity. Integrating the washburn equation shows that the fluid front displacement scales with $\sqrt{t}$, while the fluid front progression due to thermocapillarity scales linearly with *t,* indicating that thermocapillary stress will dominate for extremely long, slender channels and for very high thermocapillary stresses, both of which are true for the device

described herein. Fluid dynamic finite element simulations were carried out to investigate the effect of the magnitude of the themocapillary stress on the progression of the advancing fluid front within the heated channel. Figure 2.8(a) shows a schematic of the simulation, where fluid initially contained within a large reservoir is driven through a microchannel *via* both capillary line forces and thermocapillary stress on the fluid free surface (details of the simulation where described in a previous section). Figure 2.8(b) shows the relative effect of thermocapillary stress and capillary force on the advancing fluid front as a function of time. In the absence of a temperature gradient, the fluid flow closely resembles a modified Washburn equation specifically developed for open microchannel flow [57]. The discrepancy between theory and simulation results presented here are likely due to entrance effects within the first few microns as the meniscus curvature develops. Imposing a negative thermal gradient (where the tip is hot and the reservoir is cold) of -1,000,000 and -10,000,000 ˚C/m shows that the force on the fluid due to the thermocapillary stress opposes capillary filling, and balances the capillary forces at a distance less than 100 μm. Thus, the temperature gradients achieved by this device should be sufficient to stop and reverse flow within the channel for cleaning and re-inking the tip. Positive temperature gradients of +1,000,000 and +10,000,000 ˚C/m act constructively with the capillary force to increase the flow of polymer through the channel, dramatically reducing filling times during patterning. Thus, the results here demonstrate that the temperature gradient sustained by the proposed device is capable of dramatically increasing the speed of polymer flow within the microchannel, and is sufficient to stop

and reverse flow, both required features for scalable, robust tip based additive nanomanufacturing.

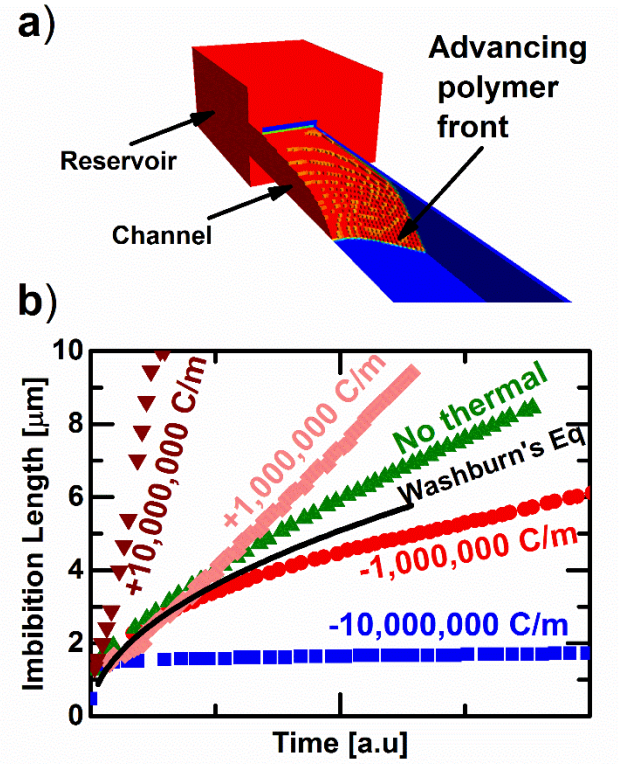

Figure 2.8 (a) Schematic of the thermofluidic finite element simulation, where the molten polymer flows from the reservoir through the channel by both capillary line forces and thermocapillary stress on the fluid free surface. (b) Thermo-capillary and capillary force effects on advancing fluid front as a function of time. The blue square and red dots show -10,000,000 ˚C/m and -1,000,000 ˚C/m thermal gradient respectively. The green color displays the channel with no thermal gradient (capillary forces are dominant here). The pink and maroon color show the channel with +1,000,000 ˚C/m and +10,000,000 ˚C/m thermal gradient thermal gradient respectively. The black line shows the imbibition length based on Washburn's equation.

2.4. Conclusion

We demonstrated an AFM cantilever design for patterning polymeric nanostructures with the ability to sense and control the polymer flow rate. Thermo-capillary forces govern polymer flow between two embedded joule heaters on the cantilever. Finite element analysis showed that the cantilever resonance frequency and sensitivity are a function of polymer imbibition length, and measuring frequency shift can provide a measure of fluid mass flow in the channel. Thermal analysis showed that the two imbedded Joule heaters could provide a thermal gradient range between -2,000,000 to 2,000,000 ˚C/m. We further showed that these thermal gradients could significantly accelerate or impede the flow of polymer within the integrated microchannel *via* thermocapillary stress on the fluid free surface. The designed cantilever is a significant step toward wafer scale patterning of heterogeneous polymer nanostructures with integrated mass flow measurement and control.

2.5. References

1. D. Morecroft, et al., *Sub-15nm Nanoimprint Molds and Pattern Transfer*. Journal of Vacuum Science & Technology B, 2009. **27**(6): p. 2837-2840.
2. T.K. Whidden, et al., *Pattern Transfer to Silicon by Microcontact Printing and Rie*. Nanotechnology, 1996. **7**(4): p. 447-451.
3. S.T. Han, et al., *Microcontact Printing of Ultrahigh Density Gold Nanoparticle Monolayer for Flexible Flash Memories.* Advanced Materials, 2012. **24**(26): p. 3556-3561.
4. Yu, G., et al., *Hybrid Nanostructured Materials for High-Performance Electrochemical Capacitors.* Nano Energy, 2013. **2**(2): p. 213-234.
5. G. Moad, et al., *Functional Polymers for Optoelectronic Applications by Raft Polymerization.* Polymer Chemistry, 2011. **2**(3): p. 492-519.
6. K. Nazrin, et al., *A Review of Roll-to-Roll Nanoimprint Lithography*. Nanoscale Research Letters, 2014. **9**(1): p. 1-13.
7. S.H. Ahn and L.J. Guo, *High-Speed Roll-to-Roll Nanoimprint Lithography on Flexible Plastic Substrates.* Advanced Materials, 2008. **20**(11): p. 2044-9.
8. B.W. Axelrod, M.L. Roukes, and J.L. Arlett, *Microfluidic Embedded Polymer Nems Force Sensors*. 2013.
9. L. Gang, R. Zhu, and Y. Yang, *Polymer Solar Cells.* Nature Photonics, 2012. **6**(3): p. 153-161.

10. L. Weiwei, et al., *Polymer Solar Cells with Diketopyrrolopyrrole Conjugated Polymers as the Electron Donor and Electron Acceptor*. Advanced Materials, 2014. **26**(20): p. 3304-3309.

11. Y. Gang, et al., *Polymer Photovoltaic Cells: Enhanced Efficiencies Via a Network of Internal Donor-Acceptor Heterojunctions.* Science-AAAS-Weekly Paper Edition, 1995. **270**(5243): p. 1789-1790.

12. S. Günes, H. Neugebauer, and N.S. Sariciftci, *Conjugated Polymer-Based Organic Solar Cells.* Chemical Reviews, 2007. **107**(4): p. 1324-1338.

13. A.C. Mayer, et al., *Polymer-Based Solar Cells.* Materials Today, 2007. **10**(11): p. 28-33.

14. M.V. Fabretto, et al., *Polymeric Material with Metal-Like Conductivity for Next Generation Organic Electronic Devices.* Chemistry of Materials, 2012. **24**(20): p. 3998-4003.

15. A.C. Arias, et al., *All Jet-Printed Polymer Thin-Film Transistor Active-Matrix Backplanes.* Applied Physics Letters, 2004. **85**(15): p. 3304-3306.

16. J. Liang, et al., *Elastomeric Polymer Light-Emitting Devices and Displays.* Nature Photonics, 2013. **7**(10): p. 817-824.

17. H. Yan, et al., *A High-Mobility Electron-Transporting Polymer for Printed Transistors.* Nature, 2009. **457**(7230): p. 679-686.

18. A. Facchetti, *Π-Conjugated Polymers for Organic Electronics and Photovoltaic Cell Applications†.* Chemistry of Materials, 2010. **23**(3): p. 733-758.

19. F. Hua, et al., *Polymer Imprint Lithography with Molecular-Scale Resolution.* Nano Letters, 2004. **4**(12): p. 2467-2471.

20. H. Lan and D. Yucheng, *Nanoimprint Lithography.* Lithography, Michael Wang (ED.), 2010.

21. C.T. Black, et al., *Polymer Self Assembly in Semiconductor Microelectronics.* IBM Journal of Research and Development, 2007. **51**(5): p. 605-633.

22. J. Bang, et al., *Block Copolymer Nanolithography: Translation of Molecular Level Control to Nanoscale Patterns.* Advanced Materials, 2009. **21**(47): p. 4769-4792.

23. J. Ok, et al., *Methanol Barriers Derived from Layer-by-Layer Assembly of Poly (Ethersulfone) S for High Performance Direct Methanol Fuel Cells.* Bulletin-Korean Chemical Society, 2008. **29**(4): p. 842-846.

24. A.A. Dameron, et al., *Molecular Layer Deposition of Alucone Polymer Films Using Trimethylaluminum and Ethylene Glycol.* Chemistry of Materials, 2008. **20**(10): p. 3315-3326.

25. K. Barton, et al., *A Desktop Electrohydrodynamic Jet Printing System.* Mechatronics, 2010. **20**(5): p. 611-616.

26. M.S. Onses, et al., *Mechanisms, Capabilities, and Applications of High-Resolution Electrohydrodynamic Jet Printing.* Small, 2015. **11**(34): p. 4237-4266.

27. S. Jin, et al., *Simple Fabrication of Single-and Multi-Layer Polymer Nanotubes by Spin-Casting Method within Anodized Aluminum Oxide (Aao) Templates.* Journal of Materials Chemistry, 2012. **22**(44): p. 23368-23373.

28. J. Martín, et al., *Tailored Polymer-Based Nanorods and Nanotubes by" Template Synthesis": From Preparation to Applications.* Polymer, 2012. **53**(6): p. 1149-1166.

29. Felts, J.R., et al., *Nanometer-Scale Flow of Molten Polyethylene from a Heated Atomic Force Microscope Tip.* Nanotechnology, 2012. **23**(21): p. 215301.

30. W.P. King, et al., *Heated Atomic Force Microscope Cantilevers and Their Applications.* Annual Review of Heat Transfer, 2013. **16**(16): p. 287-326.

31. J.R. Felts, et al., *Nanometer-Scale Infrared Spectroscopy of Heterogeneous Polymer Nanostructures Fabricated by Tip-Based Nanofabrication.* ACS Nano, 2012. **6**(9): p. 8015-8021.

32. W.K. Lee, et al., *Maskless Nanoscale Writing of Nanoparticle− Polymer Composites and Nanoparticle Assemblies Using Thermal Nanoprobes.* Nano Letters, 2009. **10**(1): p. 129-133.

33. Nelson, B.A., W. P. King, A. R. Laracuente, P. E. Sheehan, and L. J. Whitman, *Direct Deposition of Continuous Metal Nanostructures by Thermal Dip-Pen Nanolithography.* Applied Physics Letters, 2006. **88**(3): p. 033104-033106.

34. Chung, S., et al., *Temperature-Dependence of Ink Transport During Thermal Dip-Pen Nanolithography.* Applied physics letters, 2011. **99**(19): p. 193101-193103.

35. J.H. Pikul, et al., *High Precision Electrohydrodynamic Printing of Polymer onto Microcantilever Sensors.* Sensors Journal, IEEE, 2011. **11**(10): p. 2246-2253.

36. K.J. Kim and W.P. King, *Thermal Conduction between a Heated Microcantilever and a Surrounding Air Environment.* Applied Thermal Engineering, 2009. **29**(8): p. 1631-1641.

37. K.J. Kim, et al., *Nanotopographical Imaging Using a Heated Atomic Force Microscope Cantilever Probe.* Sensors and Actuators A: Physical, 2007. **136**(1): p. 95-103.

38. Somnath, S. and W.P. King, *An Investigation of Heat Transfer between a Microcantilever and a Substrate for Improved Thermal Topography Imaging.* Nanotechnology, 2014. **25**(36): p. 365501.

39. Roe, R.-J., *Surface Tension of Polymer Liquids.* The Journal of Physical Chemistry, 1968. **72**(6): p. 2013-2017.

40. S. Phongikaroon, et al., *Effect of Temperature on the Surface Tension of Soluble and Insoluble Surfactants of Hydrodynamical Importance.* Journal of Chemical & Engineering Data, 2005. **50**(5): p. 1602-1607.

41. V.B. Lazarev, *Surface Tension as a Function of Temperature for Some Molten Metals.* Theoretical and Experimental Chemistry, 1967. **3**(4): p. 294-295.

42. Arlett, J.L., and M.L. Roukes, *Ultimate and Practical Limits of Fluid-Based Mass Detection with Suspended Microchannel Resonators.* Journal of Applied Physics, 2010. **108**(8): p. 084701-084711.

43. B.T. Peter and S.R. Manalis, *Suspended Microchannel Resonators for Biomolecular Detection.* Applied Physics Letters, 2003. **83**(13): p. 2698-2700.

44. T.P. Burg, et al., *Weighing of Biomolecules, Single Cells and Single Nanoparticles in Fluid.* Nature, 2007. **446**(7139): p. 1066-1069.

45. S. Sadewasser, G. Villanueva, and J.A. Plaza, *Special Cantilever Geometry for the Access of Higher Oscillation Modes in Atomic Force Microscopy.* Applied Physics Letters, 2006. **89**(3): p. 033106-033109.

46. M.S. Hanay, et al., *Inertial Imaging with Nanomechanical Systems.* Nature Nanotechnology, 2015. **10**(4): p. 339-344.

47. G. Rinaldi, M. Packirisamy, and I. Stiharu, *Frequency Tuning Afm Optical Levers Using a Slot.* Microsystem Technologies, 2008. **14**(3): p. 361-369.

48. J.R. Felts and W.P. King, *Mechanical Design for Tailoring the Resonance Harmonics of an Atomic Force Microscope Cantilever During Tip–Surface Contact.* Journal of Micromechanics and Microengineering, 2009. **19**(11): p. 115008-115013.

49. Han, W., S. Lindsay, and T. Jing, *A Magnetically Driven Oscillating Probe Microscope for Operation in Liquids.* Applied Physics Letters, 1996. **69**(26): p. 4111-4113.

50. Mullin, N. and J. Hobbs, *Torsional Resonance Atomic Force Microscopy in Water.* Applied Physics Letters, 2008. **92**(5): p. 053103-053106.

51. L. Chen, X. Yu, and D. Wang, *Cantilever Dynamics and Quality Factor Control in Ac Mode Afm Height Measurements.* Ultramicroscopy, 2007. **107**(4): p. 275-280.

52. Phan, V.N., Pierre Joseph, Lyes Djeghlaf, Alaa El Dine Allouch, David Bourrier, Patrick Abgrall, Anne-Marie Gue, Chun Yang, and Nam-Trung Nguyen, *Capillary Filling in Nanochannels—Modeling, Fabrication, and Experiments.* Heat Transfer Engineering, 2011. **32**(7-8): p. 624-635.

53. Zhu, Y. and K. Petkovic-Duran, *Capillary Flow in Microchannels.* Microfluidics and Nanofluidics, 2010. **8**(2): p. 275-282.

54. Washburn, E.W., *The Dynamics of Capillary Flow.* Physical Review, 1921. **17**(3): p. 273-283.

55. J.M. Oh, et al., *Capillarity-Driven Dynamics of Water–Alcohol Mixtures in Nanofluidic Channels.* Microfluidics and Nanofluidics, 2010. **9**(1): p. 123-129.

56. J.W. van Honschoten, N. Brunets, and N.R. Tas, *Capillarity at the Nanoscale.* Chemical Society Reviews, 2010. **39**(3): p. 1096-1114.

57. Yang, D., et al., *Dynamics of Capillary-Driven Flow in Open Microchannels.* Journal of Physical Chemistry C, 2011. **115**(38): p. 18761-18769.

58. Darhuber, A.A., et al., *Thermocapillary Actuation of Liquid Flow on Chemically Patterned Surfaces.* Physics of Fluids, 2003. **15**(5): p. 1295-1304.

59. Darhuber, A.A. and S.M. Troian, *Principles of Microfluidic Actuation by Modulation of Surface Stresses.* Annual Review of Fluid Mechanics, 2005. **37**: p. 425-455.

60. Kataoka, D.E. and S.M. Troian, *Stabilizing the Advancing Front of Thermally Driven Climbing Films.* Journal of Colloid and Interface Science, 1998. **203**(2): p. 335-44.

3. POLYMER DROPLET WETTING: MEASUREMENT OF SPREADING WITH NANOSCALE RESOLUTION[2]

3.1. Introduction

Growing interest in utilizing polymers for organic photovoltaics, inkjet printing, self-healing coatings,[1, 2] microfluidics,[3, 4] data storage,[5-10] , photolithography[11-13] and nanocomposites has created a substantial need to understand how extremely small volumes of complex polymer fluids interact with non-trivial solid interfaces [14-17]. The spreading process is inherently complex, with a strong dependence on the long range surface forces between polymer and substrate, interactions between polymer molecules, confinement effects, surface chemistry, topography, contamination, and environmental composition. Thus, developing a comprehensive understanding of spreading requires experimental observation techniques with spatial resolutions orders of magnitude lower than conventional optical systems. Indeed, current experimental techniques are largely limited to macroscale observations of spreading of homogeneous fluids on atomically smooth surfaces, so studying more complex fluid-solid interfaces remains a significant challenge [18]. The dynamics of polymer spreading have been studied extensively at nanometer scales using molecular dynamic (MD) simulation, [19-21] but the lack of experimental observations of similar length scales has limited the value of simulation

[2] Reprinted from Soleymaniha, M. and Felts, J.R., 2018. Measurement of nanoscale molten polymer droplet spreading using atomic force microscopy. Review of Scientific Instruments, 89(3), p.033703. With permission from AIP

results. There is a need for experimental tools to study polymer spreading at the molecular level to understand the effects of volumetric confinement, rough and chemically modified surfaces, and fluid heterogeneity.

A number of experimental techniques have extensively validated many of the predicted behaviors of hydrodynamic spreading. For example, optical-based methods are widely used to study macroscale droplet spreading, where tracking the shape of the droplet over time provides information about the surface energies involved in the fluid-solid interaction, and how energy is dissipated as the droplet spreads [22-25]. Although this method has been established for macroscale droplets, it fails to capture the microscopic interactions happening at the solid-liquid contact line and is not able to measure droplets with sub-micron diameters. Ellipsometry provides sub-nanometer resolution perpendicular to the substrate by precisely measuring changes in surface optical constants due to the presence of fluid, and has been used to extensively study the molecularly thin precursor that propagates ahead of the contact line when a droplet completely wets a surface [22, 26-33]. However, the ellipsometer spot size is on the order of 10 μm, making it difficult to resolve microscale and nanoscale heterogeneity in the fluid and the surface. Measuring the complex spreading behavior of heterogenous systems requires spatial resolutions below 100 nm in three dimensions with detection sensitivity capable of identifying the variable compositions of both the fluid and the surface.

We have developed a technique for measuring spreading dynamics at the nanometer scale using Atomic Force Microscopy (AFM). The experimental setup uses a

heater stage to initiate melting of polymer beads and subsequent fluid spreading while a tapping mode AFM tip monitors how the polymer bead geometry evolves in time. AFM has previously been used to investigate spreading of molten polymer microbeads [34-36] but lacked the thermal, temporal and spatial resolution to make quantitative conclusions about the spreading dynamics. Here we overcome the limitations of previous studies through a variety of control and analysis algorithms. Although the utilized instrument is a well-known and ubiquitous tool, the data analysis and measurement methodologies developed here extend the capability of the AFM to measure important classes of dynamic processes not easily measured otherwise. The AFM compensates for thermal drift by observing and compensating for lateral motion of the droplet between images. A number of post-processing algorithms determine the droplet height, radius, and contact angle from the raw AFM data. Additionally, the shape and orientation of the tip is accounted for by monitoring the asymmetric artefacts introduced into the droplet shape. The AFM spatial resolution is 0.2 nm in height and less than 100 nm in lateral direction, which is sufficient for measuring single molecule thick structures and heterogeneity due to variations in orientation and composition of various polymer domains.[37, 38] We demonstrate the utility of the developed technique to observe the spreading of polystyrene microdroplets as a function of surface temperature and spreading time, where the high lateral resolution resolves the dynamics of semi-crystalline polystyrene domains on the surface of the bead, not measureable by any other means.

3.2. Theory of Polymer Spreading

Studies of liquid-solid interactions are traced back to Young's work [18] where the macroscopic static contact angle is defined by balancing surface tension forces between solid/liquid/vapor phases at the triple point. Different wetting states can be distinguished depending on the spreading coefficient value defined as: [26]

$$S_{eq} = \sigma_{lv}(\cos\theta_{eq} - 1) \qquad \text{(eqn 3.1)}$$

Where σ_{lv} is the surface tension between liquid and vapor, and θ_{eq} is the equilibrium contact angle between liquid and solid. Complete wetting generally occurs when $S \geq 0$, in which the fluid spreads over the solid, and wets the surface with the equilibrium shape that is defined by van der Waals, electrostatic and steric force components.[39-41] On the other hand, $S<0$ results in a droplet with a non-zero contact angle due to minimization of system free energy. Here, we deal with the latter regime where the polymer droplet dilates and reaches an equilibrium shape over time.

Droplet wetting forces are balanced theoretically by either bulk viscous dissipation (the hydrodynamic model), molecular kinetic theory (MKT) involving an energy barrier to liquid adsorption at the contact line, or combined models incorporating multiple dissipation mechanisms [30]. The hydrodynamic model dissipates the spreading force through viscous friction within the bulk of the droplet, ignoring surface chemical adsorption barriers [42, 43]. Another approach is based on molecular kinetic theory of Eyring [44], which neglects the bulk viscous dissipation and acknowledges the slippage and adsorption of the fluid particle on the solid surface as the dominant dissipation channel [45, 46]. Previous studies of partial wetting have shown that both types of dissipations

likely co-exist during the spreading [20, 41]. Therefore, balancing the spreading force and the combined dissipation due to bulk viscous flow and molecular kinetics at the surface provides an expression for the velocity of the droplet contact line over time: [41]

$$\dot{R}(t) = \frac{\gamma(\cos\theta_e - \cos\theta(t))}{\zeta_0 + 6\eta\phi[\theta(t)]\ln\left[\frac{R(t)}{a}\right]} \quad \text{(eqn 3.2)}$$

where η, γ and θ_e denote viscosity, surface tension of polymer, and equilibrium contact angle, respectively. The first term in the denominator, ζ_0, comes from the MKT model and is roughly considered a surface friction coefficient, [47] and *a* defines a radius of fluid far from the contact line that experiences negligible dissipation (indeed, the velocity must be zero at the center due to symmetry). The physical origin of *a* is somewhat undefined, as its existence arises to relax the now well-known singularity in the conventional hydrodynamic description of droplet spreading, and is roughly expected to be on the order of the fluid molecule size. The parameters *a* and ζ_0 are set as fitting parameters for fitting experimental data with the analytical solution. Independently, both theories of spreading predict a power law dependence in time for the expansion of the droplet contact radius, $R(t) \propto t^n$, where *n* is the power exponent. The hydrodynamic theory of spreading predicts *n* = 1/10, while the MKT predicts *n* = 1/7, and it is expected that the combined theory would predict a value between these two values. The contact angle also follows a power law dependence on time, where the power exponent is roughly -*3n* as a result of the spherical cap approximation [20]. Thus, evaluation of the fitting parameters *a* and $\zeta_0$as well as the resultant power law exponent provides some indication of whether contact line dissipation or bulk viscous dissipation is the dominant dissipation channel for a specific liquid-solid interaction.

The approximation function $\phi[\theta(t)]$ represents the geometrical relationship between the droplet base radius and contact angle, determined by assuming that the droplet keeps a spherical cap shape and conserves volume during spreading: [41]

$$\phi[\theta(t)] = \frac{[1+\cos\theta(t)]\ \sin\theta(t)}{[1-\cos\theta(t)]\,[2+\cos\theta(t)]} \qquad \text{(eqn 3.3)}$$

Thus, experimentally measured contact angles can approximate $\phi[\theta(t)]$ to determine the amount of viscous dissipation occurring in the droplet wedge over time. In the absence of significant surface friction effects, the time dependence of the contact angle and radius are -0.3 and 0.1, respectively which were previously derived by Tanner.[48] When friction forces dominate and viscous dissipation is negligible, the instantaneous radius and contact angle follow the power law with values of 0.14 and -0.42, respectively as calculated by Blake [41, 47].

3.3. Experimental Setup

Figure 3.1 shows the AFM setup, in which a nanometer size tip at the end of the cantilever scans the polymer surface by intermittently tapping the surface (AC mode). In this mode, the cantilever is brought to oscillation near its resonance frequency and touches the surface intermittently. Contact between the tip and surface alters the cantilever oscillation amplitude and phase [49]. A laser beam projected onto the cantilever surface and reflected into a photodiode tracks the cantilever vibration as the tip scans over the surface. Therefore, the intermittent contacts of the tip with the surface provides a measure of topography via changes in vibration amplitude and a measure of surface stiffness through variations in phase. All measurements in this study are performed on an MFD-3D

(Asylum Research, Inc., Santa Barbara, CA) loaded with MicroMasch HQ:NSC36/NO AL Cantilevers.

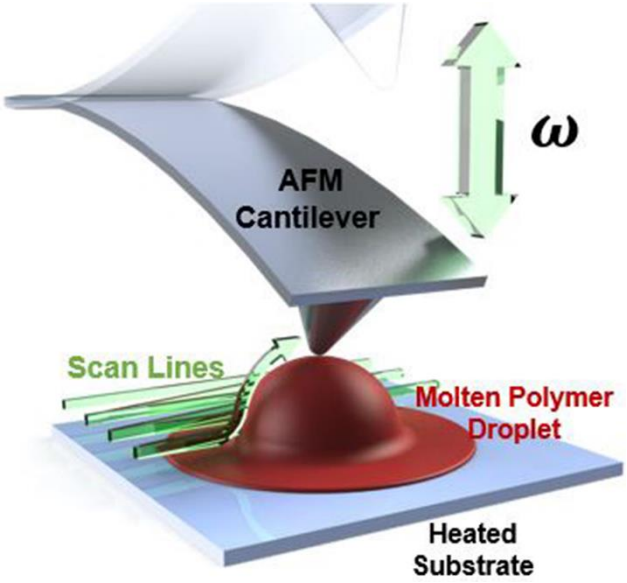

Figure 3.1 Graphical representation of an atomic force microscope tip measuring the profile of a spreading molten polymer droplet in tapping mode vibrating with amplitude of ω.

Polymer beads are formed using a previously developed dispersion polymerization technique to synthesize styrene colloids [50]. Controlling the initial conditions such as initiator and styrene concentration, temperature, stir speed and reaction time determines the molecular weight and diameter of uniform colloidal polystyrene spheres. The resulting monodisperse polystyrene beads in our experiment are roughly 2 μm in diameter. The measured weight average molecular weight (M_w) using gel permeation chromatography (GPC) is 48.2 kg/mol. The polymer solution is dispensed onto a sample surface by pipette at a concentration of 0.05 mg/mL, and the solvent evaporated before beginning

experiments. All the surfaces are cleaned with Acetone and isopropanol (IPA) and dried with Nitrogen. Then, samples are mounted on magnetic specimen holder via silver paint and placed into the AFM at room temperature and a suitable isolated sphere is identified using AFM.

The surface temperature is raised slowly (2 ºC /min) by the heater stage (Asylum PolyHeater with 0.2°C precision and 0.5°C accuracy) up to glass transition temperature of the polystyrene bead (110 ºC) while imaging the single bead. All the reported temperature values are for the heater stage not the polymer droplet. Ideally, the heater stage-silver paint-magnetic pock-substrate can be modeled as a series of thermal resistances to derive the temperature drop between the heater stage and the substrate. Since the conduction heat transfer between the heater stage and the sample surface is equal to convection heat transfer between the sample surface and the ambient air, by considering a simple 1-D steady state heat transfer problem we have;

$$h_{air}(T_{sub} - T_{amb}) = \frac{T_{sub} - T_{heater}}{\sum R_{total}} \qquad \text{(eqn 3.4)}$$

Where, h_{air} is the air convective heat transfer coefficient and is approximated to be 50 W/m^2·K. T_{amb} is the ambient temperature of 30 ℃. T_{heater} is the reported heater stage temperature which is 115 ℃. R_{total} is the total thermal resistance between heater stage and the substrate, estimated as 0.00041 m^2.K/W.This estimation is the sum of: 1. the resistance of magnetic pock with conductivity of 26.1 W/m.K and thickness of 800 µm, 2. silver paint with approximate thickness of 500 µm and conductivity of 406 W/m.K and 3. silicon substrate with thickness and conductivity of 500 µm and 1.3 W/m.K, respectively. By

solving the above equation to derive T_{sub}, the calculated temperature drop turns out to be about 1.6 ℃ and is negligible.

Particle tracking algorithms built into the AFM measure thermal drift of the particle over time and compensate to keep the bead centered in the scan over the entire experiment. It is important to note the risk of both tip fouling and tip-induced fluid motion, which would negatively bias the spreading dynamics. Since polystyrene is a hydrophobic, non-polar polymer, we did not observe significant AFM tip fouling or tip-induced smearing of fluid around the spreading droplet. However, we did observe a film transferred from the tip to the clean surroundings for wetting polymers like PMMA, making it important to functionalize tips to prevent contamination when working with wetting fluids. Each scan takes roughly 4 minutes, significantly faster than the spreading time of the droplets, which in this experiment is on the order of hours to days. The topography data from the AFM is post processed using custom Matlab code to extract the height, radius, and contact angle of the spreading droplets over time. The code reads the acquired individual images from AFM software during measurement and creates a time-evolving data set. The algorithm then finds the center of the droplet in the image, and divides the droplet into a set number of equally sized sectors. The contact angle and radius of the droplet at each instant of time is then determined for each sector by locating the edge of the droplet contact and fitting a line tangent to that point, and the total volume is recorded by integrating over the topography of the droplet. Figure 3.2(a) and 3.2(b) show typical contact angle and the contact radius measurements as a function of circumferential angle around the droplet for initial, middle and final stages of polystyrene spreading on

sapphire. At short times and large contact angles, the shape of the AFM tip tends to convolute the measured shape of the droplet, resulting in strong angle dependence on these values. In contrast, for later stages of spreading when the AFM tip predominantly contacts the fluid only at the tip apex, there is little observed convolution.

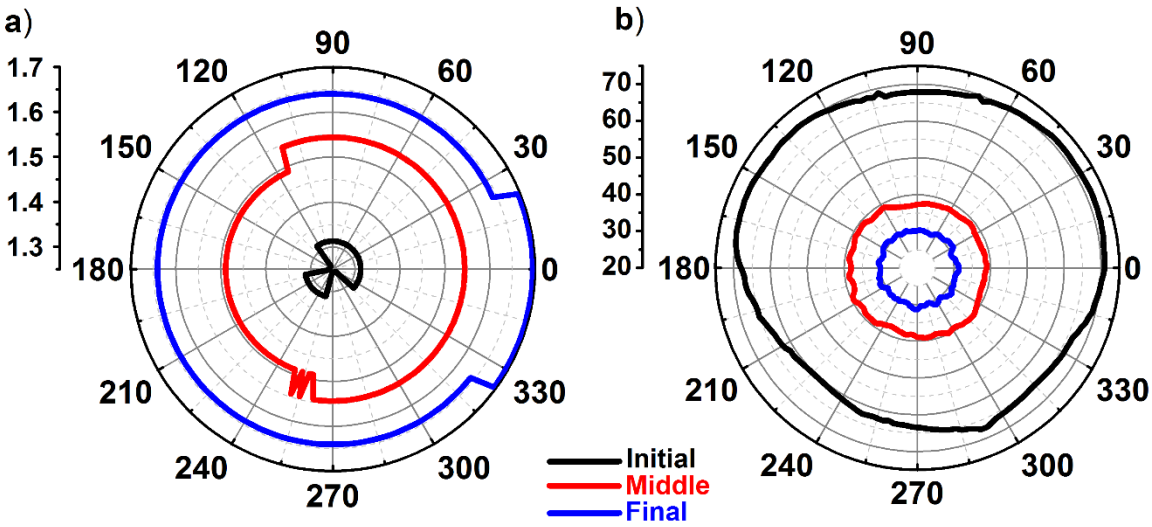

Figure 3.2 (a) Radius and (b) Contact angle as a function of circumferential angle around the polymer droplet.

Additionally, the phase data of the AFM oscillations provides a measure of the surface stiffness, which is utilized here to track crystalline structures on the surface of the amorphous molten polymer liquid. Previous AFM studies on polymer blends and polymer crystals showed that polymer composition and degree of polymer crystallinity affects the local stiffness of the material, which can be resolved qualitatively in the cantilever phase during tapping mode imaging [51-53]. In an attempt to isolate the effect of crystallinity on spreading behavior, we measure the spreading properties of polystyrene micro-beads

as a function of time on atomically smooth silicon oxide, mica and aluminum oxide (sapphire) with measured RMS roughness values of 1.08 nm, 1.23 nm and 90 pm respectively, which are common in micro and nano-fluidic devices, to validate the technique. To test reproducibility of the technique, we have repeated it over 10 times on SiO_2 surfaces with roughness of 10, 20 and 50 nm and on PS beads within the range of 50 nm and 30 μm.

3.4. Results and Discussion

Figure 3.3(a) shows 3D topography data of a spreading in atmosphere over time of a 2 μm diameter polystyrene bead on a sapphire surface at 115 ºC (above the 90 ºC glass transition temperature of the polystyrene). Figure 3.3(b) shows the measured contact angle over time. At short times, the AFM cannot track the large contact angle of the spreading droplet, which is hidden beneath the droplet radius for contact angles > 90˚. As the droplet spreads, the tip begins tracking the contact line, but convolution with the pyramidal tip geometry generates a large spread in the contact angle measurements, as evidenced by large experimental variance for contact angles between 60-80˚. Below 60˚, the tip geometry no longer significantly affects the measurement, and contact angle measurements becomes uniform with an experimental error of approximately ±0.6˚. After 400 minutes of scanning a molten bead, the contact angle reached an equilibrium value of 30˚ (measurement is taken farther until equilibrium value but is not shown here for clarity), consistent with the dynamics of partially wetting liquids on solid surfaces [54]. Figure 3.3(c) shows the measured radius and height of the droplet over time, where the height of the droplet is the maximum height between droplet and substrate, and the radius is

calculated with a height cutoff of roughly twice the substrate surface roughness (~1 nm for the polished and cleaved surfaces used here).

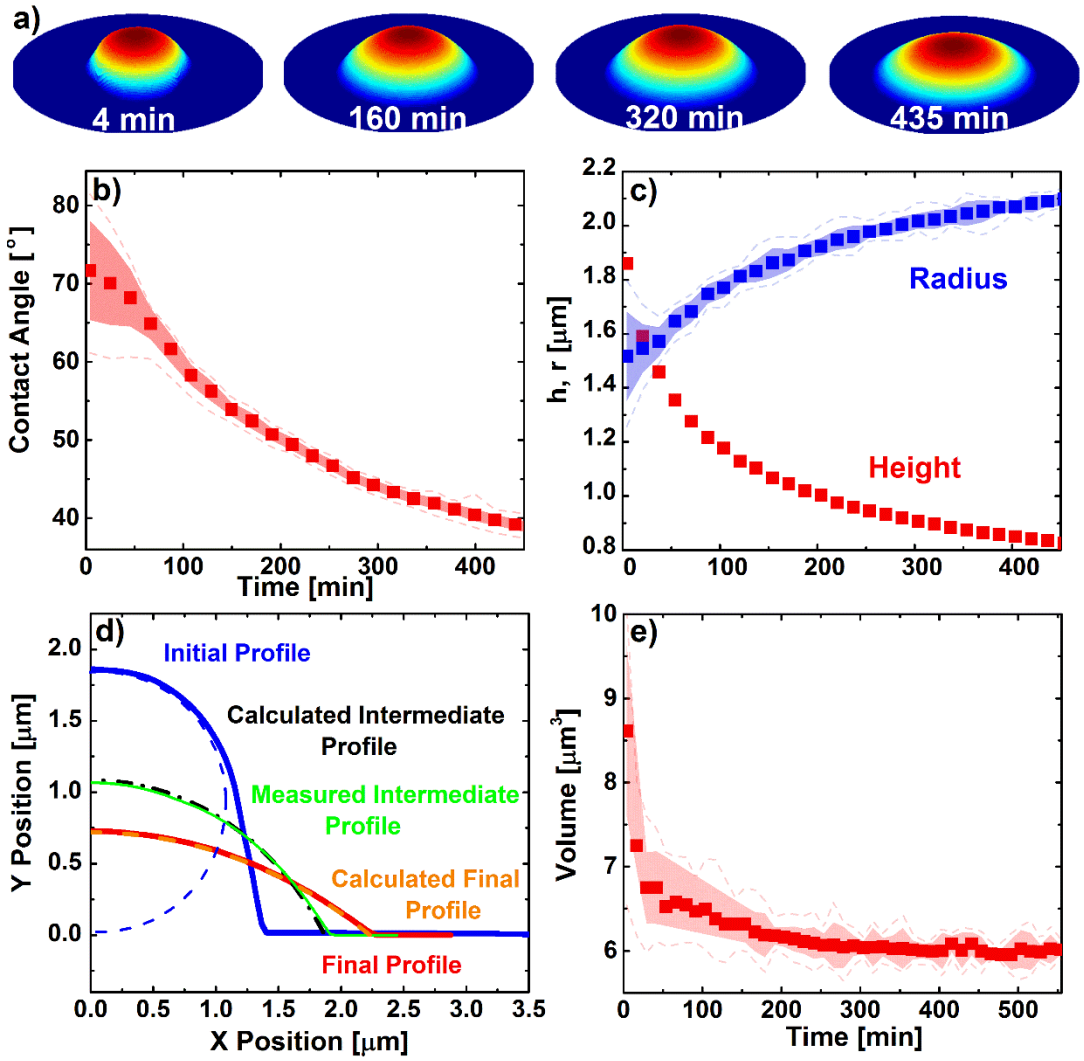

Figure 3.3 (a) 3D profile of a spreading polystyrene droplet on sapphire surface over time. (b) Measured contact angle of droplet over time. (c) Measured contact radius and droplet height over time. (d) The initial and final profile of the droplet over time. (e) Droplet volume change over time.

Figure 3.3(d) shows the initial, intermediate and final droplet shape, where the shape of the droplet is well approximated by a spherical cap at long times. At short times, the AFM does not accurately capture the void spaces present underneath the spherical polymer bead. Figure 3.3(e) shows the volume of the droplet as the function of time. The volume measurements at short times clearly illustrates the tip convolution error, where the volume under the sphere appears larger due to the void space. As the contact angle reaches 60˚, the measured droplet volume became nearly constant, indicating that the void spaces no longer exist and the AFM tip begins tracking the spreading droplet contact line. Although no precursor film was detected in this experiment, the slowly evolving volume of the droplet does not preclude the existence of a molecularly thin precursor of thickness comparable to the substrate roughness, and is the focus of future study.

Figure 3.4 shows the spreading dynamics of the 2 μm polystyrene droplet at 115 ºC on three substrates including silicon oxide (blue), sapphire (red), and cleaved mica (black). Figure 3.4(a) shows the contact angle dynamic measurement on the substrates. For the case of SiO2, the polystyrene quickly equilibrates to a large contact angle of 55˚, as expected based on previous studies of thin film PS dewetting studies on similar substrates [55]. For both the alumina and freshly cleaved mica surfaces, the polymer continues to spread according to a power law for at least 10 hours of measurement. Figure 3.4(b-c) show the height and radius time evolution, where the height decreases and the radius increases as spreading proceeds.

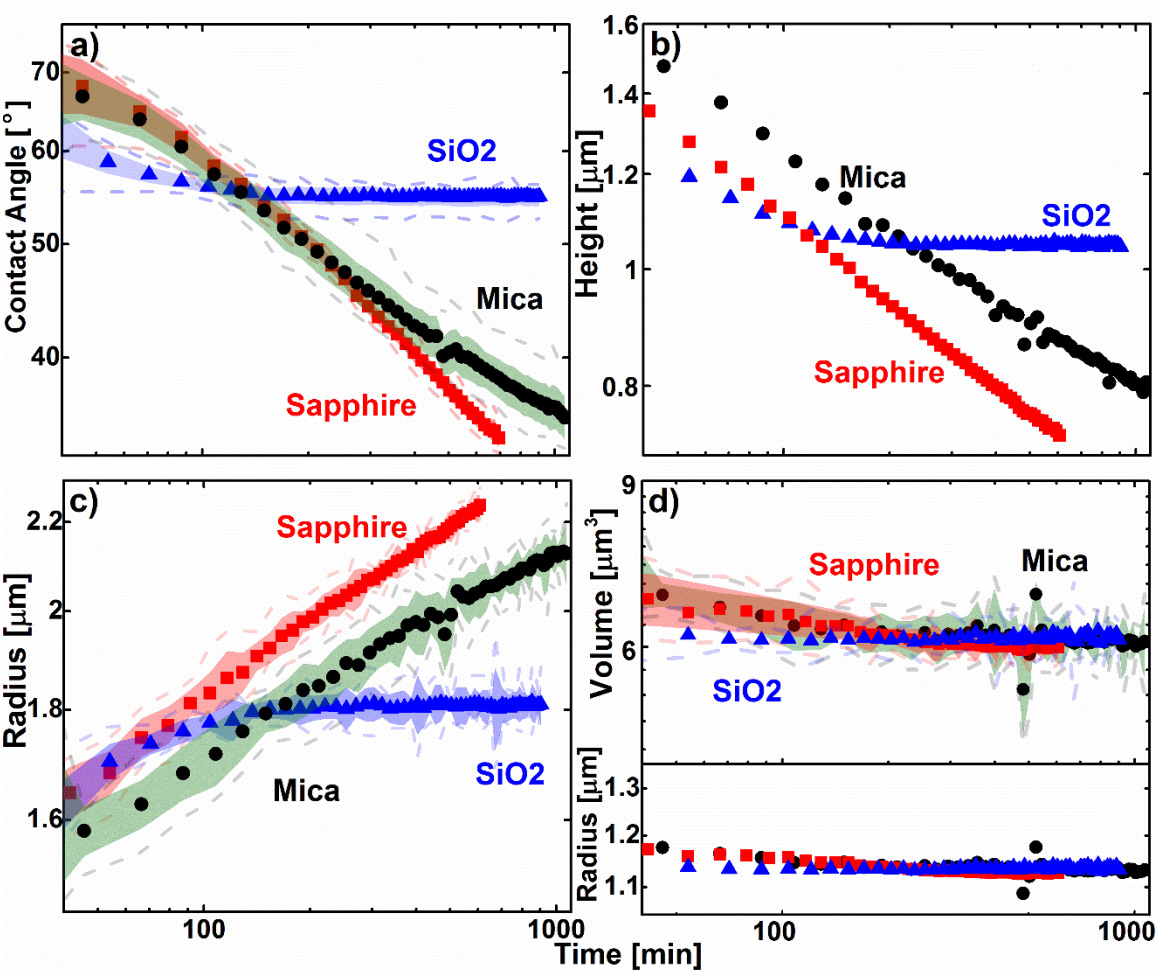

Figure 3.4 The dynamics of polystyrene spreading on sapphire (red rectangles), silicon oxide (blue triangles), and cleaved mica (black circles). The measured quantities are (a) contact angle, (b) height, (c) contact radius, and (d) apparent volume and equivalent radius of volume assuming a sphere geometry.

Figure 3.4(d) shows the changing volume of the sphere and the calculated effective sphere radius, indicating that the AFM tip effectively captures the geometry of the droplets for all times after ~100 minutes. The measured dynamic contact angle follows a power law decay as $t^{-0.08 \pm 0.02}$, $t^{-0.29 \pm 0.01}$ and $t^{-0.21 \pm 0.01}$ for SiO_2, sapphire and mica, respectively. The droplet base radius similarly follows a power law of $t^{0.11 \pm 0.03}$, $t^{0.12 \pm 0.01}$ and $t^{0.09 \pm 0.01}$ for

SiO_2, sapphire and mica correspondingly. A precursor film growing from the contact line was expected for the sapphire surfaces based on previous capillary filling experiments of polystyrene in alumina pores. Those experiments show a transition temperature at ~170 ºC where the spreading shifts from partial wetting (capillary filling) to fully wetting regime, and attribute the tube-like structures formed to an advancing precursor film [56]. Here, a precursor film does not emanate from the droplet contact line on flat alumina for temperatures up to ~230 ºC. The lack of precursor film formation could be from contamination of the substrates, thermal decomposition of polymer at air, or phase changes within the polymer melt. Nonetheless, geometry likely plays a role in the formation of a precursor film in ways which are not fully understood, and suggest it may be possible to engineer surface structures to preferentially initiate precursor formation. It is important to note that by raising the temperature, surface tension decreases which results in lower equilibrium contact angle. However, in our experiments, we did not observe notable changes in the equilibrium contact angle by increasing the temperature, which is likely a result of contact line pinning due to minute traces of surface contamination.

Figure 3.5(a-b) shows fits to the contact angle and radius for sapphire using viscous dissipation, MKT, and combined spreading models. For fitting the hydrodynamic model, fitting parameters including the parameter *a* and viscosity with values of 10^{-9} m and 1.25×10^{5} Pa.s, respectively providing the best fit to the experimental data (R^2=0.987). For the MKT model, surface friction of 0.81×10^{7} (dimensionless) is the only fitting parameter (R^2=0.973). For the combined model, the fitting values for surface friction (MKT theory) and the parameter *a* and viscosity are 0.25×10^{7}, 10^{-9} m and 0.91×10^{5} Pa.s, respectively

(R^2=0.997). For the case of the combined model, roughly 15% of the flow is attributed to MKT, while the remainder is dominated by viscous flow, suggesting that the spreading measured here is dictated by viscous dissipation, as expected for long chain polymers. These results demonstrate the practicability for using AFM spreading dynamic measurements to study the specific mechanisms of wetting at elevated temperatures.

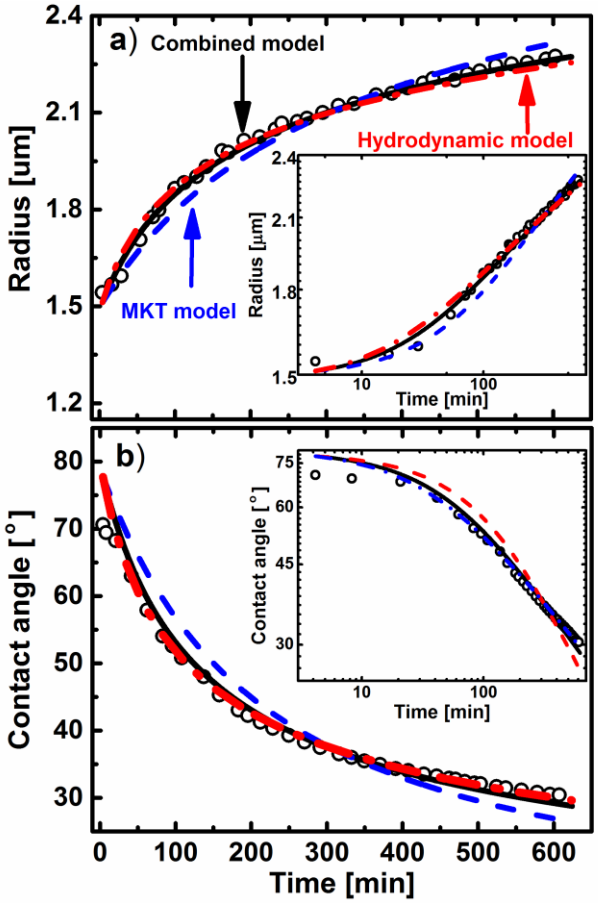

Figure 3.5 Fits to radius (a) and contact angle (b) experimental data for sapphire using combined, MKT and hydrodynamic models. ($\boldsymbol{\zeta}$= 0.25×$\mathbf{10^7}$, a=1e-9 m, $\boldsymbol{\eta}$=0.91×$\mathbf{10^5}$ Pa.s for combined model, $\boldsymbol{\zeta}$=0.81×$\mathbf{10^7}$(dimensionless) for MKT model and a=1e-9 m, $\boldsymbol{\eta}$=1.25×$\mathbf{10^5}$ Pa.s for hydrodynamic model). Insets show the same plots in log-log scale.

The current technique can also track fluid heterogeneity during spreading. In the present experiment, the phase of the AFM cantilever oscillation is sensitive to the mechanical stiffness and dissipation at the tip-substrate interface [57-59]. The stiffness difference between differing phases appears as contrast in AFM phase images. This technique, as an independent and well-established technique, has been utilized for different applications including characterization of biomaterials and energy dissipation studies of different 2D materials [60-63]. Indentation studies of polystyrene at different temperatures show that the modulus of elasticity changes as a function of temperature [64, 65]. Figure 3.6(a-c) shows the overlaid phase and topography AFM images at 145 ºC on mica, sapphire and silicon oxide surfaces, respectively. This shows PS crystalline structures coexist with amorphous phase and the degree of crystallization on sapphire and mica are smaller, less pronounced and less dense as compared to the SiO_2 surface. Figure 3.7(a-f) shows the overlaid phase and topography AFM image of the droplet on SiO_2 substrate from 125 ºC to 175 ºC, where nanoscale chain-like regions appear on the droplet surface.

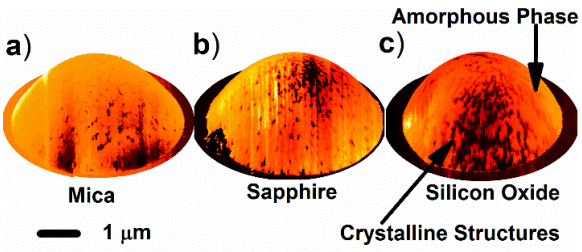

Figure 3.6 (a-c) 3D AFM images of overlaid phase and topography images on mica, sapphire and smooth silicon oxide substrates at 145 ºC.

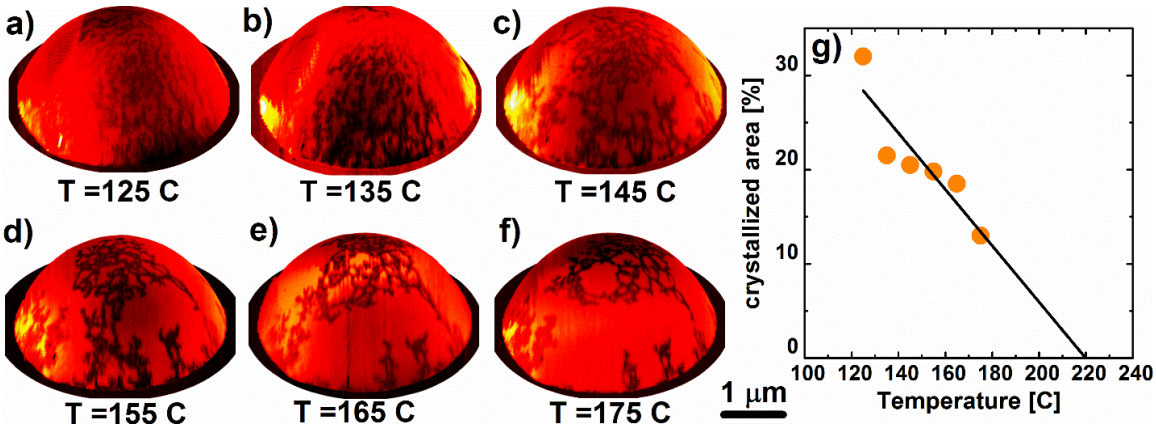

Figure 3.7 (a-f) 3D profile of overlaid phase and topography images of the molten polymer over a temperature range 125-175 °C. (b) Plot of percentage of crystallized area on the molten polymer surface over the temperature range.

Since polystyrene is the only material on the surface, and polystyrene is semi-crystalline [66], it is hypothesized the chains are crystalline regions of polystyrene that nucleated at the substrate and began migrating toward the free surface of the polymer to minimize the free surface energy. Figure 3.7(g) shows the percentage of crystallized area of the droplet surface as the function of temperature, showing a decrease in the amount of crystalline features as temperature increases. Increasing the temperature of the surface toward the melting temperature of polystyrene results in breaking up the prevalence of the chain-like regions. This is consistent with the fact that the melt transition temperature is the temperature below which energy is minimized in the crystalline phase whereas above it serves to minimize the energy in the amorphous phase. Interestingly, such large crystalline regions were not observed on sapphire or mica surfaces, indicating that the

nucleation of crystalline regions within a molten polymer droplet may influence its spreading behavior.

Figure 3.8(a-f) shows the motion of crystalline PS regions over time at 145 ºC on an SiO_2 substrate. Three distinctive crystalline structures have been determined in figure 3.8(a-b) on the droplet surface at the beginning of the measurement. The crystalline structures originally nucleate at the interface of the droplet and the substrate and gradually move toward the top of the droplet. Figure 3.8(g) shows the trajectory of three distinct regions over time. The non-negative average velocity (the average is calculated as the absolute traveled distance by the time elapsed between start and end of the structure) of the regions are approximately 9.87 nm/min, 13.8 nm/min and 13.3 nm/min for yellow, blue and black lines respectively with standard error of 1.2 nm/min. The relation between advection and diffusive heat transfer can be studies using the Peclet number, which is defined as $Pe=LU/\alpha$, where α is thermal diffusivity of the polymer, L is the characteristic length, and U is the mean velocity (which is the measured velocity of the crystalline structures here). The calculated Peclet number is on the order of 10^{-6} in our measurement and it shows that the heat transfer is happening in diffusive rather than advective regime. This value is in contrast to other studies of surface advection during spreading, where the primary driver is fluid evaporation and the Peclet number is large [67].

That the observed motion is driven by thermal diffusivity implies there must be a temperature gradient driving the flow. The temperature dependence of fluid surface tension results in net surface motion from high temperature to low temperature.

We anticipate a small temperature gradient on the droplet surface due to convective cooling of the hot droplet to the cool atmosphere. The temperature gradient on the droplet can be estimated using the thermocapillary velocity equation[68], $U = \frac{d\sigma \times \Delta T}{dT \times \mu}$, where U is the thermocapillary velocity, $\frac{d\sigma}{dT}$ is the temperature gradient of surface tension approximately 0.083 N/m.K for polystyrene [69, 70] and μ is viscosity of the polystyrene estimated as 0.9×10^5 Pa.s.

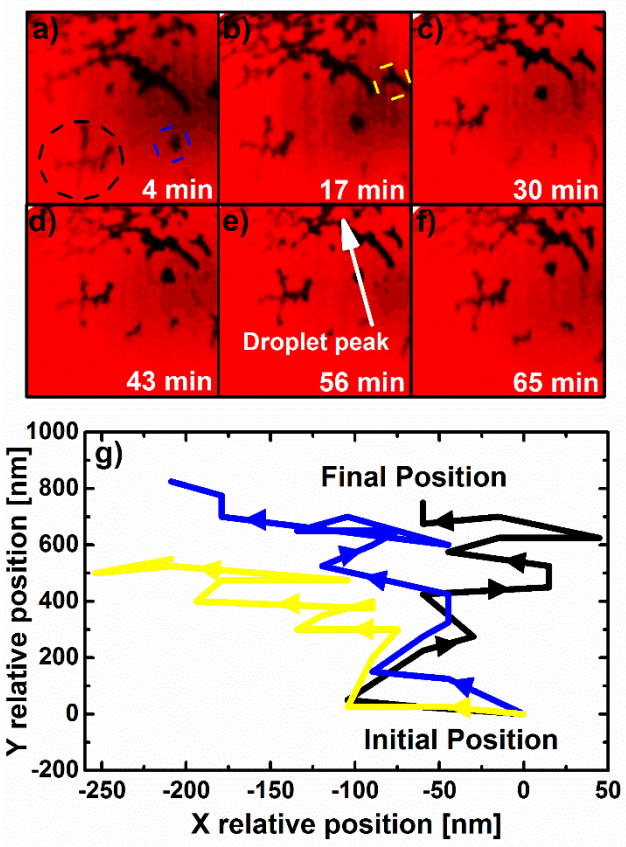

Figure 3.8 (a-f) Movement of the nanoscale chain-like features motion on the molten polymer surface over time. (b) Plot of 2D relative motion of three different features on the polymer surface (identifies by blue, black and yellow circles at figures 7(a) and 7(b)).

We estimate a temperature gradient < 1 °C on the droplet surface sufficient to drive the observed flow, which is consistent with the magnitude of temperature drops expected within this system. It is important to note that the contact line was immobile during these measurements, meaning that internal flow due to dynamic spreading and viscous dissipation are unlikely mechanisms for structure motion. These results demonstrate the ability of AFM tips to track the dynamics of heterogeneous flow with nanometer scale resolution, making it possible to study the dynamics of these materials in ways not possible by any other means. The results of this study reveal the unique spreading dynamics of molten polystyrene droplets, where the droplet initially spreads as a homogeneous fluid according to known spreading laws, eventually transitions to a heterogeneous fluid with an immobile contact line, where surface diffusion of heterogeneous objects is driven by thermocapillary flow.

3.5. Conclusion

We have demonstrated a new technique for dynamic measurement of molten polymer spreading with nanometer scale resolution using AFM. This approach can be used to monitor the spreading dynamics of any nanoscale or microscale polymer structure over a broad range of temperature. Spreading parameters including contact angle, volume, radius and height can be tracked over time. For the case of polystyrene on various solid substrates, we confirm the appropriateness of the spherical cap approximation for the droplet volume, and show that spreading proceeds mainly according to viscous dissipation mechanisms. This method additionally observed nucleation of crystalline structures on the droplet surface at elevated temperature, track the motion of nucleated structures over time,

and observe a decrease in structure prevalence as a function of increasing temperature. The nanometer scale spatial resolution of this technique is 2 orders of magnitude better than existing tools for studying droplet spreading dynamics, making it possible to study wetting phenomena of complex fluid-substrate systems not possible through any other means.

3.6. References

1. Cho, S.H., S.R. White, and P.V. Braun, *Self-Healing Polymer Coatings.* Advanced Materials, 2009. **21**(6): p. 645-649.
2. Toohey, K.S., et al., *Self-Healing Materials with Microvascular Networks.* Nature materials, 2007. **6**(8): p. 581-585.
3. Becker, H. and L.E. Locascio, *Polymer Microfluidic Devices.* Talanta, 2002. **56**(2): p. 267-287.
4. Becker, H. and C. Gärtner, *Polymer Microfabrication Technologies for Microfluidic Systems.* Analytical and bioanalytical chemistry, 2008. **390**(1): p. 89-111.
5. Belfield, K.D. and K.J. Schafer, *A New Photosensitive Polymeric Material for Worm Optical Data Storage Using Multichannel Two-Photon Fluorescence Readout.* Chemistry of Materials, 2002. **14**(9): p. 3656-3662.
6. Hagen, R. and T. Bieringer, *Photoaddressable Polymers for Optical Data Storage.* Advanced Materials, 2001. **13**(23): p. 1805-1810.
7. Vettiger, P., et al., *The" Millipede"-Nanotechnology Entering Data Storage.* Nanotechnology, IEEE Transactions on, 2002. **1**(1): p. 39-55.
8. Gotsmann, B., et al., *Designing Polymers to Enable Nanoscale Thermomechanical Data Storage.* Advanced Functional Materials, 2010. **20**(8): p. 1276-1284.
9. Cannara, R.J., et al., *Thermo-Mechanical Probe Storage at Mbps Single-Probe Data Rates and Tbit in− 2 Densities.* Nanotechnology, 2008. **19**(39): p. 395305.

10. Dürig, U., et al., *"Millipede"–an Afm Data Storage System at the Frontier of Nanotribology.* Tribology Letters, 2000. **9**(1-2): p. 25-32.

11. Acikgoz, C., et al., *Polymers in Conventional and Alternative Lithography for the Fabrication of Nanostructures.* European Polymer Journal, 2011. **47**(11): p. 2033-2052.

12. Guo, X., et al., *A New Strategy of Lithography Based on Phase Separation of Polymer Blends.* Scientific Reports, 2015. **5**.

13. Lipomi, D., et al., *7.11: Soft Lithographic Approaches to Nanofabrication.* Polym. Sci. Compr. Ref, 2012. **10**: p. 211-231.

14. Sirringhaus, H., et al., *High-Resolution Inkjet Printing of All-Polymer Transistor Circuits.* Science, 2000. **290**(5499): p. 2123-2126.

15. Zhao, J., et al., *Efficient Organic Solar Cells Processed from Hydrocarbon Solvents.* Nature Energy, 2016. **1**: p. 15027.

16. Shaheen, S.E., D.S. Ginley, and G.E. Jabbour, *Organic-Based Photovoltaics: Toward Low-Cost Power Generation.* MRS Bulletin, 2005. **30**(01): p. 10-19.

17. Paul, D. and L. Robeson, *Polymer Nanotechnology: Nanocomposites.* Polymer, 2008. **49**(15): p. 3187-3204.

18. Young, T., *An Essay on the Cohesion of Fluids.* Philosophical Transactions of the Royal Society of London, 1805. **95**: p. 65-87.

19. Nieminen, J. and T. Ala-Nissila, *Spreading Dynamics of Polymer Microdroplets: A Molecular-Dynamics Study.* Physical Review E, 1994. **49**(5): p. 4228.

20. Heine, D.R., G.S. Grest, and E.B. Webb III, *Spreading Dynamics of Polymer Nanodroplets.* Physical Review E, 2003. **68**(6): p. 061603.

21. Heine, D.R., G.S. Grest, and E.B. Webb III, *Spreading Dynamics of Polymer Nanodroplets in Cylindrical Geometries.* Physical Review E, 2004. **70**(1): p. 011606.

22. Kwok, D., et al., *Measuring and Interpreting Contact Angles: A Complex Issue.* Colloids and Surfaces A: Physicochemical and Engineering Aspects, 1998. **142**(2): p. 219-235.

23. Neumann, A. and R. Good, *Techniques of Measuring Contact Angles*, in *Surface and Colloid Science*. 1979, Springer. p. 31-91.

24. Kalantarian, A., R. David, and A. Neumann, *Methodology for High Accuracy Contact Angle Measurement†.* Langmuir, 2009. **25**(24): p. 14146-14154.

25. del Rıo, O., et al., *Contact Angle Measurements by Axisymmetric Drop Shape Analysis and an Automated Polynomial Fit Program.* Colloids and Surfaces A: Physicochemical and Engineering Aspects, 1998. **143**(2): p. 197-210.

26. Bonn, D., et al., *Wetting and Spreading.* Reviews of Modern Physics, 2009. **81**(2): p. 739.

27. Leger, L., et al., *Precursor Film Profiles of Spreading Liquid Drops.* Physical Review Letters, 1988. **60**(23): p. 2390.

28. Ausserré, D., A. Picard, and L. Léger, *Existence and Role of the Precursor Film in the Spreading of Polymer Liquids.* Physical Review Letters, 1986. **57**(21): p. 2671.

29. Heiniö, J., K. Kaski, and D. Abraham, *Dynamics of a Microscopic Droplet on a Solid Surface: Theory and Simulation.* Physical Review B, 1992. **45**(8): p. 4409.

30. De Gennes, P.-G., *Wetting: Statics and Dynamics.* Reviews of Modern Physics, 1985. **57**(3): p. 827.

31. de Gennes, P. and A. Cazabat, *Spreading of a Stratified, Incompressible, Droplet*, in *Capillarity Today*. 1991, Springer. p. 33-39.

32. Extrand, C. and S.I. Moon, *Contact Angles of Liquid Drops on Super Hydrophobic Surfaces: Understanding the Role of Flattening of Drops by Gravity.* Langmuir, 2010. **26**(22): p. 17090-17099.

33. Kanungo, M., et al., *Effect of Roughness Geometry on Wetting and Dewetting of Rough Pdms Surfaces.* Langmuir, 2014. **30**(25): p. 7358-7368.

34. Glynos, E., B. Frieberg, and P.F. Green, *Wetting of a Multiarm Star-Shaped Molecule.* Physical Review Letters, 2011. **107**(11): p. 118303.

35. Wang, H., et al., *Surface Microfluidic Patterning and Transporting Organic Small Molecules.* Small, 2014. **10**(13): p. 2549-2552.

36. Xu, H., et al., *Molecular Motion in a Spreading Precursor Film.* Physical Review Letters, 2004. **93**(20): p. 206103.

37. Felts, J.R., et al., *Direct Mechanochemical Cleavage of Functional Groups from Graphene.* Nature Communications, 2015. **6**.

38. Felts, J.R., et al., *Nanometer-Scale Flow of Molten Polyethylene from a Heated Atomic Force Microscope Tip.* Nanotechnology, 2012. **23**(21): p. 215301.

39. Dimitrova, T.D., et al., *Disjoining Pressure Vs Thickness Isotherms of Thin Emulsion Films Stabilized by Proteins.* Langmuir, 2001. **17**(26): p. 8069-8077.

40. Mate, C.M. and V. Novotny, *Molecular Conformation and Disjoining Pressure of Polymeric Liquid Films.* The Journal of Chemical Physics, 1991. **94**(12): p. 8420-8427.

41. De Ruijter, M.J., J. De Coninck, and G. Oshanin, *Droplet Spreading: Partial Wetting Regime Revisited.* Langmuir, 1999. **15**(6): p. 2209-2216.

42. Cox, R., *The Dynamics of the Spreading of Liquids on a Solid Surface. Part 1. Viscous Flow.* Journal of Fluid Mechanics, 1986. **168**: p. 169-194.

43. Voinov, O., *Hydrodynamics of Wetting.* Fluid Dynamics, 1976. **11**(5): p. 714-721.

44. Glasstone, S., K.J. Laidler, and H. Eyring, *The Theory of Rate Processes: The Kinetics of Chemical Reactions, Viscosity, Diffusion and Electrochemical Phenomena*. 1941: McGraw-Hill Book Company, Incorporated.

45. Hayes, R.A. and J. Ralston, *The Molecular-Kinetic Theory of Wetting.* Langmuir, 1994. **10**(1): p. 340-342.

46. Petrov, P. and I. Petrov, *A Combined Molecular-Hydrodynamic Approach to Wetting Kinetics.* Langmuir, 1992. **8**(7): p. 1762-1767.

47. Blake, T. and J. Haynes, *Kinetics of Liquidliquid Displacement.* Journal of Colloid and Interface Science, 1969. **30**(3): p. 421-423.

48. Tanner, L., *The Spreading of Silicone Oil Drops on Horizontal Surfaces.* Journal of Physics D: Applied Physics, 1979. **12**(9): p. 1473.

49. Binnig, G., C.F. Quate, and C. Gerber, *Atomic Force Microscope.* Physical Review Letters, 1986. **56**(9): p. 930.

50. Li, F., C. Geng, and Q. Yan, *Growth Kinetics of Monodisperse Polystyrene Microspheres Prepared by Dispersion Polymerization.* Journal of Polymers, 2013. **2013**.

51. Liu, Y.-X. and E.-Q. Chen, *Polymer Crystallization of Ultrathin Films on Solid Substrates.* Coordination Chemistry Reviews, 2010. **254**(9): p. 1011-1037.

52. James, P., et al., *Interpretation of Contrast in Tapping Mode Afm and Shear Force Microscopy. A Study of Nafion.* Langmuir, 2001. **17**(2): p. 349-360.

53. Hobbs, J.K., O.E. Farrance, and L. Kailas, *How Atomic Force Microscopy Has Contributed to Our Understanding of Polymer Crystallization.* Polymer, 2009. **50**(18): p. 4281-4292.

54. Lau, W.W. and C.M. Burns, *Kinetics of Spreading. Polystyrene Melts on Plane Glass Surfaces.* Journal of Colloid and Interface Science, 1973. **45**(2): p. 295-302.

55. Reiter, G., *Unstable Thin Polymer Films: Rupture and Dewetting Processes.* Langmuir, 1993. **9**(5): p. 1344-1351.

56. Zhang, M., et al., *Wetting Transition in Cylindrical Alumina Nanopores with Polymer Melts.* Nano Letters, 2006. **6**(5): p. 1075-1079.

57. McLean, R.S. and B.B. Sauer, *Tapping-Mode Afm Studies Using Phase Detection for Resolution of Nanophases in Segmented Polyurethanes and Other Block Copolymers.* Macromolecules, 1997. **30**(26): p. 8314-8317.

58. Felts, J.R., et al., *Nanometer Scale Alignment of Block-Copolymer Domains by Means of a Scanning Probe Tip.* Advanced Materials, 2014. **26**(19): p. 2999-3002.

59. Magonov, S., V. Elings, and M.-H. Whangbo, *Phase Imaging and Stiffness in Tapping-Mode Atomic Force Microscopy.* Surface Science, 1997. **375**(2-3): p. L385-L391.

60. Ye, Z. and X. Zhao, *Phase Imaging Atomic Force Microscopy in the Characterization of Biomaterials.* Journal of Microscopy, 2010. **238**(1): p. 27-35.

61. Liu, H., et al., *Visualization of Enzymatic Hydrolysis of Cellulose Using Afm Phase Imaging.* Enzyme and Microbial Technology, 2009. **45**(4): p. 274-281.

62. Holland, N.B. and R.E. Marchant, *Individual Plasma Proteins Detected on Rough Biomaterials by Phase Imaging Afm.* Journal of Biomedical Materials Research Part A, 2000. **51**(3): p. 307-315.

63. Vasić, B., A. Matković, and R. Gajić, *Phase Imaging and Nanoscale Energy Dissipation of Supported Graphene Using Amplitude Modulation Atomic Force Microscopy.* Nanotechnology, 2017. **28**(46): p. 465708.

64. Spinks, G., H. Brown, and Z. Liu, *Indentation Testing of Polystyrene through the Glass Transition.* Polymer Testing, 2006. **25**(7): p. 868-872.

65. Berthoud, P., C. G'sell, and J. Hiver, *Elastic-Plastic Indentation Creep of Glassy Poly (Methyl Methacrylate) and Polystyrene: Characterization Using Uniaxial Compression and Indentation Tests.* Journal of Physics D: Applied Physics, 1999. **32**(22): p. 2923.

66. Ishihara, N., et al., *Crystalline Syndiotactic Polystyrene.* Macromolecules, 1986. **19**(9): p. 2464-2465.

67. Chandramohan, A., et al., *Marangoni Convection in Evaporating Organic Liquid Droplets on a Nonwetting Substrate.* Langmuir, 2016. **32**(19): p. 4729-4735.

68. Hadland, P., et al., *Thermocapillary Migration of Bubbles and Drops at Moderate to Large Marangoni Number and Moderate Reynolds Number in Reduced Gravity.* Experiments in Fluids, 1999. **26**(3): p. 240-248.

69. Yang, D., et al., *Experimental Study on the Surface Characteristics of Polymer Melts.* Colloids and Surfaces A: Physicochemical and Engineering Aspects, 2010. **367**(1): p. 174-180.

70. Park, H., et al., *Effect of Temperature and Pressure on Surface Tension of Polystyrene in Supercritical Carbon Dioxide.* The Journal of Physical Chemistry B, 2007. **111**(15): p. 3859-3868.

4. NANOFABRICATION AND CHARACTERIZATION[3]

4.1. Introduction

AFM cantilevers with integrated heaters were introduced for the first time by IBM at 1999 for thermomechanical data storage application, where a heated AFM tip melts nanoscale indentation data bits into a polymer layer [1]. In addition, heated AFM cantilevers can be used for modulating chemical, optical or electrical properties of a wide range of different materials such as biological, organic or 2D materials [2-4]. Heated AFM cantilevers can also perform nanoscale thermal, mechanical and electrical analyses by setting the temperature between the tip-substrate interface and measuring the material response with the AFM cantilever [5-7]. Depending on specific process requirements, different types of heated AFM probes have been developed. For reducing tip wear, which is a limiting factor for AFM-based imaging, wear resistant ultrananocrystalline (UNCD) diamond tips were integrated onto heated cantilevers [8, 9]. For application of heated AFM cantilever in electrical measurement, it is necessary to decouple the tip voltage and the cantilever temperature by either integrating n-p-n back-to-back diode into the cantilever design [10] or incorporating a Shottky diode at the end of the cantilever [11].

Additive nanomanufacturing is another application of heated AFM cantilevers, otherwise known as thermal dip-pen nanolithography (t-DPN), where a heated tip probe

[3] *Part of the data reported in this chapter is reprinted from Soleymaniha, M. and Felts, J.R., 2019, March. Next generation of heated atomic force microscope cantilever for nanolithography: modelling, simulation and nanofabrication. In Novel Patterning Technologies for Semiconductors, MEMS/NEMS, and MOEMS 2019 (Vol. 10958, p. 109580Q). International Society for Optics and Photonics

can deposit different types of nanostructures with polymer composites [12], and conductive polymers [13-15]. One of the issues contributed with t-DPN is the lack of control over the polymer flow from the tip to the substrate which limits the application of the t-DPN in nanopatterning with high precision and accuracy. Another limiting factor is the limited ability of the technique in pattening wide area which prohibits application of t-DPN for wafer scale and high volume nanofabrication applications. Here we present fabrication process and characterization of new cantilever design for t-DPN with two embedded heaters which are connected with a microchannel. Despite the older generation of t-DPN cantilevers, the new design can control the flow of the polymer precisely with thermocapillary force which is acting on the flow of the polymer in the microchannel. In addition, the second heater, the reservoir, can hold a large amount of polymer, up to 40 ng which helps the cantilever to pattern polymers on a wider area as compared to the other t-DPN cantilevers.

4.2. Nanofabrication Process

Fabrication process of the heated AFM cantilevers consists of six major steps; 1) fabrication of tip, anchor and guards, 2) fabrication of channels, 3) fabrication of cantilevers legs 4) ion implantation, 5) formation of electrical contacts, and 6) releasing the cantilevers. Figure 4.1 shows the fabrication process of the designed cantilevers. The process utilizes n-type <100> Silicon-on-insulator (SOI) wafers with 9 μm silicon device layer and 1μm buried oxide layer, a resistivity of 1-10 Ω-cm and a doping concentration of 1e14 Ω/cm^3. In the following, we describe each major fabrication step in details.

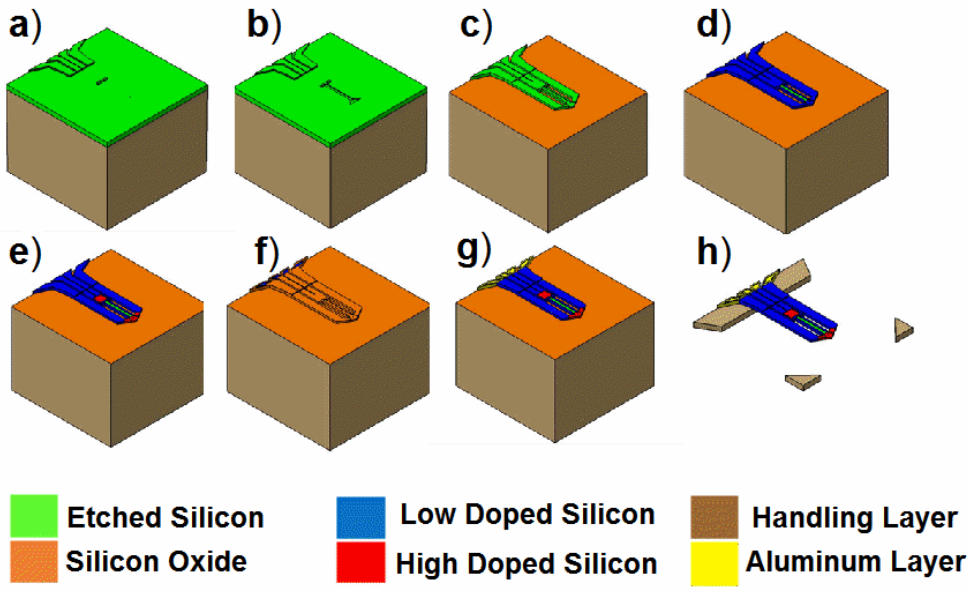

Figure 4.1(a-h) Schematic of nanofabrication process flow of the heated AFM cantilever.

A thin layer of silicon dioxide (600 nm) is deposited with plasma enhanced chemical vapor deposition (PECVD) on the wafer. The deposited oxide layer is used as the etching mask. The first photolithography (contact lithography with i-line) step is to pattern the cantilever base, guards and the tip pillar, followed by inductively coupled plasma Reactive Ion Etching (ICP-RIE) step to etch the resist pattern into the silicon dioxide layer. Then, cryogenic ICP-RIE is used to transfer the silicon dioxide patterns into the silicon layer. As the result, a silicon pillar with 4 μm height and diameter and with an oxide cap on top of it, is fabricated (figure 4.1(a)). Figures 4.2(a-d) show scanning electron microscope (SEM) images of the guards and base structures after the dry etching step of the silicon and removal of photoresist. Figure 4.2(e) shows the zoomed out structures of a guard and pillar and figure 4.2(f) shows the zoomed-in view of the silicon pillar. Table 4.1

shows the etch recipe in ICP-RIE to etch the silicon dioxide and silicon using the photoresist and silicon dioxide as the mask, respectively.

Table 4.1 Etch parameter for silicon dioxide and silicon etch with ICP-RIE tool.

Parameters for etching silicon dioxide		Parameters for etching silicon	
Ar: 10 sccm	Pressure: 10 mTorr	O2: 30 sccm	Pressure: 15 mTorr
CHF3: 25 sccm	Temperature: 25 C	SF6: 90 sccm	Temperature: -100 C
ICP power: 200 W	RF power: 100 W	ICP power: 900 W	RF power: 10 W

Silicon isotropic wet etch with HNA, a mixture of hydrofluoric acid (HF), nitric acid (HNO_3) and water, provides an isotropic silicon etch. As we need to maintain the silicon dioxide cap for the following step, it is necessary to optimize the HNA concentration to get high silicon etching rate and high selectivity with respect to the oxide layer. Therefore, 2% HF, 3% water and 95% HNO_3 mixture is used for etching 1.5 µm of silicon layer. Figure 4.3(a) shows the pillar after the HNA etching step. Ideally, we need to etch 1.5 µm of silicon on each side of the pillar. In the next step, channels are patterned by the second photolithography step. The goal at this step is to finalize the tip structure and transfer the channel structure into the silicon layer. Therefore, cantilever tips are formed by etching the remaining silicon layer of the pillar with the same HNA mixture concentration and removing the silicon dioxide cap by HF (figure 4.1(b) and figure 4.3(b)). Figure 4.4(a-c) show the SEM images of different cantilever designs with long channel (200 µm), short channel (100 µm) and no channel respectively.

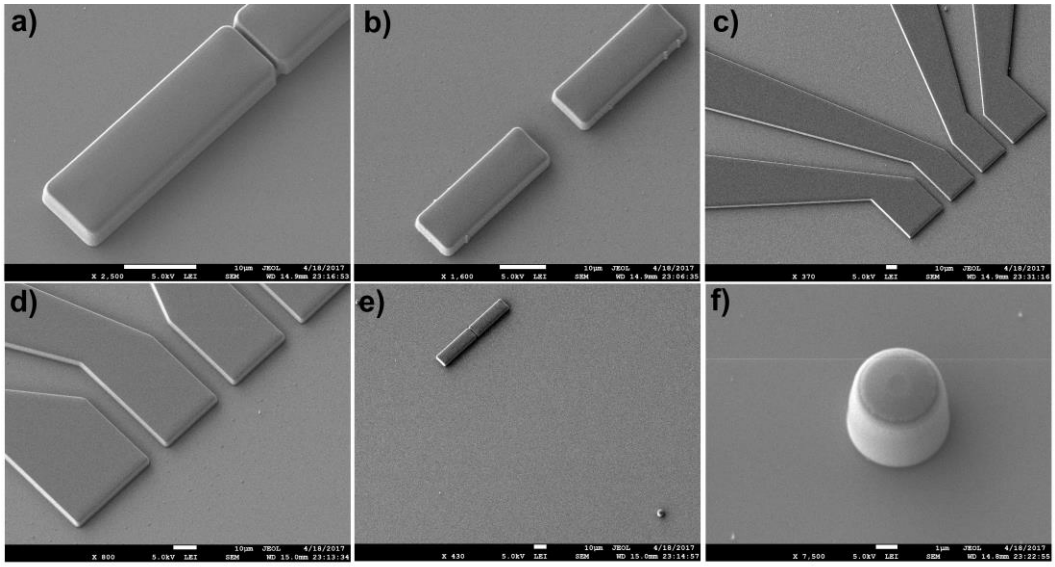

Figure 4.2 SEM images of the SOI wafer after cryogenic ICP-RIE step (a-b) Topography of guard structures. (c-d) Cantilever base e) Zoomed out view of the tip and guard. (f) Pillar with oxide cap.

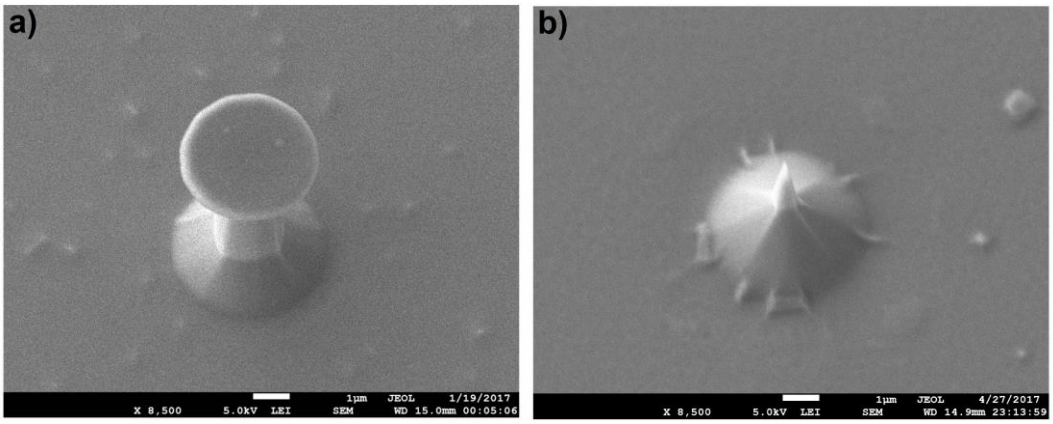

Figure 4.3 SEM images of the pillar (a) after the first HNA isotropic etch with the silicon oxide cap. (b) After the second HNA etch.

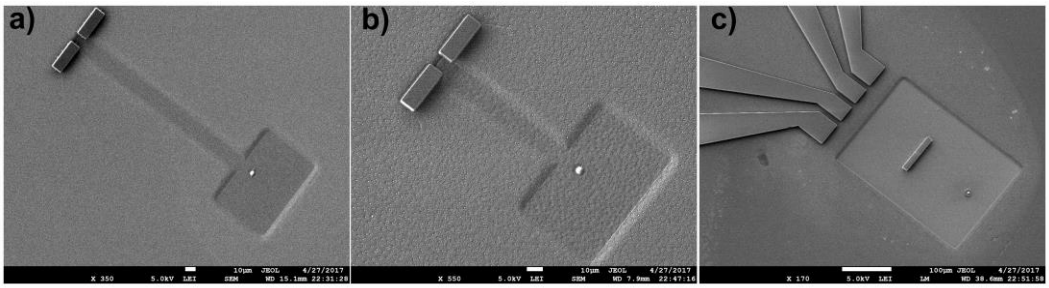

Figure 4.4 SEM images of different cantilever designs including (a) Long channel. (b) Short channel. (c) No channel.

Third, a photolithography (image reversal mode) step is performed to inversely pattern the cantilever legs. Electron beam evaporation is used to deposit 200 nm thin chromium layer on the wafer which is followed by lift-off step to prepare the hard mask for etching the rest of silicon layer with cryogenic ICP-RIE. Cantilever legs are fabricated by etching the rest of the silicon device layer of SOI (figure 4.1(c)). Figures 4.5(a-c) show SEM images of different cantilever designs including short channel (figure 4.5(a)), long channel (figure 4.5(b)) and cantilever with no channel (figure 4.5(c)) after etching the silicon while the chromium layer is still on the wafer.

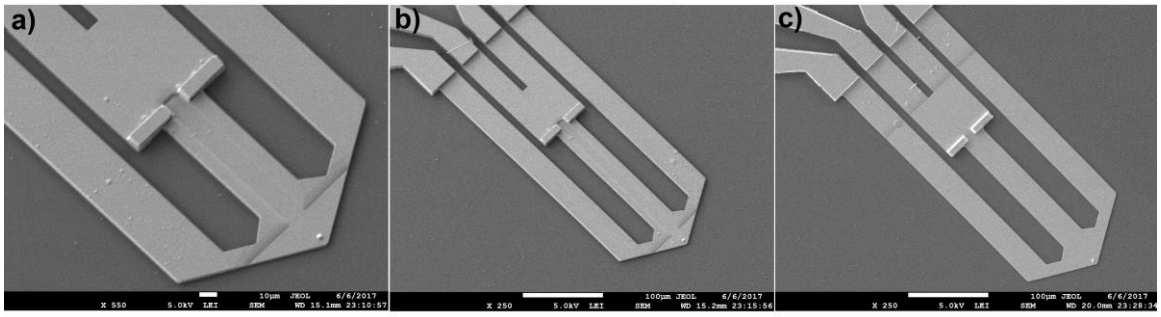

Figure 4.5 SEM images of different cantilever designs after etching the cantilever legs including (a) Short channel. (b) Long channel. (c) No channel**.**

In the next step, the entire cantilever except for the channel is low doped (2.51e13 atoms/cm^2) with phosphorous (figure 4.1(d)). To activate the dopants, it is necessary to diffuse the impurities into the entire cantilever thickness. A thin layer of silicon oxide (100 nm) is deposited with PECVD on the silicon. Diffusion step is performed at 1000 C for 30 min in a horizontal furnace with continuous flow of nitrogen into the tube. The oxide layer is removed prior to the next lithography step. Subsequently, by masking the reservoirs and the channel, the entire cantilever, including legs and base, are high doped (2.51e16 atoms/cm2) with phosphorous (figure 4.1(e)).

Piranha clean and asher were performed to clean the wafers and completely removed the photoresist and other contaminants from the surface. After depositing about 200 nm oxide with PECVD, a diffusion step, like the previous step, is done at the same temperature for 2 hours. The deposited oxide layer in the previous step acts as an insulator layer. In the next step, vias on the highly doped silicon bases are formed by photolithography and transferring the patterns by etching the oxide layer with RIE (figure 4.1(f)). Figures 4.6(a-b) show the cantilevers after etching the silicon oxide to uncover the doped silicon.

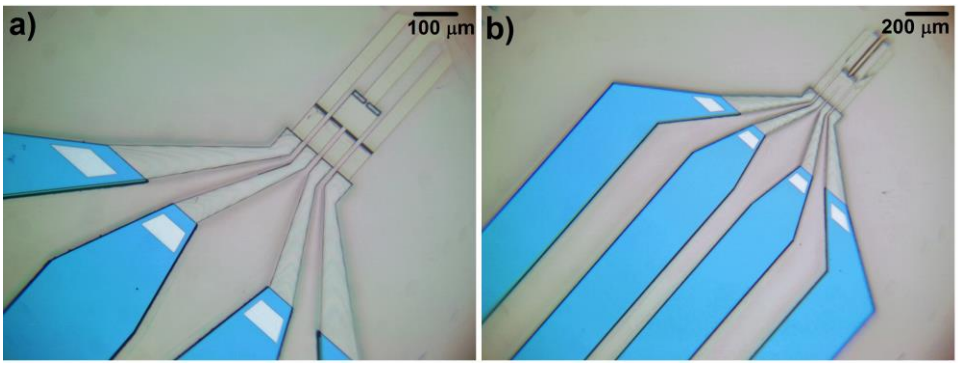

Figure 4.6 Optical images of cantilevers after opening the vias in the silicon oxide layer (a) No channel. (b) Long channel.

The next photolithography step is done to pattern 700 nm thick aluminum traces which are deposited with E-beam evaporation (lift-off) for providing electrical contact between the doped silicon and the aluminum (figure 4.1(g)). For this step, a negative photoresist (NR7-1500P) was used to pattern the cantilevers leads. The deposited aluminum layer provides electrical contact between the patterned silicon vias and the electrical contact pads. Figures 4.7(a-d) show optical images of different cantilever designs after the formation of the aluminum leads (long cantilever without and with channel, short cantilever without and with channel, respectively).

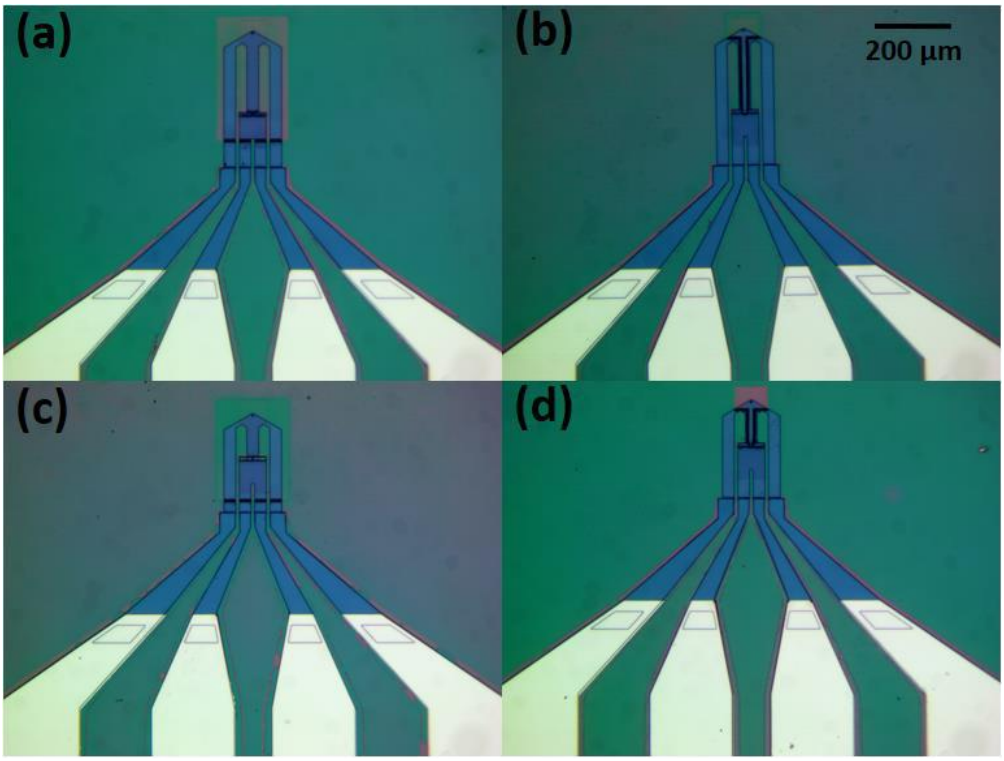

Figure 4.7 Optical images of different cantilever designs (a) Long cantilever without channel. (b) Long cantilever with channel. (c) Short cantilever without channel. (d) Short cantilever with channel.

The last step is to etch the backside of the silicon wafers as a part of the process for releasing cantilevers (figure 4.1(h)). The front side of the wafer is protected by spin coating of a thick layer of photoresist (about 6 µm). The backside lithography is performed to pattern windows on the backside of the wafer which are aligned with the cantilevers on the front side of the wafer. Then, E-beam evaporation of 1 µm aluminum and lift-off process is done to make the backside etch mask. Then, the through silicon etch process is performed with cryogenic ICP-RIE. For this step, a different recipe was used to etch the

silicon with high selectivity with respect to silicon oxide. Table 4.2 shows the details of the recipe. The etch process is stopped when the buried oxide is revealed in the open areas. Then, the wafer was hold in AZ400T stripper at 85 C for around 24 hours and a short ashing step was performed to completely remove the possible remaining photoresist on the wafer. Finally, the buried oxide silicon dioxide layer is removed by HF and the AFM cantilevers is released. Figures 4.8(a-d) show SEM images of Short cantilever without channel, long cantilever without channel and short cantilever with channel, respectively after releasing.

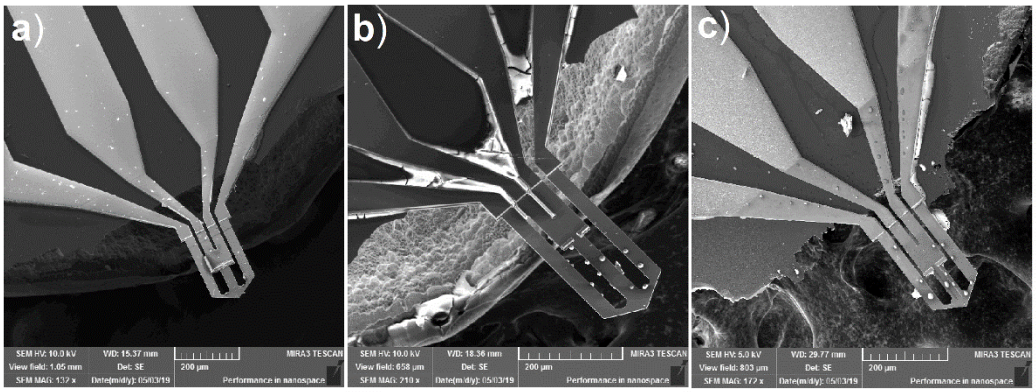

Figure 4.8 SEM images of the fabricated cantilevers after releasing. (a) Short cantilever without channel. (b) Long cantilever without channel. (c) Short cantilever with channel

Table 4.2 Cryogenic ICP-RIE etch recipe for through silicon etch step

Temperature: -110 C	RF power: 3 W
Pressure: 10 mTorr	ICP Power: 700 W
Etch rate: ~2.2 μm/min	SF6/O2: 40/6 Sccm

4.3. Electrical Characterization

It is important to understand the electrical and thermal characterization of the fabricated heated tips before using them in lithography and metrology applications. Therefore, it is required to consider a set of measurements to thermally and electrically calibrate the heated tips.

The electrical resistance of silicon is a function of temperature. By applying voltage through the cantilever aluminum contact leads, the heater temperature increases due to Joule heating. Below the critical temperature threshold, the increase in temperature increases thermal scattering, raising the electrical resistance of the device. At a critical temperature, the thermal energy begins to elevate additional intrinsic charge carriers to the conduction band, lowering the resistance of the cantilever [16, 17]. Since a lower resistance increases current and therefor heating, the cantilever operation becomes unstable at high temperature, resulting in thermal runaway and burnout of the device. Therefore, it is important to evaluate the cantilever resistance change over a range of input voltages to know the electrical properties of the cantilevers at different temperatures. Since the new fabricated heated AFM cantilevers have two heaters, it is required to measure the electrical response of the system for both heaters. For electrical characterization of the heated tip, we consider two identical but independent circuits, one for reservoir and the other for the tip. For each circuit, a Keithley 2400 source-meter which is in series with tip or reservoir heater and sense resistor supplies the circuit with required varying voltage. The sense resistors have 10 KΩ constant resistance value to prevent over heating of the heated cantilevers at high voltages. We used a cantilever with long channel design for

electrical and thermal measurements. The source meters measure the total electrical current of each circuit. By applying Ohm's law, the total resistance value of each circuit is calculated. By subtracting the total resistance value from the sense resistance, the resistance of each heater can be calculated. Electrical measurements are done in two different rounds. In one set, the input voltage for reservoir heater is gradually increased while the input voltage to the tip heater is kept at 1 volt during the measurement. Keeping the voltage at a low constant voltage is done to overcome the noise of measurement and to read the electrical current of the unheated heater. In another set, the same experiment is done by changing the input voltage for tip heater and keeping the voltage at zero for reservoir heater. In each measurement set, the electrical current value for both heaters should be measured to record the change of resistance in both heaters while applying voltage to only one of the heaters.

Figure 4.9 shows both heaters resistance change with increasing voltage at each set of measurements. In both cases, the resistance of the heaters increases with the input voltage and then drops at a critical temperature. Therefore, by increasing the voltage, more current can flow in the silicon which reduces the resistance even further. The initial resistance for the tested cantilever for the reservoir and the tip are 0.9 kΩ and 1.8 kΩ, respectively.

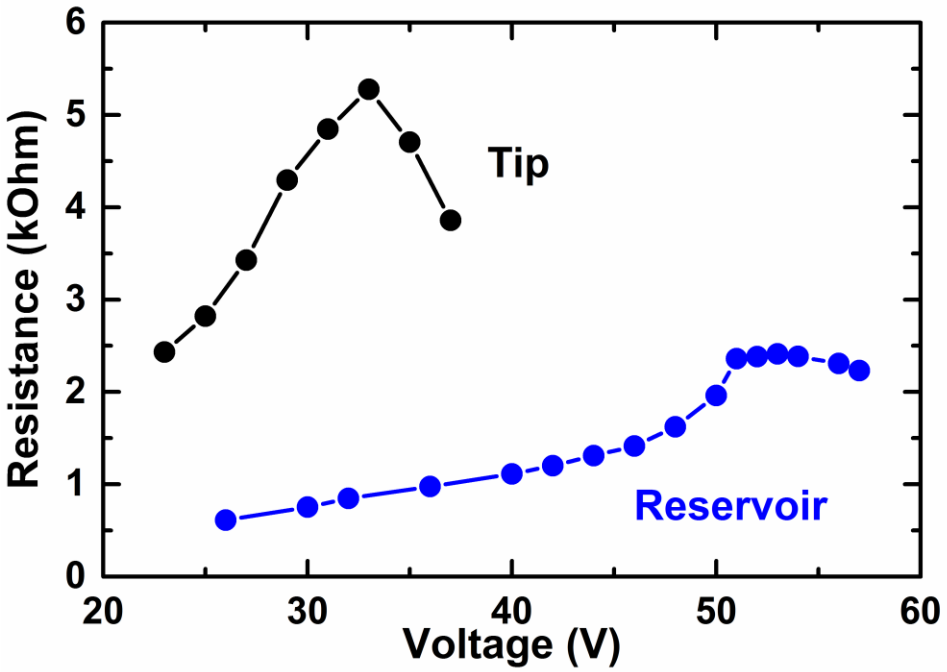

Figure 4.9 Resistance change of heaters with respect to the input voltage.

4.4. Thermal Characterization

Raman thermometry is a spectroscopy-based technique in which a laser beam is focused on a surface and collects a portion of the scattered photons, specifically inelastic scattering component, from the surface. The inelastic scattered photons have shifts in their energy level, called Stokes shifts, which depend on vibrational state of the substrate. In heated AFM cantilevers, by applying voltage across cantilever legs, temperature increase in heater regions. The temperature shift in the material due to the crystal lattice vibrations can be related to the Stokes peak position, width and intensity. For thermal analysis of the heated AFM cantilevers, relative changes in the Raman Stokes peaks with respect to room temperature peaks is done to derive the temperature of each heater for a range of input voltages. Raman measurements is done with Jobin-Yvon Horiba Labram HR instrument

coupled to an Olympus BX41 microscope. Two sets of thermal analysis is done for calibration of both heaters. First, the laser is focused on the tip heater at the end of the cantilever and Raman peaks are recorded for a range of applied voltage to the tip heater only. Then, the same process is done for the reservoir heater by focusing the laser on reservoir heater and applying voltage to the reservoir heater only. The temperature at each specific Raman peak can be estimated by the following formula [16, 17]:

$$T_n = \frac{P_n - P_{n-1}}{0.022} + T_{n-1} \qquad \text{(eqn 4.1)}$$

Where T_n and P_n are the temperature and Raman peak at a specific voltage value correspondingly. Whereas T_{n-1} and P_{n-1} are the temperature and Raman peak at a lower voltage value.

Figure 4.10 shows the resistance changes of heaters by changing the temperature at the corresponding heater. In both cases, thermal runaway occurs at around 500 C when the tip and reservoir resistance values drop and start to decrease by further increasing the temperature by applying higher voltage value across the heaters.

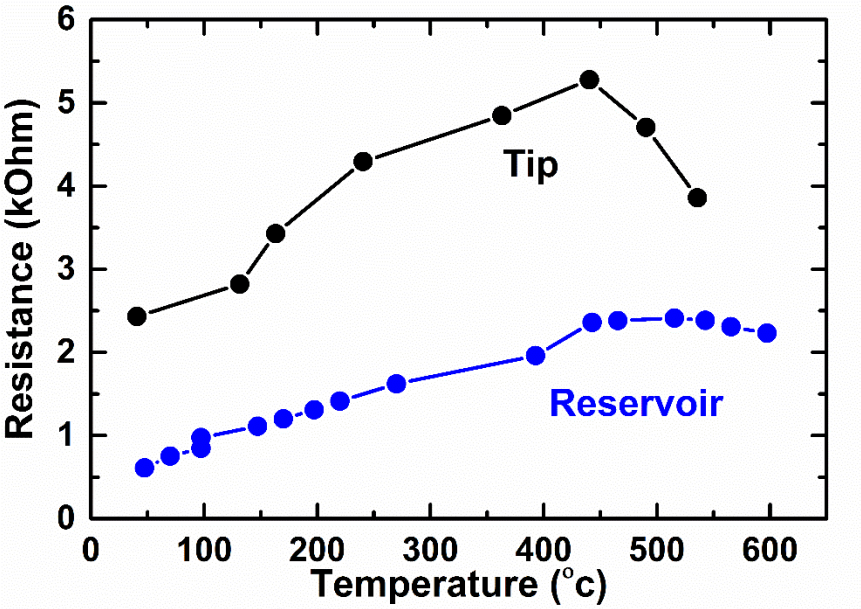

Figure 4.10 Resistance change over temperature during heating individual heaters.

Figure 4.11 shows the change of temperature over voltage change for the both cases. Due to conduction through the channel, by either heating one of the heaters, the other heater temperature raises as well. In the case of heating the tip, the maximum tested temperature at the tip heater is around 600 °C whereas the temperature at unheated reservoir reaches to around 175 °C. In the heated reservoir measurement, the temperature at the unheated tip heater reaches to around 200 °C due to heat conduction through the channel between the heaters whereas the temperature at the heated reservoir heater reaches to 600 °C. In other words, the maximum temperature gradient along the channel is about 2.0E6 °C/m for the tested cantilever which has 200 µm long channel between the heaters.

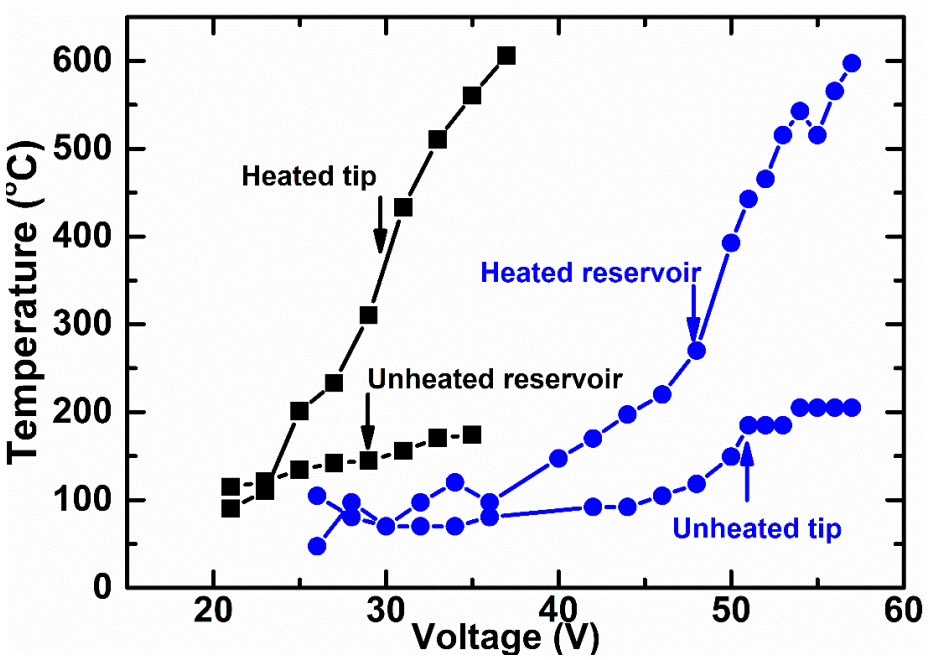

Figure 4.11 Resulting temperature of the tip and reservoir as a function of input voltage applied either to tip heater (black color) or the reservoir heater (blue color).

4.5. Conclusion

We have demonstrated nanofabrication processes required for manufacturing heated AFM cantilevers with two embedded joule heaters. Electrical and thermal properties of the cantilevers were determined in DC mode only. Electrical measurement of a fabricated cantilever shows electrical resistance of 0.9 KΩ and 1.8 KΩ at room temperature in the reservoir and the tip heaters respectively. Preliminary Raman spectroscopy results show maximum temperature of around 500 °C for both heaters before thermal runaway happens. Due to heat transfer between the heaters, heating a single heater results in temperature increasing of the other heater such that a heating reservoir at 600 °C results in an unheated tip with around 200 °C. The heat transfer effect between the heaters had been illustrated by FEM simulations in chapter 2.

4.6. References

1. Vettiger, P., et al., *Ultrahigh Density, High-Data-Rate Nems-Based Afm Data Storage System.* Microelectronic Engineering, 1999. **46**(1-4): p. 11-17.
2. Carroll, K.M., et al., *Fabricating Nanoscale Chemical Gradients with Thermochemical Nanolithography.* Langmuir, 2013. **29**(27): p. 8675-8682.
3. Zheng, X., et al., *Patterning Metal Contacts on Monolayer Mos 2 with Vanishing Schottky Barriers Using Thermal Nanolithography.* Nature Electronics, 2019. **2**(1): p. 17.
4. King, W.P., et al., *Atomic Force Microscope Cantilevers for Combined Thermomechanical Data Writing and Reading.* Applied Physics Letters, 2001. **78**(9): p. 1300-1302.
5. King, W.P., et al., *Heated Atomic Force Microscope Cantilevers and Their Applications.* Annual Review of Heat Transfer, 2013. **16**.
6. King, W.P., et al., *Nanoscale Thermal Analysis of an Energetic Material.* Nano Letters, 2006. **6**(9): p. 2145-2149.
7. Borca-Tasciuc, T., *Scanning Probe Methods for Thermal and Thermoelectric Property Measurements.* Annual Review of Heat Transfer, 2013. **16**(16).
8. Fletcher, P.C., et al., *Wear-Resistant Diamond Nanoprobe Tips with Integrated Silicon Heater for Tip-Based Nanomanufacturing.* ACS Nano, 2010. **4**(6): p. 3338-3344.
9. Kim, H.J., et al., *Ultrananocrystalline Diamond Tip Integrated onto a Heated Atomic Force Microscope Cantilever.* Nanotechnology, 2012. **23**(49): p. 495302.

10. Fletcher, P.C., et al., *Electrothermal Atomic-Force Microscope Cantilever with Integrated Heater and Npn Back-to-Back Diodes.* Journal of Microelectromechanical Systems, 2011. **20**(3): p. 644-653.

11. Maniscalco, N.I. and W.P. King, *Microcantilever with Integrated Solid-State Heater, Conductive Tip, and Schottky Diode.* Sensors and Actuators A: Physical, 2011. **168**(2): p. 351-357.

12. Lee, W.K., et al., *Maskless Nanoscale Writing of Nanoparticle− Polymer Composites and Nanoparticle Assemblies Using Thermal Nanoprobes.* Nano Letters, 2009. **10**(1): p. 129-133.

13. Yang, M., et al., *Direct Writing of a Conducting Polymer with Molecular-Level Control of Physical Dimensions and Orientation.* Journal of the American Chemical Society, 2006. **128**(21): p. 6774-6775.

14. Hu, H., H. Kim, and S. Somnath, *Tip-Based Nanofabrication for Scalable Manufacturing.* Micromachines, 2017. **8**(3): p. 90.

15. Felts, J.R., et al., *Nanometer-Scale Infrared Spectroscopy of Heterogeneous Polymer Nanostructures Fabricated by Tip-Based Nanofabrication.* ACS Nano, 2012. **6**(9): p. 8015-8021.

16. Lee, J., et al., *Electrical, Thermal, and Mechanical Characterization of Silicon Microcantilever Heaters.* Journal of Microelectromechanical Systems, 2006. **15**(6): p. 1644-1655.

17. Nelson, B.A. and W. King, *Temperature Calibration of Heated Silicon Atomic Force Microscope Cantilevers.* Sensors and Actuators A: Physical, 2007. **140**(1): p. 51-59.

5. CONCLUSION AND FUTURE WORKS

This dissertation presented the design, fabrication and characterization of new heated AFM cantilever which potentially can be used for nanomanufacturing polymer-based nanostructures on a variety of substrates. However, it would be necessary to perform more detailed mechanical, electrical and thermal characterizations on different variations of the fabricated cantilevers before using them for t-DPN applications. One of the most important thermal experiments would be a Raman measurement for extracting temperature gradient map along the microchannel for different temperatures of heaters which would give a better understanding regarding the thermo-capillary effect in the heated AFM cantilevers.

Additional Raman measurements are required to derive resonance frequency and spring constant of the cantilevers [1]. In addition, to evaluate the imaging resolution of the cantilevers, a series of measurements would be needed to evaluate the tip radius of curvature in different batches of fabricated cantilevers. Since the fabricated cantilevers have different thicknesses, running mechanical tests for each cantilever would be crucial.

Recently, t-DPN has been performed for fabrication of MoS_2 field-effect transistors with as narrow as 30 nm [2]. With the new heated AFM cantilever design, it would be expected to have control over the polymer flow, making it possible to write even narrower polymer line to shrink down the resolution even further. Another interesting application could be depositing quantum dot inks on the center of bowtie nanoantennae with nanometer scale resolution of t-DPN technique.

The new design has a reservoir to stack polymer, making it possible to continue writing with the cantilever for much longer time as compared to the older designs. Therefore, a higher throughput is expected for the new design. It should be noted that the current trend in feeding the t-DPN cantilever is manually dipping the tip into a polymer sink and touching the tip with the ink. It is a time consuming process which requires nanoscale precision and there is a high risk to either break the cantilever or damage the tip. The new heated cantilever has a large reservoir area for placement of polymer colloids which can facilitate the feeding process. However, for improving the feeding yield and throughput, it would be necessary to consider a micromanipulation robotic setup with to stack the polymer colloids on the reservoir heater.

However, there could more ways to even further increase the throughput such as considering a continuous polymer feeding mechanism instead of current manual dipping process. Previous experiments have shown promising results in terms of integrating multiple cantilevers onto a single chip to increase the throughput of the fabrication process with heated AFM cantilever [3]. A new design for arrays of the new cantilevers would be a new interesting route for further improvement of t-DPN with the new cantilevers.

Moreover, the design of the cantilever can be further optimized to incorporate multiple channels and reservoirs with different polymers for patterning dopant junctions in organic photovoltaics, microfluidics devices and electronic logic circuits. The ability to pattern different materials without removing the cantilever and inking process will add the value of the t-DPN technique for high volume nanomanufacturing of MEMS/NEMS.

An important key for future improvements of t-DPN is understanding the mechanism of spreading of polymers at the nanoscale. In order to control the polymer flow along the microchannel or on the surface, it would be important to find a way to measure and analysis the precursor growth of the polymer. The study of precursor on a surface have been done mainly through molecular dynamics simulations and yet it has not been possible to experimentally study the dynamic behavior of the polymer precursor [4, 5]. With the AFM-based technique the interactions between polymer and substrate could be studied on flat surfaces. However, a comprehensive study is required to study the spreading of more polymer types on a variety of surfaces such as rough or textured surfaces to evaluate the theories of spreading on textured surfaces for polymers at the nanoscale. As there has been considerable debates and controversy on wetting transparency of the graphene [6], it would be helpful to take advantage of high resolution of the AFM to study the graphene wetting behavior with this technique.

Finally, the ability to predict and control the spreading of polymers at the nanoscale will help us to not only develop better toolsets for nanolithography, but also would give the ability to utilize the insight in other fields like green energy, lubrication, environmental science and automotive industry.

5.1. References

1. Lee, J., et al., *Electrical, Thermal, and Mechanical Characterization of Silicon Microcantilever Heaters.* Journal of Microelectromechanical Systems, 2006. **15**(6): p. 1644-1655.
2. Chen, S., et al., *Monolayer Mos2 Nanoribbon Transistors Fabricated by Scanning Probe Lithography.* Nano Letters, 2019.
3. Lee, J. and W.P. King. *Array of Microcantilever Heaters with Integrated Piezoresistors*. in *2007 7th IEEE Conference on Nanotechnology (IEEE NANO)*. 2007. IEEE.
4. Mate, C.M., *Anomalous Diffusion Kinetics of the Precursor Film That Spreads from Polymer Droplets.* Langmuir, 2012. **28**(49): p. 16821-16827.
5. Heine, D.R., G.S. Grest, and E.B. Webb III, *Surface Wetting of Liquid Nanodroplets: Droplet-Size Effects.* Physical Review Letters, 2005. **95**(10): p. 107801.
6. Rafiee, J., et al., *Wetting Transparency of Graphene.* Nature materials, 2012. **11**(3): p. 217.

APPENDIX A

PHOTOLITHOGRAPHY MASKS

Mask1: Tip, guard and base formation

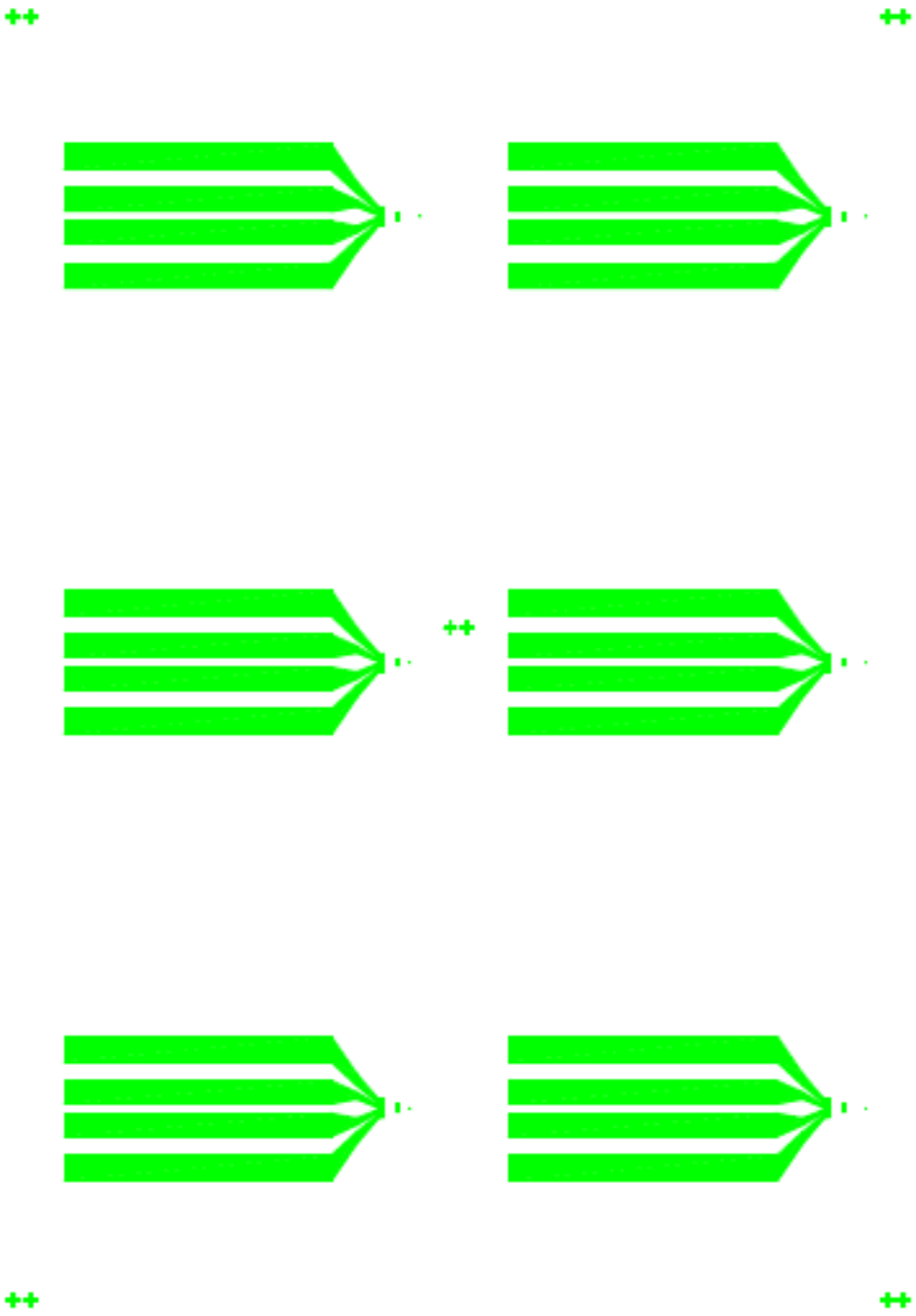

Mask 2: Channels

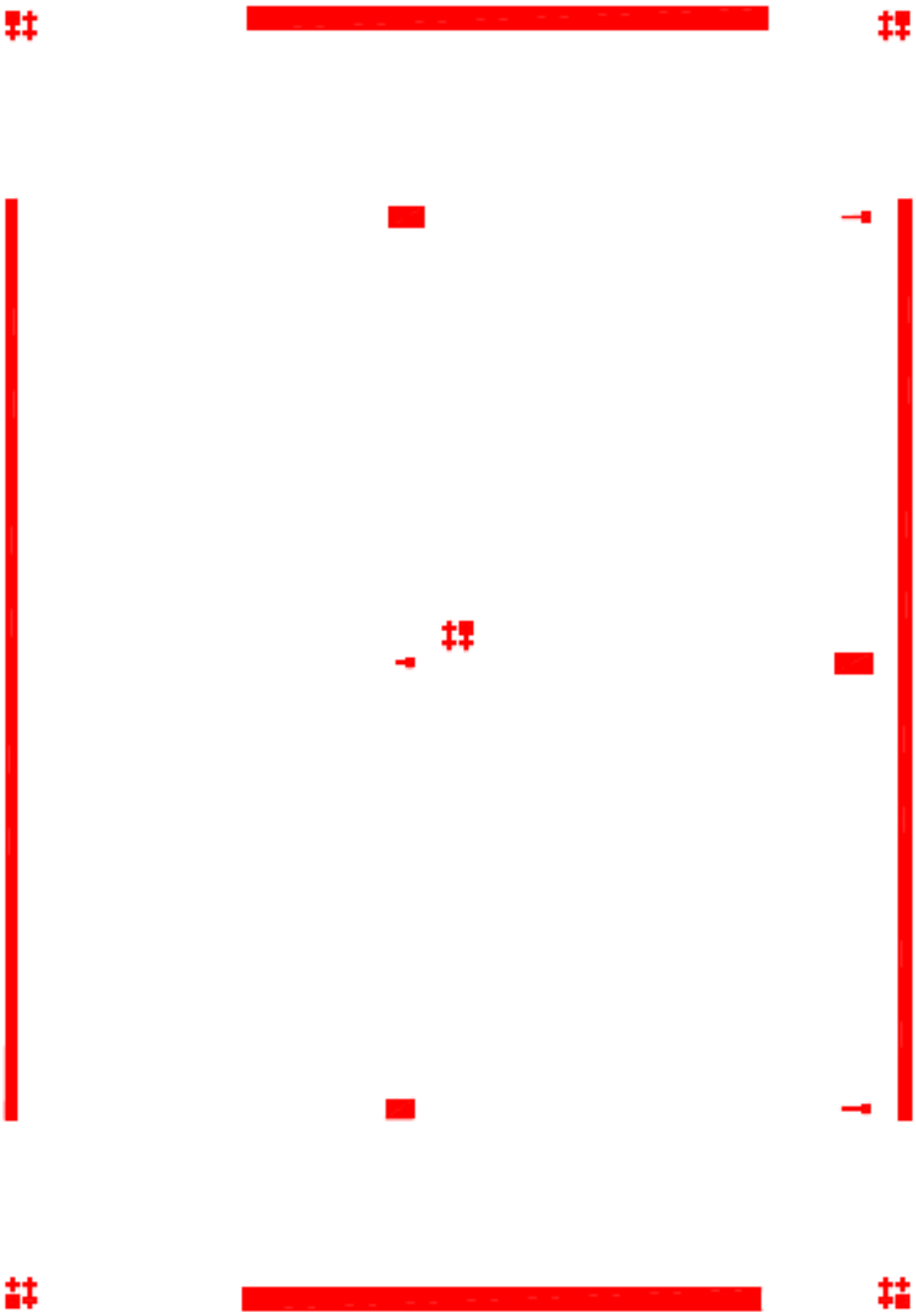

Mask 3: Cantilever legs

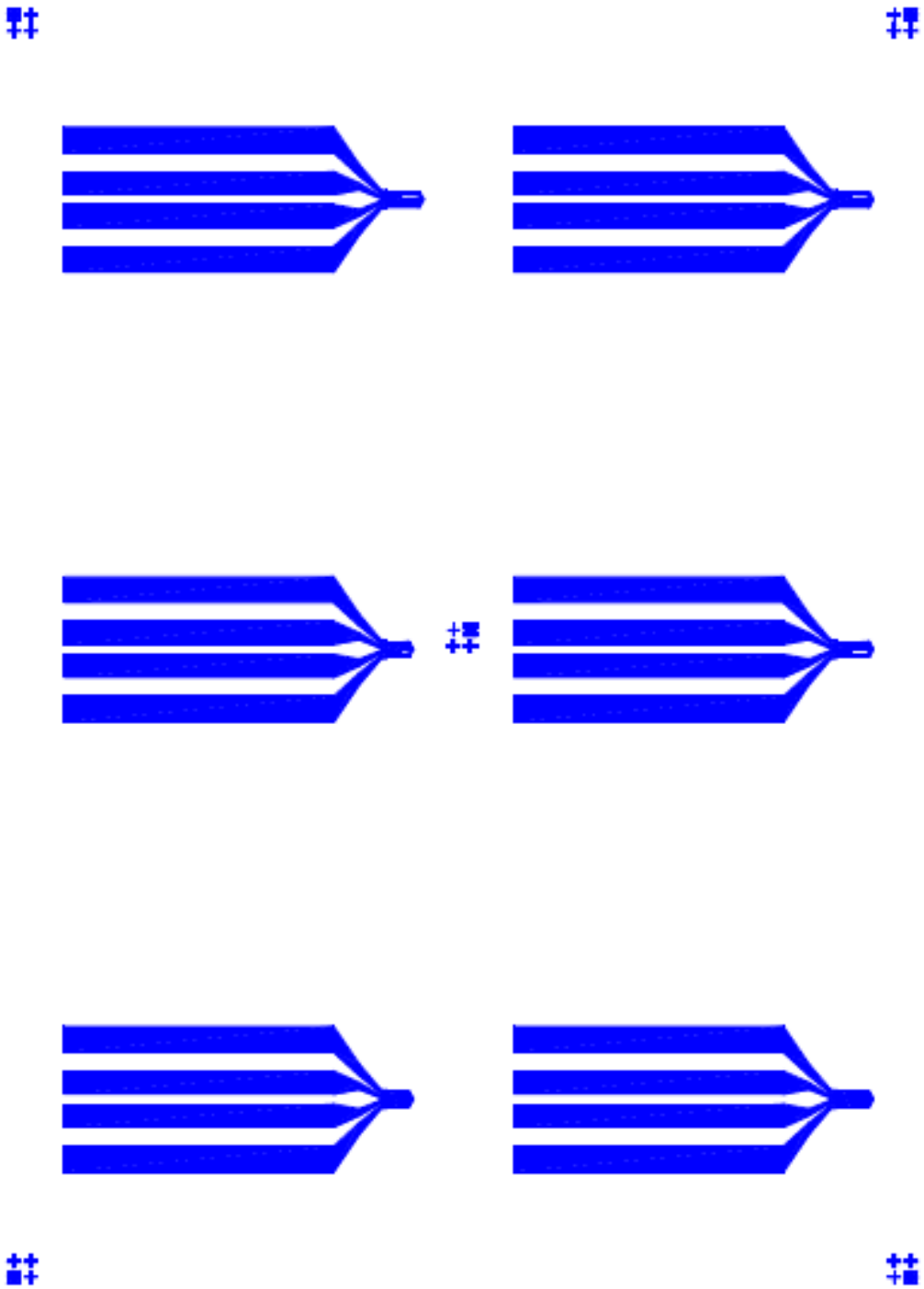

Mask 4: Low dose implantation

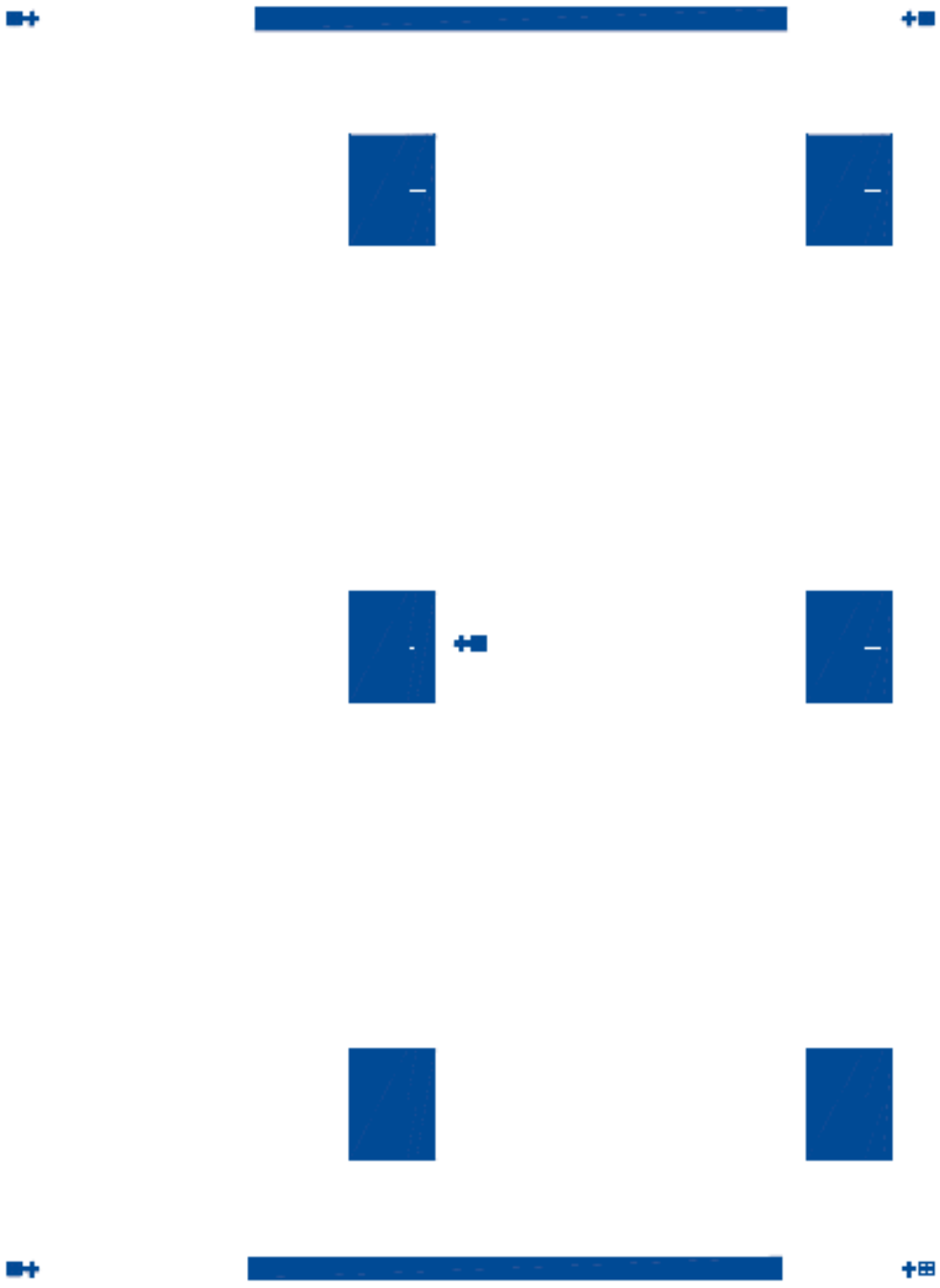

Mask 5: High dose implantation

Mask 6: Contact vias

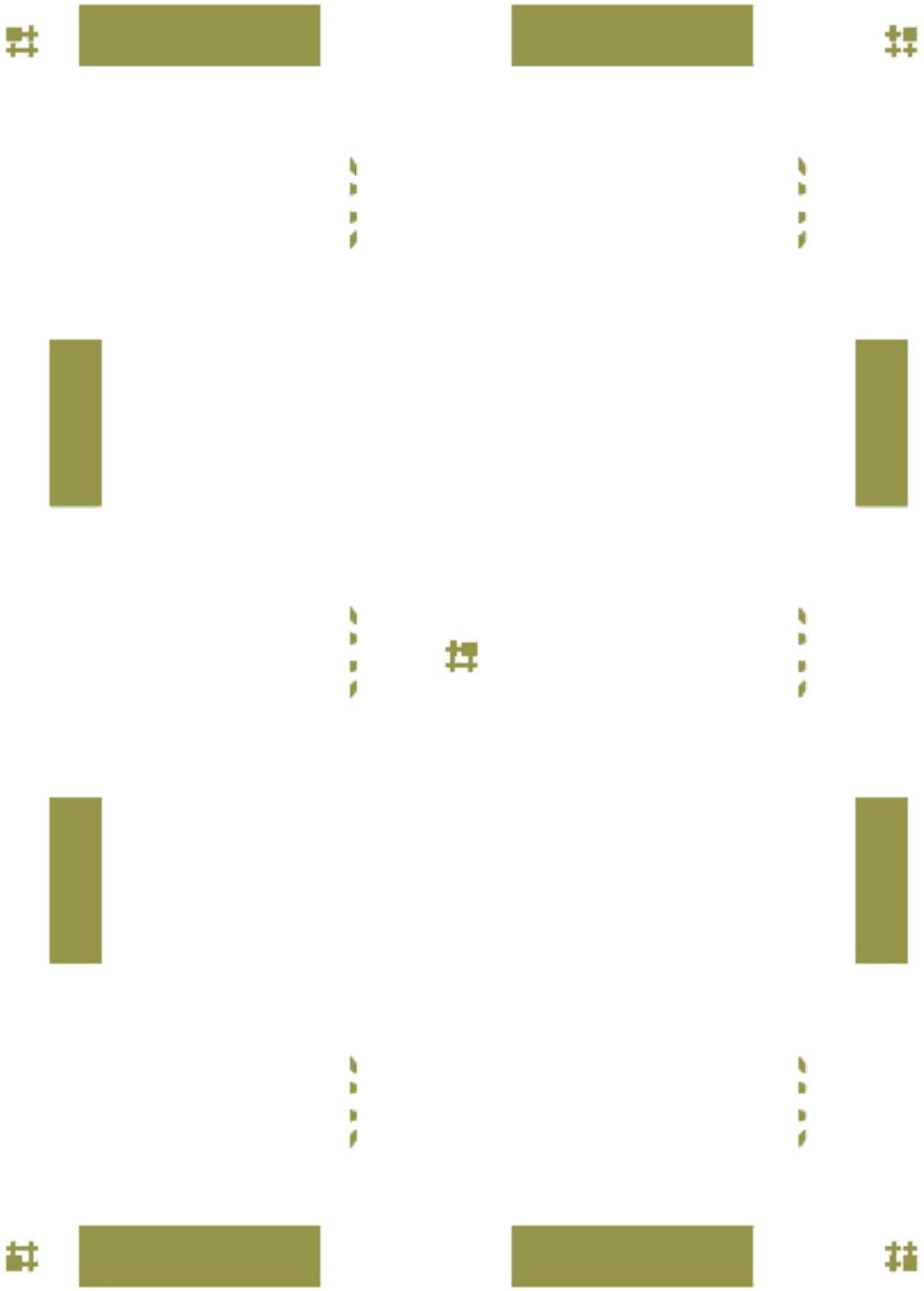

Mask 7: Aluminum leads

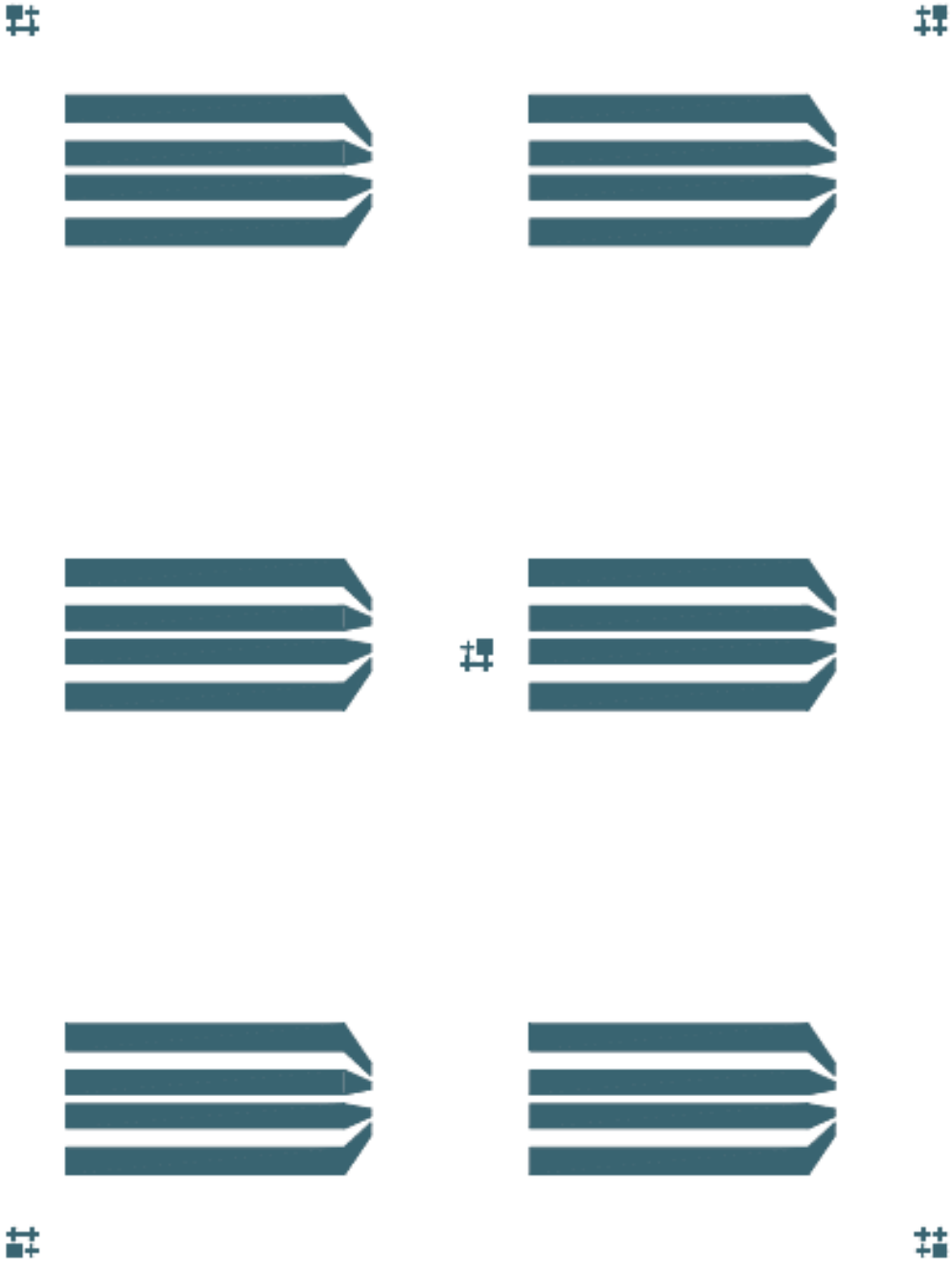

Mask 8: Backside Etch

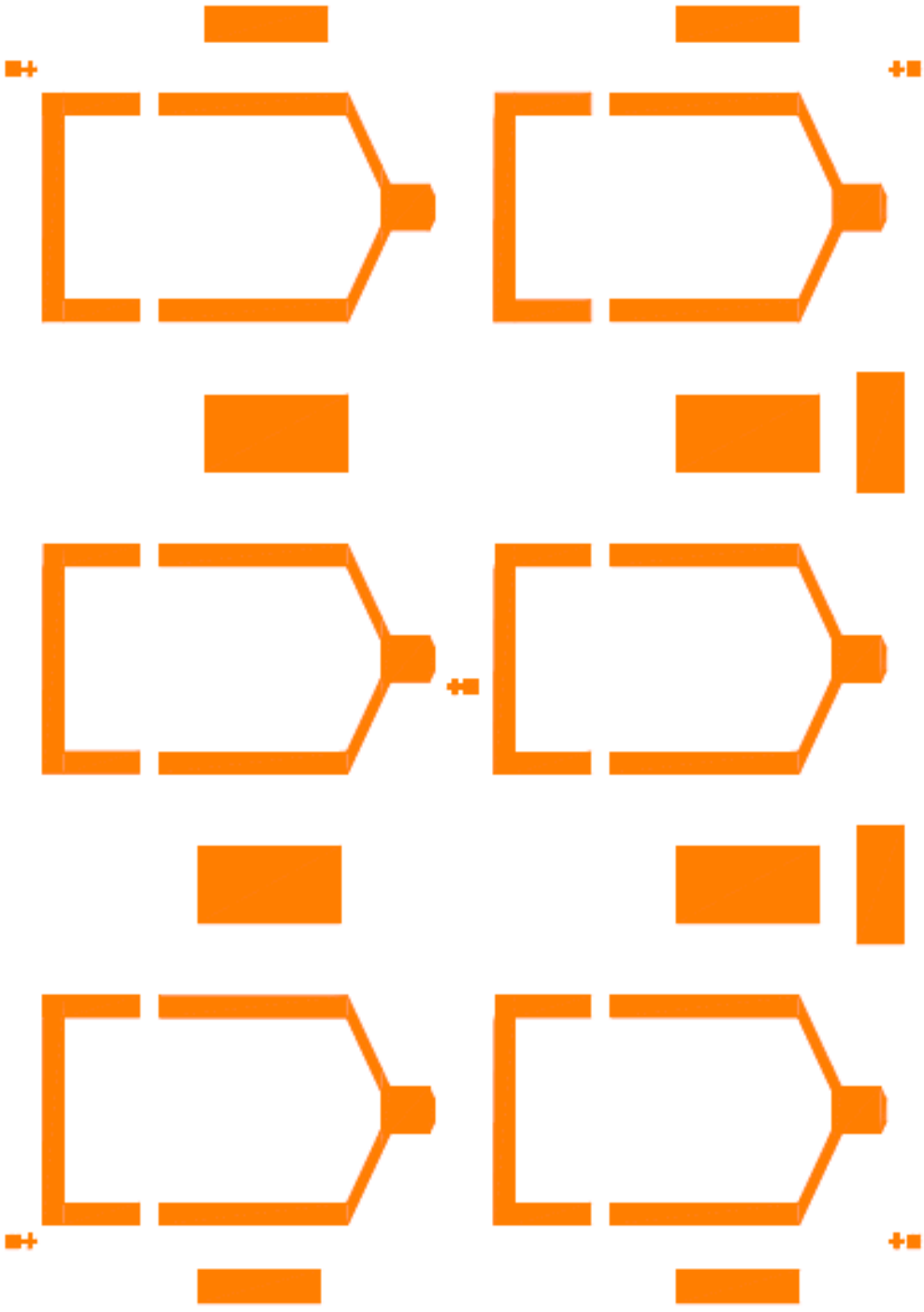

APPENDIX B

NANOFABRICATION RECIPE

Microfabrication recipe			
Wafer material			
1	**Material**	**Material**	SOI wafer <100> (3 inch wafer) 10 µm -1 µm-550 µm, one side polished
Wafer cleaning			
2	**Material**	**Material**	Cleaning with Piranha and HF to remove native oxide
Oxide deposition			
3	Chip, Anchor, guard and tip	**Equipment /Recipe:**	PECVD (oxide deposition) Thickness: 6000-6500 Å
Measure oxide thickness			
4	Chip, Anchor, guard and tip	**Equipment/ Recipe:**	Ocean optics NanoCalc DUV (ellipsometer) Record the oxide thickness
AZ5214E (photoresist coating)			
5	Chip, Anchor, guard and tip	**Equipment/ Recipe:**	BID-TEK SP-100 Spin Coater HMDS coating with the same recipe as the resist. Rotation speed: 4000 rpm/ 40 sec Thickness=∼1.4 µm **Softbake** on hotplate at 120°C for 2 min
Photolithography of Mask #1			
6	Chip, Anchor, guard and tip	**Equipment:** **Recipe:**	Karl Suss MA-6 Mask Aligner (4 inch mask holder) Contact mode: soft contact *Exposure* Ch.2 (wavelength=365 nm) Dose=55-65 mJ **Development:** AZ-726 or AZ 1:1 (check the status of the development every 15 sec)

Hard Bake			
7	Chip, Anchor, guard and tip	**Equipment:** **Recipe:**	Oven 135 °C for 10 min
Topside Oxide Etch			
8	Chip, Anchor, guard and tip	**Equipment:** **Recipe:**	ICP-RIE Etch Depth Needed= 6000-6500 Å Gases used: Ar/CHF3 at 25 C. Etch rate: 50 nm /min
Topside Silicon Etch (Anisotropic)			
9	Chip, Anchor, guard and tip	**Equipment:** **Recipe:**	Cryo ICP-RIE (-100C) Etch Depth Needed= 4 µm Etch rate: ~ 1 µm/min
Topside Silicon Wet Etching (Isotropic)			
10	Chip, Anchor, guard and tip	**Equipment:** **Recipe:**	Wet Bench- HNA Etch Depth Needed=1.7 µm HNA-2% HF, 3% H2O, 95% HNO_3
SEM			
11	Chip, Anchor, guard and tip	**Equipment:** **Recipe:**	SEM Measure the tip structure to avoid over etching in the following steps.
AZ5214E (photoresist coating)			
12	Channel	**Equipment:** **Recipe:**	BID-TEK SP-100 Spin Coater 4000 rpm/40 sec Thickness=~3.2 µm
Photolithography of Mask #2			
13	channel	**Equipment:** **Recipe:**	Karl Suss MA-6 Mask Aligner Contact mode: soft contact *Exposure* Ch.2 (wavelength=365 nm) Dose=100 mJ **Development:** AZ-726 (20 sec intervals)
Hard Bake			
14	Channel	**Equipment:** **Recipe:**	Oven 135 °C for 10 min

Isotropic Silicon etch (anisotropic)			
15	Tip	**Equipment:** **Recipe:**	HNA Etch Depth Needed= 0.5 µm/HNA-2% HF, 3% H2O, 95% HNO_3
SEM			
16	Tip	**Equipment:** **Recipe:**	SEM Measure the tip structures
Image reversal/Lift off (LOR+AZ5214E)			
17	Legs	**Equipment:** **Recipe:**	BID-TEK SP-100 Spin Coater 400 Thickness=~200 nm (LOR 2A) Thickness~ 1.4 µm (AZ5214E)
Softbake/Prebake			
18	Legs	**Equipment:** **Recipe:**	Hot Plate 170 °C for 8 mins (LOR) 120 °C for 90 sec (AZ5214E) Image reversal bake: 90 sec at 120 °C
Photolithography of Mask #3			
19	Legs	**Equipment:** **Recipe:**	Karl Suss MA-6 Mask Aligner Contact mode: soft contact *Exposure* Ch.2 (Wavelength = 365 nm) First exposure= 50 mJ Flood exposure= 250 mJ **Development:** AZ726 Check the wafer every 15 sec with optical microscope
E-beam Evaporation			
20	Legs	**Equipment:** **Recipe:**	Lesker E-beam evaporation Deposition rate: 1 angstrom/sec Chromium deposition thickness: 100 nm
Liftoff			
21	Legs	**Equipment:** **Recipe:**	AZ400T Stripper at 80 °C Time: about 10 min Acetone sonication if needed.

Topside Silicon Etch (Anisotropic)			
22	Legs	**Equipment:** **Recipe:**	ICP-RIE Cryo Etch (-90 °C) with SF6/O2 Etch Depth Needed = The remaining device layer thickness
Cr removal			
23	Legs	**Equipment:** **Recipe:**	Cr etchant Time= about 10-15 min Tip: Sonication in acetone can be used for lift off.
Piranha clean			
24	Legs	**Equipment:** **Recipe:**	Wet bench H2SO4/H2O2 (3:1) for 10 min followed by acetone sonication
AZ5214E (photoresist coating)			
25	Implantation	**Equipment:** **Recipe:**	BID-TEK SP-100 Spin Coater 2000 rpm for 40 sec Thickness = ~2.5 µ Tip: check structures with optical microscope to ensure regarding good coverage of the structures by resist.
Softbake/Prebake			
26	Implantation	**Equipment:** **Recipe:**	Hot Plate 120 °C for 2-3 min
Photolithography of Mask #4 (Low Dose Implantation)			
27	Implantation	**Equipment:** **Recipe:**	MA6 Mask Aligner (i-line) Dose = 100 mJ **Development:** AZ726 Time: 15 sec intervals and checking with optical microscope.
Hard Bake			
28	Implantation	**Equipment:** **Recipe:**	Hot Plate 110 °C for 30 min

Ion Implantation of Entire Beam			
29	Implantation	**Equipment:** **Recipe:**	 2.51e13 atoms/cm2 / 200 keV / Phosporous
Piranha Clean			
30	Implantation	**Equipment:** **Recipe:**	Wet Bench Piranha Solution (H2SO4:H2O2 : 70%:30%) Time = 10-15 min Sonication in acetone for 10 min
Oxide Deposition			
31	Implantation	**Equipment:** **Recipe:**	PECVD Thickness: 1780 Å Time: 2.5 min
Diffusion			
32	Implantation	**Equipment:** **Recipe:**	Furnace Furnace - 1000 °C, 0.5 Hours No oxygen in tube
BOE			
33	Implantation	**Equipment:** **Recipe:**	Wet Bench 6:1 BOE Estimated Etch Rate = 1000 Å/min Time = ~2.5 min
AZ 5214E			
34	Implantation	**Equipment:** **Recipe:**	BID-TEK SP-100 Spin Coater 2000 rpm for 40 sec Thickness = ~2.5 µm
Softbake/Prebake			
35	Implantation	**Equipment:** **Recipe:**	Hot Plate 120 °C for 2 min
Photolithography of Mask #5 (High Dose Implantation)			
36	Implantation	**Equipment:** **Recipe:**	MA6 Mask Aligner (i-line) Dose = 100 mJ Development: AZ726 Time: 15 sec intervals and checking with optical microscope. **Development:** AZ726 (check the development status every 20 sec)

Hard Bake			
37	Implantation	**Equipment:** **Recipe:**	Hot Plate 120 °C for 30 min
Ion Implantation of Heater Regions			
38	Implantation	**Equipment:** **Recipe:**	2.51e16 atoms/cm2 / 200 keV / 45° tilt / Phosporous
Piranha Clean			
39	Implantation	**Equipment:** **Recipe:**	Wet Bench Piranha Solution (H2SO4:H2O2 :: 70%:30%) Time: 15 min 10 min sonication in acetone is recommended.
Asher			
40	Implantation	**Equipment:** **Recipe:**	Asher (O2 plasma) with Oxford RIE Time: 5-20 min (check the progress every 5 min with optical microscope)
Oxide Deposition			
41	Implantation	**Equipment:** **Recipe:**	PECVD Thickness: 1780 Å Time: 2.5 min
Diffusion			
42	Implantation	**Equipment:** **Recipe:**	Furnace (no oxygen) Temperature = 1000 °C Time = 2 hours
AZ 5214E			
43	Contact/ Metal Lift Off	**Equipment:** **Recipe:**	BID-TEK SP-100 Spin Coater 500 rpm/9 sec Bake on hotplate at 120 C for 3min Tip: check the edges for complete coverage of the structures specifically close to the legs.

Softbake/Prebake			
44	Contact/ Metal Lift Off	**Equipment:** **Recipe:**	Hot Plate 120 °C for 3 min
Photolithography of Mask #6 (Open Vias for Metal Contact)			
45	Contact/ Metal Lift Off	**Equipment:** **Recipe:**	EVG 610 Double-sided Mask Aligner Exposure : i-line/ Contact mode: proximity: 100 µm Dose = ~150 mJ **Development** AZ726: Check the development status every 15 sec
Hard Bake			
46	Contact/ Metal Lift Off	**Equipment:** **Recipe:**	Hot Plate 120 °C for 10 min
Topside Oxide Etch			
47	Contact/ Metal Lift Off	**Equipment:** **Recipe:**	ICP-RIE Gases: Ar/CHF3 Etch Depth Needed = 1000 A Etch rate: 50 nm/min
Piranha Clean			
48	Contact/ Metal Lift Off	**Equipment:** **Recipe:**	Wet Bench Piranha Solution (H2SO4:H2O2 :: 70%:30%) Time = 15 min
Futurrex NR7-1500P			
49	Contact/ Metal Lift Off	**Equipment:** **Recipe:**	BID-TEK SP-100 Spin Coater 500 rpm/ 9 sec Thickness = ~2.75 µm
Soft Bake			
50	Contact/ Metal Lift Off	**Equipment:** **Recipe:**	Hot Plate 150 °C for 80 sec

Photolithography of Mask #7 (Metal Connections)			
51	Contact/ Metal Lift Off	**Equipment:** **Recipe:**	EVG 610 Double-sided Mask Aligner Exposure : i-line/ Contact mode: proximity: 100 µm Dose = ~250 mJ *Pre-Development* Bake Hot Plate, 100C for 2 minutes and 5 minute cool **Development** RD6 for 20 sec Rinse with DI Water and dry w/ N-gun
BOE			
52	Contact/ Metal Lift Off	**Equipment:** **Recipe:**	Wet Bench 6:1 BOE Estimated Etch Rate = 1000 Å/min Time = 10 sec
Topside Aluminum Deposition			
53	Contact/ Metal Lift Off	**Equipment:** **Recipe:**	E-Beam Evaporator 7000 Å Aluminum 2 Å/sec
Liftoff - Acetone Soak to Remove PR/Metal Layer			
54	Contact/ Metal Lift Off	**Equipment:** **Recipe:**	Wet Bench Sonication in acetone for 10-20 min
Apply Thick Photoresist (PR) to Topside			
55	Backside Alignment	**Equipment:** **Recipe:**	BID-TEK SP-100 Spin Coater Create protective layer AZ 4620 1500/750/35 Thickness = ~ 13.5 µm Or multiple coating with AZ5214 with 2000 rpm/30 sec (6 times) and baking after each coating for 5 min at 120 °C

Hard Bake (Only if AZ4620 is used for front side)			
56	Backside Alignment	**Equipment:** **Recipe:**	Hot Plate 115 °C for 5 min
Image reversal/Lift off (LOR+AZ5214E)			
57	Backside Alignment	**Equipment:** **Recipe:**	BID-TEK SP-100 Spin Coater Thickness=~200 nm (LOR 2A) (2000 rpm/40 sec) Thickness~ 1.4 µm (AZ5214E) (1000 rpm for 40 sec)
Softbake			
58	Backside Alignment	**Equipment:** **Recipe:**	Hot Plate 170 °C for 8 mins (LOR) 120 °C for 90 sec (AZ5214E) Image reversal bake: 90 sec at 120 °C
Photolithography of Mask #8			
60	Backside Alignment	**Equipment:** **Recipe:**	EVG 610 Double-sided Mask Aligner Contact mode: proximity contact, 100 µm separation *Exposure* Ch.2 (Wavelength = 365 nm) First exposure= 50 mJ Flood exposure= 250 mJ **Development:** AZ726 Check the wafer every 15 sec with optical microscope
E-beam evaporation of aluminum			
61	Backside Alignment	**Equipment:** **Recipe:**	Lesker E-beam Evaporator Aluminum deposition Thickness: ~1.2 µm Deposition rate: 2 Angstrom/sec
Lift off			
62	Backside Alignment	**Equipment:** **Recipe:**	Stripper at 80 °C Time: about 10 min Acetone sonication if needed.

Cleave Wafer			
63	Backside Alignment	**Equipment:** **Recipe:**	Work Bench Cleave wafer into 4 quadrants
Deposit thick aluminum layer on topside of Carrier Wafer			
64	Backside Alignment	**Equipment:** **Recipe:**	Lesker E-beam Evaporator Aluminum deposition Thickness: ~1 µm Deposition rate: 3 Angstrom/sec
Attach 1/4 Wafer to Carrier Wafer			
65	Release	**Equipment:** **Recipe:**	By Hand N/A
Backside Silicon Etch			
66	Release	**Equipment:** **Recipe:**	ICP-RIE at -90 °C Etch rate: ~2.2 µm/min Checking with microscope every 2 min once the cantilevers start to show up on the backside
Asher			
67	Release	**Equipment:** **Recipe:**	Asher (O2 plasma) with Oxford RIE Time: 5-20 min (check the progress every 5 min with optical microscope)
Soak to Separate Wafers			
	Release	**Equipment:** **Recipe**	Wet Bench Photoresist Stripper AZ400T Time = overnight Dry on hotplate
HF Release			
68	Release	**Equipment:** **Recipe:**	Wet Bench HF 49% Thickness = 1 µm Time = 10-20 sec Dry on a hot plate

SEM			
69	Release	**Equipment:** **Recipe:**	SEM to check the cantilevers